Interaction and Mixing Effects in Two and One Dimensional Hole Systems

Ahrash James Daneshvar

Downing College
University of Cambridge

Dissertation submitted for the degree of
Doctor of Philosophy

Except where stated otherwise, this thesis contains my own original work which was not done in collaboration with others. This thesis is not substantially the same as any that I have already submitted, or am in the process of submitting, for any degree at this, or another, University. It is less than 60 000 words long.

A. J. Daneshvar 26/5/1998

Summary

This thesis describes electrical measurements performed on low dimensional p-type devices, fabricated from GaAs/AlGaAs heterostructures. The Coulomb interaction between holes is similar to that between electrons. However, the kinetic energy is suppressed, which makes interaction effects particularly important. Holes may also be used to study band structure effects which arise from spin-orbit coupling in the valence band. The effects of Coulomb interactions in low dimensional *electron* systems are currently being studied extensively. Experiments presented in this thesis indicate the possible importance of Coulomb exchange interactions in both one and two dimensional *hole* systems (1DHSs,2DHSs).

Tilted magnetic field studies of 2DHSs in the quantum Hall regime indicate that Landau levels at *even* filling factors, ν, will not cross. For high ν, this is attributed to a spin-orbit mixing effect which arises from the low symmetry of the system. At lower ν, activation-energy measurements verify that the energy gaps decrease and then increase as the field is tilted. However, the energy gap versus field dependences do not exhibit the curvature that might be expected from a perturbative anticrossing. It is speculated that the origin of this effect is a phase transition driven by the exchange interaction. Balanced arguments contrasting the relative strengths of the mixing and interactions theories are provided.

The second part of this thesis describes a new method for the fabrication of ballistic 1DHSs, which exhibit clear conductance quantization. The quantization changes from even to odd multiples of e^2/h as a function of the magnetic field in the plane of the heterostructure, as 'spin splitting' causes the 1D subbands to cross. Measurements of the 1D subband energy spacings are used together with the magnetic fields at which the crossings occur to calculate the in-plane g factors of the 1D subbands. These are found to increase as the number of occupied 1D subbands decreases. This enhancement of the g factor is attributed to exchange interactions; possible mixing explanations are also discussed. At higher magnetic fields, the pattern of quantization features shows that the subbands have crossed many times, and that the 1DHS can be strongly magnetized.

Acknowledgements

I am heavily indebted to my PhD supervisor, Dr Chris Ford, for his time and patience, for trying to make me to think and write clearly, and for his encouragement. I would also like to thank Dr Alex Hamilton for getting me started in the laboratory at the beginning of my time in SP, and for useful discussions; in retrospect I should have been more appreciative. I would also like to thank Professor Mike Pepper for his enthusiasm, and for providing the group's excellent facilities. None of this work would have possible without the excellent wafers grown by Dr Michelle Simmons.

Other people with whom I have enjoyed useful discussions include Dr Nigel Cooper, Dr Eugene Kogan, Dr Shye Shapira, Dr Giles Davies and especially Dr Crispin Barnes.

I must thank the people that have proof-read parts of this thesis. They are: Dr Chris Ford; Dr Alex Hamilton; Dr Giles Davies; Dr Crispin Barnes; Dr Linda Macks; Dr K. J. Thomas; Louise McSweeney; John de Mello; Allon Jameson; Ian Castleton.

I would like to thank all of my friends, and in particular John, Jon, Nick, Jane, Allon, Llew and Ian, for trying to ensure that I don't take myself too seriously. I should also thank my office mates, Neil and Gil-Ho, for putting up with me - especially during the latter parts of this write-up. Past SP students deserving a mention, for their friendship and help, include Thomas, Neil Turner and Ian Castleton. I must thank my parents for all of their support, and Louise for keeping me sane.

Finally, I thank Pete Flaxman for providing me with helium at the weekends, Alan Beckett for his excellent practical skills, and Harry Clark for help in the clean room (including making one of my samples).

I have been funded by the EPSRC, the Semiconductor Physics group, Downing College, my parents and The Earl of Beaconsfield.

Publications

The work described in this thesis has resulted in the following publications:

A. J. Daneshvar, C. J. B. Ford, A. R. Hamilton, M. Y. Simmons, M. Pepper, and D. A. Ritchie, *Enhanced g factors of a one-dimensional hole gas with quantized conductance*, Phys. Rev. B, **55**, 13409 (1997);

A. J. Daneshvar, C. J. B. Ford, M. Y. Simmons, A. V. Khaetskii, A. R. Hamilton, M. Pepper, and D. A. Ritchie, *Magnetization instability in a two dimensional system*, Phys. Rev. Lett., **79**, 4449 (1997);

A. J. Daneshvar, C. J. B. Ford, A. R. Hamilton, M. Y. Simmons, M. Pepper, and D. A. Ritchie, *Multiple subband crossing in a one- dimensional hole gas with quantized conductance.* Proceedings of EP2DS-XII, Tokyo, 1997. To appear in Physica B, 1998.

Contents

Chapter 1

Introduction to low-dimensional hole systems

1.1 Introduction

The properties of interacting fermions confined to less than three dimensions have been studied intensively for over two decades. Through advances in both fabrication techniques and physical understanding, this branch of condensed matter physics continues to present interesting problems which require novel solutions. This thesis describes electrical measurements performed on two and one dimensional hole systems (2DHSs,1DHSs), which are made from p-type semiconductors, at very low temperatures and high magnetic fields. This chapter details some of the important processes involved in the fabrication of the two-dimensional hole system and the peculiarities of the particular types of sample used. In addition, it describes some of the essential physics of one and two dimensional systems (1DSs,2DSs) from a simplified 'parabolic band' point of view. Later chapters present a more rigorous treatment of the low-dimensional hole system, and also the specific details of theory relevant to the measurements which form the backbone of this thesis.

1.2 The fabrication of 2DHSs

1.2.1 Molecular beam epitaxy

Molecular beam epitaxy (MBE) enables the fabrication of very high quality layered semiconductor structures. For a detailed exposition see reference [1]. The starting point for growth is a very clean, either doped or undoped, crystal of GaAs mounted on a heated substrate holder in an ultra-high vacuum chamber. The particular facet of the crystal can strongly influence the nec-

essary growth conditions, type of dopant atom and also the final properties of the holes in the structure. The highest quality 2DHSs to date have been grown on the $\{311\}A$ planes of GaAs, and were doped with silicon (see also Section 1.2.2). All of the wafers studied in this thesis were grown by Dr M. Y. Simmons.

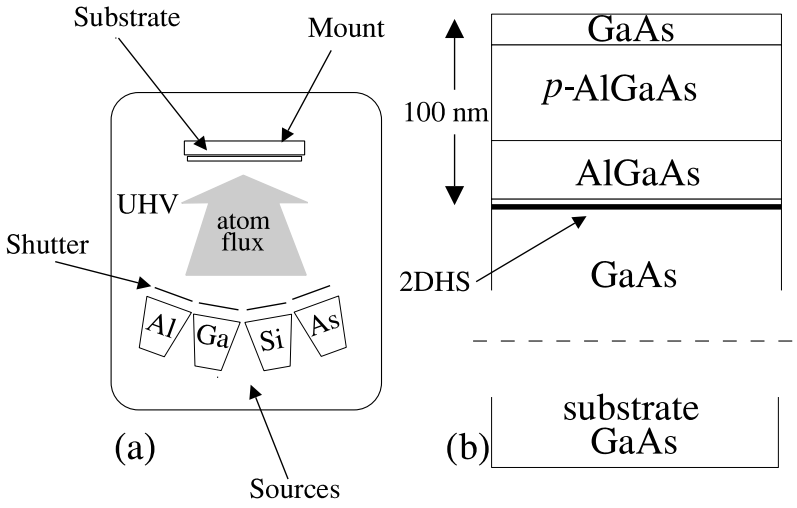

Figure 1.1: Schematic diagrams of: (a) an MBE chamber, in which very high quality GaAs/AlGaAs heterostructures may be grown with monolayer accuracy; (b) a typical device structure.

The growth is achieved by the exposure of the substrate to thermal fluxes of arsenic, gallium and aluminium (see Fig. 1.1(a)). The rate is carefully controlled so that a monolayer of either GaAs or $Al_xGa_{1-x}As$ is deposited approximately once every second. The symbol x represents the fraction of Ga sites occupied by As atoms in the crystal structure. It will be dropped from here on, except when explicitly referred to. Layers of different materials are deposited by changing the proportions of the fluxes at different stages of the growth. A typical single-interface structure is represented schematically in Fig. 1.1(b).

The formation of a 2DHS occurs at the interface between the two semiconductors; this process is described in Section 1.2.3. An important feature of the structure is the spacer layer of undoped AlGaAs which separates the 2DHS from the doped region, thereby reducing the amplitude of the random potential experienced by the holes due to the ionized dopants. The incorporation of a spacer layer in this manner is known as modulation doping [1].

1.2.2 Properties of {311} surfaces

It is found that silicon can act as an n- or a p-type dopant in GaAs, depending on the orientation and chemical composition of the crystallographic surface upon which it is deposited [2]. The cleaving of a GaAs crystal to expose a pair of (311) planes necessarily leaves one surface with the single dangling bonds belonging to gallium atoms and the double dangling bonds to the arsenic atoms; on the other surface, the arsenic atoms have the single dangling bonds. As depicted in Fig. 1.2, these two surfaces are labelled A and B respectively. The silicon dopant is incorporated on the single bond site during growth; for the A surface Si has one electron too few whereas for the B surface it has one electron too many. Thus a $(311)A$ surface is p-doped by silicon.

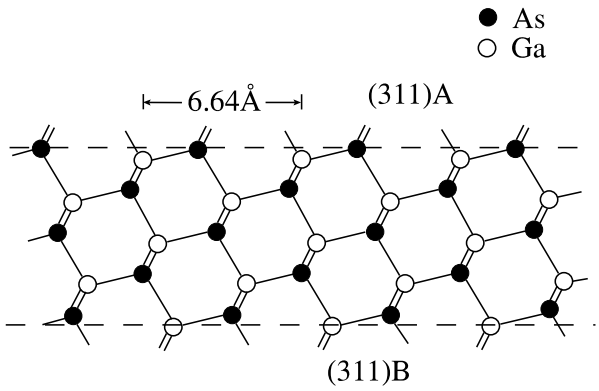

Figure 1.2: The $(311)A$ and $(311)B$ surfaces, in which the single dangling bonds belong to either Ga or As atoms respectively.

Corrugations are another important feature of the {311} planes. They are believed to form during growth by surface reconstruction, which favours a lower energy array of steps over the higher energy flat surface. The resulting corrugations are aligned to the $[\overline{2}33]$ direction, and have a periodicity and height of 32 Å and 10 Å respectively [3].

1.2.3 Spatial band structure

The band gap of GaAs is direct, and below a temperature of 4 K has a value of 1.52 eV [4, 5]. Although the band gap of AlAs is indirect, the band gap of $Al_xGa_{1-x}As$ remains direct for x less than approximately 0.4. In the latter regime, the AlGaAs band gap varies as $1.52 + 1.26x$ eV [6]. The aluminium concentrations of the wafers studied in this thesis were measured after growth, using a photo-voltage spectrometer, to have $0.30 < x < 0.36$.

The sum of the valence and conduction band offsets at the GaAs/AlGaAs interfaces of such a wafer is therefore approximately 0.4 eV. Using the 2:1 prescription [6], the valence band offset is estimated to be approximately 0.14 eV. The forward-bias voltages of NiCr/Au Schottky contacts measured as part of this work were found to vary between 0.38 V and 0.8 V, and must be similar to the Schottky barrier height.

Figures 1.3(a) and (b) plot the energy of the valence band edge versus distance from the surface of the wafer, for a shallow single-interface wafer and a deeper approximately symmetrically-doped quantum well wafer. The Schottky barrier height and the valence band offset have been assumed to be 0.8 eV and 0.14 eV respectively.

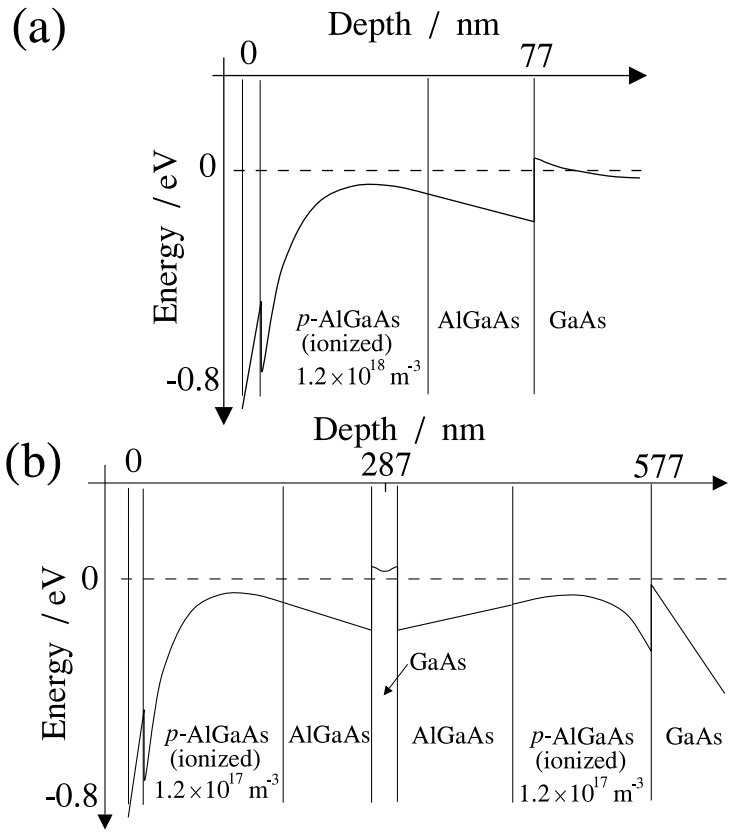

Figure 1.3: Schematic graphs plotting the energy of an electron at the valence band edge, as a function of distance from the surface of the wafer. (a) shows the band structure for a wafer similar to that depicted in Fig. 1.1(b), whilst (b) is for a wafer such as T240 (see the text).

The band structure of Fig. 1.3(a) can be understood using Poisson's equation, $-\nabla^2\Phi = \rho/\epsilon$, which relates the curvature of the electrostatic potential Φ to the local charge density ρ. The permittivity of the medium, ϵ, depends on the stoichiometry of the material and its temperature, and takes a value of approximately $12.7\epsilon_0$ in GaAs [7] at temperatures below 4 K. ϵ_0 is the permittivity of free space; this and other physical constants used in this thesis are defined in Appendix A. In the *p*-doped regions of the AlGaAs, the acceptors are assumed to be fully ionized and the potential is therefore parabolic. Gauss's law shows that $\nabla\Phi$ is continuous from this doped region into the undoped AlGaAs barriers, and also across the GaAs/AlGaAs interface. At this hetero-interface, the band edge is discontinuous and falls below the chemical potential. The strong electric field due to the ionized dopants causes band bending which confines holes to the hetero-interface.

Although some transport measurements were made of such single-interface heterostructures (see Section 6.3.1), the experiments presented in Chapters 2 to 8 were performed on wafers in which the 2DHS was confined to an approximately symmetric quantum well of width 200 Å. The band structure of one of these deeper wafers, T240, is depicted in Fig. 1.3(b). Another wafer studied was T335n+, which had a similar spatial band structure, but was grown on a conducting n+ substrate. More details of these wafers are provided in Chapters 2 and 4, and also in Appendix B which contains the growth structures.

1.2.4 Processing of samples

The study of the electrical properties of the 2DHSs requires a number of extra processing steps to taken. These include the fabrication of ohmic contacts to the 2DHS, which lies below the surface of the wafer, and the deposition of Schottky contacts to enable a variation of carrier concentration. In this work, such 'chips' or 'devices' were fabricated using optical (and electron-beam) lithography to define selected regions of the 2DHS into 'Hall bars' with annealed AuBe ohmic contacts, and NiCr/Au Schottky contacts (or 'gates'). A detailed description of these processes is provided in Appendix C.

1.3 Confined fermions, and length scales

The confinement of holes to a very narrow region of the semiconductor drastically alters their properties. Associated with the physical properties of the system are characteristic lengths, and energies and times, which determine the relevant physical processes. Because of the complexity of the experimental system, there are many such scales and consequently many regimes of behaviour.

The most important length scales are the dimensions of the hole system, λ_x, λ_y and λ_z. The z direction is taken to be normal to the plane of the 2DHS. In wafers T240 and T335n+, λ_z is less than 200 Å. In contrast, λ_x and λ_y are defined by the dimensions of the Hall bar (see Appendix C for more details), which are typically 80×800 μm.

1.3.1 The 2D density of states at zero magnetic field

The energy spectrum of the holes is quantized in 2D and takes the form

$$E = E_j + \frac{\hbar^2 k_{||}^2}{2m^*}, \tag{1.1}$$

where E_j represents the z confinement energy and takes a series of values dependent on the confinement potential, $k_{||}$ is the in-plane wavevector and m^* is an idealized hole effective mass. The hole energy has been taken to be positive. A more realistic description of the 2D dispersion relations is presented in Chapter 2; nevertheless, for some purposes the parabolic approximation with an effective mass of $0.2m_0 < m^* < 0.4m_0$ (where m_0 represents the mass of the electron in free space) is useful.

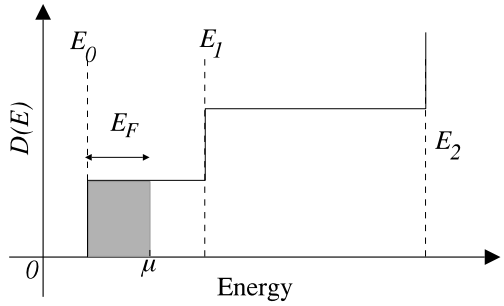

Figure 1.4: The density of states of a system of simple fermions confined strongly in one direction increases in steps. The shaded region represents the occupied states at low temperature; these particles cannot access the higher 2D subbands and their motion in the confinement direction is 'frozen'.

An idealized density of states $D(E)$ is plotted in Fig. 1.4, and takes the constant value

$$D(E)dE = \frac{d^2k}{4\pi^2} = \frac{m^*}{\pi\hbar^2}dE \tag{1.2}$$

for each 2D subband, per unit area. In this thesis, the 2D carrier concentrations n are sufficiently low ($n < 1.8 \times 10^{15}$ m^{-2}) that only one 2D subband

is ever occupied at low temperatures. Figure 1.4 also marks the Fermi energy E_F and the chemical potential μ. The flow of a current is a non-equilibrium process, and occurs by the occupation of a non-equilibrium distribution of k states. If the temperature T is sufficiently small, $k_BT \ll (E_j - E_{j+1})$, the holes move in the xy plane only, because of the insurmountable energy gap to excitation in the z direction. Every hole in the system thus has the same z component wavefunction.

1.3.2 Scattering at zero magnetic field

Other important length scales are related to scattering. Plane waves are eigenstates of the kinetic energy operator. They are not eigenstates of the full Hamiltonian however, and in the case of weak interactions the effect of the extra terms in perturbation theory is to cause transitions (or scattering) between the zeroth-order states. Theoretically, scattering is often parameterized by the mean time τ between scattering events. Because the hole system is degenerate, $E_F \gg k_BT$, the scattering processes are strongly affected by phase-space considerations and can only occur at or within k_BT of the Fermi energy. The scattering time τ may therefore be converted to a scattering length by $l = v_F\tau$, where v_F is the Fermi velocity. The scattering mechanisms may be classified as either elastic, in which case the hole has its direction changed but not its energy, or inelastic in which case both the energy and direction are altered.

Elastic scattering Elastic scattering mechanisms include remote-ionized impurity scattering from the acceptors, roughness scattering at GaAs/AlGaAs interfaces, alloy scattering due to inhomogeneities in the semiconductor stoichiometry, and scattering from background impurities. The wafers used in this work had been optimized in the MBE growth stage to limit these deleterious effects [8].

Because the energy of the hole is unaltered, the phase of the scattered wave has a well defined relationship with that of the incident wave. The scattering process is therefore phase coherent. The elastic scattering time, τ_e, is defined to be the mean time between elastic scattering events. Another important quantity is the large-angle scattering time $\hat{\tau_e}$. This scattering time is related to the electrical transport properties of the 2DHS, which are discussed in Section 1.4, through the mobility $\mu_{tr} = e\hat{\tau_e}/m^*$.

The mobility of 2DHSs confined to asymmetric heterostructures is strongly anisotropic. Transport in the $[\overline{2}33]$ (fast) direction is found to have the highest mobility; the lowest mobility (or slow) direction is orthogonal to this [9, 10]. In contrast, wafer T240 was found to exhibit a mobility anisotropy of less than 8%. In such symmetric quantum wells, the hole wavefunctions suffer less

overlap with the GaAs/AlGaAs interfaces than in single-interface heterostructures. The lack of strong mobility anisotropy therefore agrees with the suggestion [11, 12] that it arises from anisotropic interface-roughness scattering due to irregularities in the corrugations (discussed in Section 1.2.2).

In wafer T240, which had a mobility of approximately 130 $\mathrm{m^2V^{-1}s^{-1}}$ at temperatures below 1 K, the associated transport length (l_{tr}) is estimated to be (9 ± 0.07) μm using

$$l_{tr} = \frac{\hbar}{e}\mu_{tr}k_F. \tag{1.3}$$

It therefore usually exceeds the spacing between the dopants (which are the primary source of impurities). At low temperatures, both the transport and elastic scattering lengths are independent of temperature, and saturate at finite values related to the impurity spacings.

Inelastic scattering Inelastic scattering processes change the energy and therefore the phase of the hole. Typical examples include hole-phonon interactions and hole-hole interactions. All of the measurements in this thesis were performed below 1.2 K. Very few phonons are excited in the crystal in this regime, so the hole-phonon interaction is neglected here; the dominant process in limiting the phase coherence of the single-particle hole wavefunction is hole-hole scattering. The scattering time for this process in a clean 2D metal varies as $E_F/(k_BT)^2$, which reflects the phase space available for scattering of the two holes. The distance travelled with a constant phase is approximately $l_\phi \propto v_F/(k_BT)^2$. In diffusive systems, for which $l_\phi > l_{tr}$, the phase-coherence length is redefined to be $l_\phi = \sqrt{\mathcal{D}\tau_\phi}$, where $\mathcal{D}$ is the 2D diffusion coefficient. Many sophisticated calculations have been performed on electron systems, which modify the phase-space results by factors which are logarithmic in temperature, and also show that in very disordered systems the inelastic scattering time is roughly linearly dependent on temperature. See for example reference [13]. Phase-coherent transport has been observed in experiments in which 2DHSs are subjected to a strong magnetic field, and indicate a lower bound on l_ϕ of 2 μm [14].

Other scattering times The spin and the electrostatic potential Φ are coupled by the spin-orbit interaction, which is particularly strong in hole systems (see Chapter 2). This allows a scattering event to change the average angular momentum components of a hole. This represents the fact that spin is not a good quantum number in the presence of the spin-orbit interaction, and is characterized by the spin-orbit scattering time τ_{so}.

1.4 Electrical transport

1.4.1 Regimes

Modern lithographic techniques enable the fabrication of devices which are smaller than the transport scattering length l_{tr} and also the phase coherence length l_ϕ. A number of transport regimes may be identified, and are discussed in detail in reference [15]. Firstly, there is the diffusive transport regime in which $\lambda_x, \lambda_y \gg l_{tr}$. At high temperatures, the dynamics of this regime are semi-classical. However, at sufficiently low temperatures, the condition $l_\phi \gg l_{tr}$ can be fulfilled and quantum interference effects such as weak localization become important. It is worth noting that in very high mobility 2DHSs, this latter condition is not met due to the correspondingly high transport scattering length.

In the other extreme, $l_{tr} \gg (\lambda_x, \lambda_y)$, the holes' motion is *ballistic* and there is no scattering. Often, $l_\phi > (\lambda_x, \lambda_y)$, in which case quantum mechanical effects become very important.

1.4.2 Semi-classical electrical properties

The electrical properties of GaAs/AlGaAs heterostructures are surprisingly well described using the (classical) Drude theory of metals, which has strong parallels with the kinetic theory of gases. A quantum theory such as the Sommerfeld theory of metals, or the Boltzmann (transport) equation [16], properly accounts for the fermionic nature of electrons (or holes). It is stressed here that both the 2DHS and 2DES are highly degenerate below 4 K, and are more similar to very low density two-dimensional metals than to typical bulk semiconductors.

Zero magnetic field The most useful result at zero magnetic field is the expression for the conductivity tensor, which relates current density $\mathbf{j}$ to electric field $\mathbf{E}$: $\mathbf{j} = \underline{\sigma}\mathbf{E}$. In the simplest theory the conductivity tensor is replaced by an isotropic conductivity σ,

$$\begin{aligned} \sigma &= ne\mu_{tr}, \\ \mu_{tr} &= \frac{e\hat{\tau_e}}{m^*}, \end{aligned} \tag{1.4}$$

although Chapter 2 shows that many of these assumptions are inappropriate for 2DHSs. The mobility μ_{tr}, which is often used as a measure of the quality of the 2DHS, reflects this scattering time and is the constant of proportionality between the applied field and the drift velocity of the holes.

Non-zero magnetic field The dynamics of particles in truly two dimensional systems are affected only by the component of magnetic field perpendicular to the plane of confinement, $B_\perp$. Physical effects are described in more detail in later sections, which show that for sufficiently high fields classical theories totally fail to explain observations. Furthermore, it turns out that in some regimes non-interacting quantum theories are also insufficient. In the semi-classical approach the effects of the field are determined by considering the Lorentz force on a moving particle, which is

$$\mathbf{F} = q(\mathbf{E} + \mathbf{v} \times \mathbf{B}) \tag{1.5}$$

where $\mathbf{v}$ represents the particle's velocity and q its charge (with $|q| = |e|$). $\mathbf{E}$ and $\mathbf{B}$ are the electric and magnetic fields. A classical free particle moves in circles with cyclotron frequency $\omega_C = eB_\perp/m^*$, and a cyclotron radius $r_C = m^* v_F/eB_\perp$. These quantities are discussed in a quantum context (Section 1.5.1) later. In a finite sample, the Lorentz force causes charge to build up at its edges. The resulting transverse electric field balances the second term of equation 1.5 and can be detected as a Hall voltage. These ideas are neatly summarized by the relation $\mathbf{j} = \underline{\sigma}\mathbf{E}$:

$$\begin{pmatrix} j_x \\ j_y \end{pmatrix} = \frac{\sigma}{1 + (\omega_C \hat{\tau_e})^2} \begin{pmatrix} 1 & -\omega_C \hat{\tau_e} \\ \omega_C \tau & 1 \end{pmatrix} \begin{pmatrix} \mathrm{E}_x \\ \mathrm{E}_y \end{pmatrix}. \tag{1.6}$$

The diagonal elements of the $\underline{\sigma}$ are referred to as σ_{xx} and the off-diagonal ones are called σ_{xy}. The particularly useful resistivity tensor $\underline{\rho} = \underline{\sigma}^{-1}$ may also be defined.

1.4.3 Quantum transport: the Landauer-Buttiker formalism

The theory of transport at low temperatures in the limit $l_\phi \gg \lambda$ has been developed by Landauer [17] and extended by Buttiker [18]. Although the latter condition does not hold at zero magnetic field in typical 2DHSs, the concepts provide a natural explanation of the integer quantum Hall effect. It is therefore worth spending some time explaining the theory, which strictly applies to non-interacting fermions only.

The model system to be treated is depicted in Fig. 1.5, and consists of a 2D region which is smaller than the phase coherence length of the system. The 2D region is contacted by 'perfect' leads which connect to ideal sources and sinks of particles. No scattering occurs in the leads; thus all particles incident upon them are transmitted into the reservoirs and all particles emitted from the reservoirs progress into the sample. The ith reservoir has a well-defined, constant, chemical potential μ_i which is unaffected by any flow of charge. The

perfect leads may be of any dimensionality. However, initially it is assumed that they are truly 1D and that the reservoirs are connected to the system by a single 1D quantum channel (or 'mode'); the results will be extended to leads with more quantum channels (the quasi-2D limit) later.

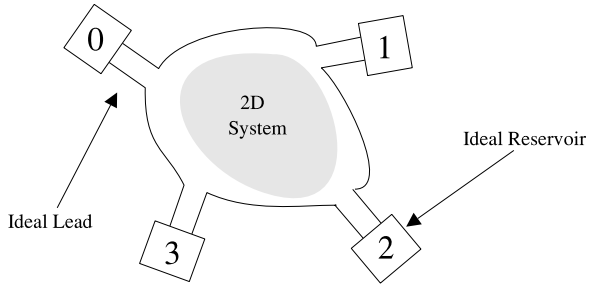

Figure 1.5: A schematic diagram showing an ideal 2D system in which elastic scattering only occurs, connected to ideal reservoirs by ideal leads.

For convenience, the lowest chemical potential μ_0 is set to zero. No transport occurs due to particles below this chemical potential because in all leads the number of positive- and negative-going k states are filled. Defining $\Delta\mu_i = \mu_i - \mu_0$, the current injected by the ith reservoir into its lead is

$$I_i^+ \approx ev_i\overrightarrow{D}(\mu)\Delta\mu_i \tag{1.7}$$

where v_i is the group velocity at the chemical potential and $\overrightarrow{D}$ is the 1D density of states for particles with positive wavevectors. The group velocity is defined to be $(1/\hbar)dE/dk$. In 1D, the density of states is $\overrightarrow{D}(E) = (1/2\pi)dk/dE$, which cancels the group velocity to give

$$I_i^+ = \frac{e}{h}\Delta\mu_i. \tag{1.8}$$

The probability that a particle injected from the ith lead is scattered back into that lead is defined to be R_{ii}. Similarly, T_{ij} represents the chance that a particle injected by the jth lead enters lead i. Thus the current into the ith lead may be written as I_i^-

$$I_i^- = \frac{e}{h}\left(R_{ii}\Delta\mu_i + \sum_{j\neq i} T_{ij}\Delta\mu_j\right). \tag{1.9}$$

Hence the net current flowing out of the ith reservoir is

$$I_i = I_i^+ - I_i^- = \frac{e}{h}\left((1 - R_{ii})\Delta\mu_i - \sum_{j\neq i} T_{ij}\Delta\mu_j\right). \tag{1.10}$$

By interpreting the chemical potential differences as voltages, the various conductances of the system may be calculated. This derivation holds for arbitrary magnetic field strength, because the cancellation of the density of states by the group velocity occurs at all field strengths. This phenomenological derivation closely follows that of Buttiker [18], and has been verified by Baranger and Stone using first-order perturbation theory in an arbitrary magnetic field [19].

Extra 1D subbands may be introduced into the leads using a generalized scattering probability $T_{ij,kl}$ where the second pair of subscripts means that the particle is injected by the lth subband of lead j and is scattered into the kth subband of lead i. The coefficient $R_{ii,kl}$ is defined similarly.

Assuming that all channels are fed up to the same potential by their respective reservoirs, equation 1.10 generalizes to:

$$I_i = \frac{e}{h}\left((Q - R_{ii})\Delta\mu_i - \sum_{j\neq i} T_{ij}\Delta\mu_j\right) \tag{1.11}$$

where $R_{ii} = \sum_{kl} R_{ii,kl}$, $T_{ij} = \sum_{kl} T_{ij,kl}$ and Q is an integer counting the number of conducting 1D channels in the lead [18]. This equation is equally applicable in an arbitrary strength magnetic field.

1.5 The quantum Hall effects

1.5.1 Application of a perpendicular magnetic field

The single-particle Hamiltonian in a perpendicular magnetic field may be written as

$$H = \frac{(\mathbf{p} + q\mathbf{A})^2}{2m^*} + q\Phi \tag{1.12}$$

where $\mathbf{A}$ is the vector potential with $\mathbf{B} = \nabla \times \mathbf{A}$ [20]. Two useful gauges are the symmetric gauge $\mathbf{A} = (-yB_\perp/2, xB_\perp/2, 0)$ and the Landau gauge $\mathbf{A} = (0, xB_\perp, 0)$, both of which provide $\mathbf{B} = B_\perp\hat{z}$. The energy spectrum of the particles, which is continuous at zero magnetic field, is quantized into harmonic oscillator energy levels known as Landau levels $E_N = \hbar\omega_C(N + 1/2)$ with $\omega_C = eB_\perp/m^*$ [20]. N is an integer (≥ 0) known as the harmonic oscillator,

or Landau level, quantum number. Each Landau level has a degeneracy of $eB_\perp/h$. A detailed description of the Landau level 'fans' of the valence band is given in Section 2.4. The important physics of the quantum Hall effects is most easily elucidated assuming electron-like parabolic bands.

The introduction of spin into the system doubles the number of energy levels. In the simplest of cases, the magnetic field affects the energy of the Landau levels through the inclusion of the Zeeman term $g\mu_B \mathbf{B}.\hat{\mathbf{s}}$, where g is the g factor of the particles, μ_B is the Bohr magneton and $\hat{\mathbf{s}}$ is the spin angular-momentum operator. A particular level is labelled $|N, s\rangle$ where s represents the spin-projection quantum number. The filling factor ν of the many-particle system is the number of filled spin-resolved Landau levels. When ν is an integer, the number of particles in the system exactly fits into ν spin-resolved Landau levels and there is an energy gap at the chemical potential.

Length scales and scattering for $B_\perp > 0$ At low magnetic fields, there are many occupied Landau levels in a many-particle system. The relevant length scale is the cyclotron radius $r_C = m^* v_F/eB_\perp$, which is the radius of the circular motion of the particles at the Fermi level. In the quantum limit, which occurs at high magnetic fields, the degeneracy of each Landau level increases until all of the particles occupy the lowest Landau level. A particle is localized about its guiding centre over a distance of $2l_B$, where

$$l_B = \sqrt{\hbar/eB_\perp} \tag{1.13}$$

is the magnetic length.

In the absence of scattering, the density of states of a 2DS subject to a strong perpendicular magnetic field may be written as a sum of delta functions

$$D(E) = \sum_N \frac{eB_\perp}{h} \delta(E - (\hbar\omega_c(N + \frac{1}{2}))) \tag{1.14}$$

where spin has been ignored for simplicity. As in the zero magnetic field case, the effect of scattering is to limit the lifetime of the particles. The finite lifetime may be related to a broadening of the density of states, by an energy Γ, using the uncertainty principle. The experimental observation of the discrete nature of the density of states requires not only that $k_B T \ll \hbar\omega_C$ but also that $\Gamma < \hbar\omega_C$. In the Born approximation, which holds for short-range scattering, Γ is a function of magnetic field, varying as $\sqrt{B_\perp}$ [21].

1.5.2 The integer quantum Hall effect

The discovery of the integer quantum Hall effect (IQHE) in silicon inversion layers in 1980 [22] has led to a whole new field of solid state physics. Its

observation three years later in a 2DHS [23] verified the universality of the effect. The experiment is performed by applying a strong magnetic field ($B_\perp$) perpendicular to the plane of the 2DS, at low temperatures. The primary observations are the very accurate quantization of the Hall resistivity ρ_{xy}, to values of $h/(ie^2)$ where i is an integer, and the simultaneous vanishing of the diagonal resistivity ρ_{xx} at integral filling factors. Fig. 1.6 shows data obtained from the T240 2DHS at 290 mK. The features are periodic in $1/B$, and reflect

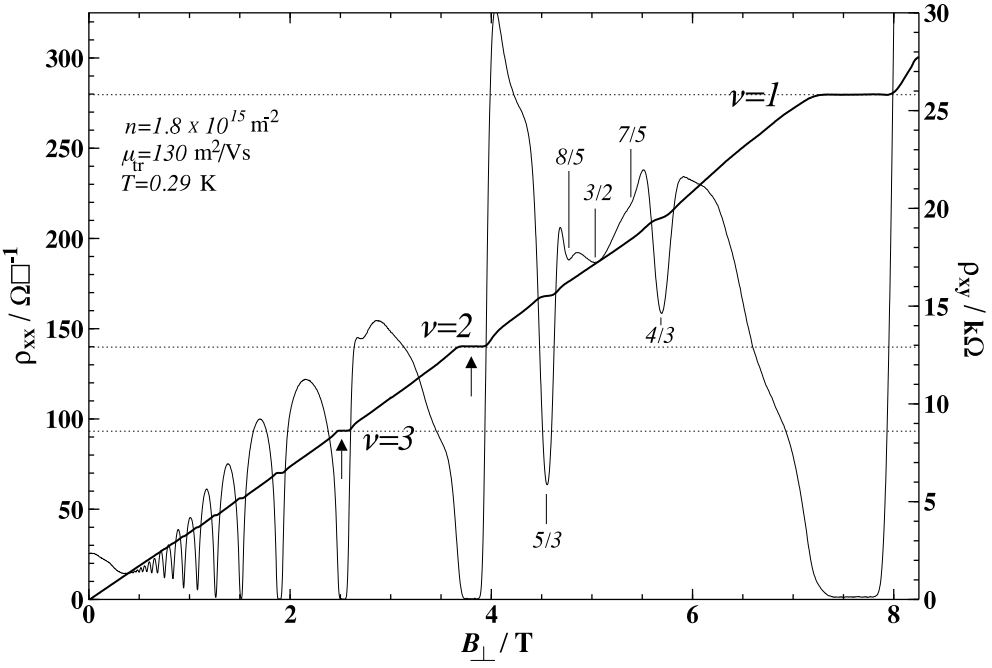

Figure 1.6: ρ_{xx} and ρ_{xy} versus perpendicular magnetic field in the high mobility T240 2DHS. Low integer filling factors are marked on the diagram by the arrows. Some fractional quantum Hall effect states are visible in the vicinity of $\nu = 3/2$.

the quantization of the hole energy spectrum into Landau levels.

A crucial part of the explanation of the IQHE is the idea of localized and delocalized states, which arise when disorder is considered. The quantized density of states is represented in Fig. 1.7. Because the system contains a fixed number of particles and the degeneracy of the levels is proportional to $B_\perp$, the chemical potential is swept by the field through the peaks and troughs of the density of states.

The states in the minima of the DOS are localized by the disorder potential when the corresponding localization length ξ is less than the size of the sample. As the chemical potential moves towards the peaks in the DOS, the localization

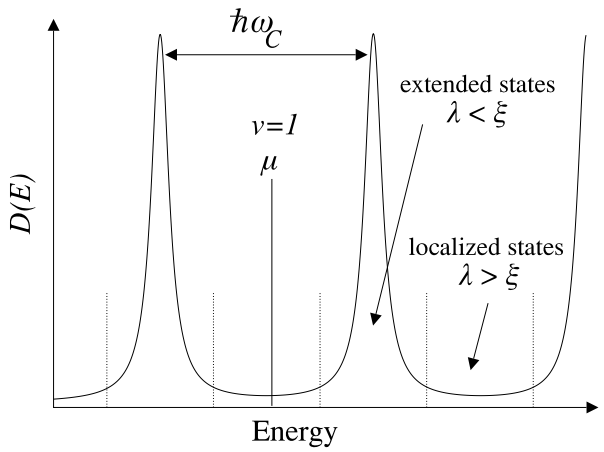

Figure 1.7: The quantized density of states of a disordered sample subject to a strong magnetic field $B_\perp$, showing localized and extended states separated by the dotted lines.

length increases until it exceeds the sample size, at which point the states are delocalized over the whole system [24, 25].

1.5.3 Edge and Bulk transport

In the delocalized regime, the transport occurs in the bulk of the sample and is dissipative: the Hall voltage varies with magnetic field as might be expected from classical considerations, and ρ_{xx} and σ_{xx} are non-zero. In contrast, near to integer ν, no transport can occur in the bulk because the holes are localized. It is here that transport at the edge of the sample becomes important. Figure 1.8(a) shows that in a sample with smooth edges, the Landau level energies are shifted adiabatically by the electrostatic potential near to the edge of the sample, and penetrate the chemical potential at some point near to the edge.

These 'edge states' are quasi-1D and have a very large coherence length. In this simplistic picture, the edge states are very narrow; a more sophisticated theory shows that in fact they form compressible and incompressible strips of non-zero width at the edge of the sample [26]. The classical analogue of these states are skipping orbits along the edge of the sample. Edge channels have been observed directly in the vicinity of a shallow edge of a 2DES [27].

The conductance of the system may be deduced using the Landauer-Buttiker approach introduced earlier. Referring to Fig. 1.8(b), we assume that ohmic contacts 0 and 3 are the current source and sink respectively, and

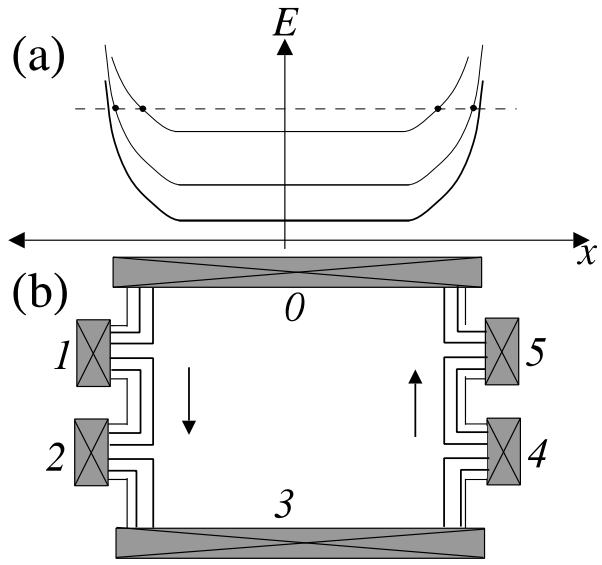

Figure 1.8: (a) The formation of edge states at the chemical potential of a finite sample. (b) Transport due to edge states, which occurs when contacts feed the edge channels to different levels. On a particular edge, the current flows in one direction only.

that the other contacts act as voltage probes. There is no scattering between the two sides of the sample, because they are separated by a large distance. Hence, the current admitted by contact 1 must be the same as the current emitted by contact 0 on that side of the Hall bar. Contact 1 draws no net current so it must emit the same current as and have an equal chemical potential to contact 0: $\mu_1 = \mu_0$. Similarly, $\mu_2 = \mu_1$. The voltage measured between contacts 1 and 2, $(\mu_2 - \mu_1)/e$ is therefore zero and $\rho_{\rm xx} = 0$. The dissipation-free current flow arises from the absence of back-scattering, which in turn is due to the magnetic field which physically separates the opposite-direction current paths. The net current flowing in the system is

$$i\frac{e}{h}\mu_0 - i\frac{e}{h}\mu_3 \tag{1.15}$$

where i is an integer counting the number of edge states. The transverse voltage is given by $V_{24} = (\mu_2 - \mu_4)/e = (\mu_0 - \mu_3)/e$. Thus the Hall resistivity is

$$\rho_{\rm xy} = V_{24}/I_{03} = \frac{h}{ie^2}, \tag{1.16}$$

which explains the quantization in the integer quantum Hall effect.

1.5.4 The fractional quantum Hall effect

It was discovered in 1982 that for $\nu < 1$ in 2DESs, the Hall resistance is also quantized according to

$$\rho_{xy} = \frac{h}{fe^2} \tag{1.17}$$

$$f = \frac{p}{q} \tag{1.18}$$

with $p < q$ and both integral [28]. The same effect was soon observed thereafter in 2DHSs [29], and has been studied since in some detail [30]. A natural way to generate the allowed integers was proposed in the context of a global phase diagram of the quantum Hall effects, and relates the integral and fractional versions through a set of 'similarity' transformations [31]:

$$\begin{aligned} \nu &\rightarrow \nu + 1 \\ \nu &\rightarrow 1 - \nu \\ \frac{1}{\nu} &\rightarrow 2 + \frac{1}{\nu}. \end{aligned} \tag{1.19}$$

The final transformation is a consequence of the celebrated 'Composite Fermion' theory [32]. In samples of sufficiently high mobility, fractional quantization for $\nu > 1$ may be observed, as in Fig. 1.6 where there are fractional states around $\nu = 3/2$. In contrast to the integer quantum Hall effect, the energy gaps in the fractional states have a many-body origin.

1.6 One-dimensional systems

Systems exhibit quasi-1D behaviour when, in addition to their confinement to two dimensions, they are confined strongly in a second direction. This was first achieved using surface patterning of 2DHSs on a sub-micron length scale, using electron beam lithography and Schottky gating [33, 34], and remains the most flexible technique for 1D confinement (see Appendix C). Recent developments include the use of self-organised growth to fabricate V-groove wires, which are extremely narrow and therefore provide very large confinement energies, and the technique of cleaved-edge over-growth which produces long, impurity free, one dimensional systems [35] of exceptionally large subband spacing. In this section, conductance quantization in ballistic systems is introduced. The experimental realization and investigation of the ideas presented here, with regard to hole systems, are detailed in Chapters 6 to 8.

1.6.1 Ballistic Quantization

The transport properties of quasi-1D systems are easily treated using the Landauer-Buttiker formalism. It turns out that the cancellation of the 1D density of states by the group velocity quantizes the two-terminal conductance G. Consider the system shown schematically in Fig. 1.9, which shows

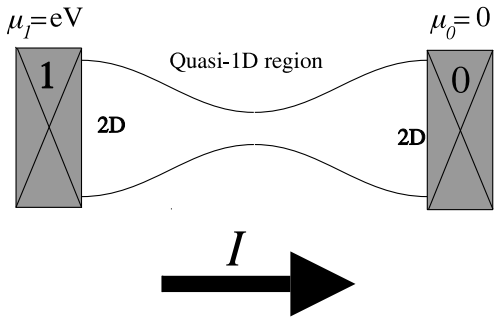

Figure 1.9: A two-terminal measurement of the conductance of a quasi-1D wire.

a two-terminal measurement of the conductance of a 1D wire defined in some way in a 2D system. Immediately setting $\mu_0 = 0$ and $\mu_1 = eV$ where V represents an applied voltage, we can simplify equation 1.11 to give:

$$I_1 = -I_0 = \frac{e^2}{h} V \left((Q - \sum_{kl} R_{11,kl}) \right) = \frac{e^2}{h} V \sum_{kl} T_{kl} \tag{1.20}$$

$$G = \frac{\partial I}{\partial V} = \frac{e^2}{h} \sum_{kl} T_{kl} \tag{1.21}$$

where the subscripts i and j have been dropped.

In a system satisfying $T_{kl} = \delta_{kl} T_l$ (no inter-subband scattering), G may be written as

$$G = 2\frac{e^2}{h} \sum_{l} T_l \tag{1.22}$$

where the factor of two has been introduced to account for spin. Thus the conductance of the system (in this set of approximations) is determined by the transmission of particles through the 1D region of the system depicted in Fig. 1.9. Provided that the transmission coefficients take the values one or zero only, the conductance is quantized in multiples of $2e^2/h$. Conductance

quantization was first observed in 1988, in narrow quasi-one dimensional constrictions created in a 2DES [36, 37]. Ten years since, the study of holes in small structures is still particularly under developed, because of fabrication and measurement difficulties (see Chapter 6). Experiments to date include the observation of magnetic focussing of ballistic holes in 2DHSs [38], which were used to probe the anisotropies of the 2D Fermi contour [38, 39]. The quantization of conductance in 1DHSs was first observed by Zailer *et al.* [14].

1.7 Scope and context of this thesis

This thesis describes electrical measurements performed on one- and two-dimensional hole systems at temperatures below 300 mK, both at zero and strong magnetic fields. The common thread is the possible observation of effects due to Coulomb interactions.

In spite of the lower kinetic energy of a hole system in comparison with a similar electron system (see Chapter 2), which should enhance the importance of the Coulomb interactions, the only transport observations which can be attributed with certainty to interactions between holes are those of the fractional quantum Hall effect in 2DHSs. Other than the extensive studies of that effect, which have been in progress for fifteen years, there are few experimental or theoretical works on the transport properties of interacting holes. These are described in more detail in Section 3.5; and virtually all have concerned correlation effects between holes. In contrast, this thesis provides evidence for the importance of the effects of exchange interaction.

The thesis is organised as follows. Chapter 2 describes the complicated valence band of the 2DHS in zero and perpendicular magnetic fields, in terms of the theoretical and experimental studies to date. It includes new data demonstrating the importance of the reflection symmetry of the confinement potential of the 2DHS. Because this thesis describes interaction effects, a short chapter follows in which the exchange interaction is described and in which the theory of an exchange-induced phase transition in the 2DS is detailed.

Chapter 4 describes an extensive series of tilted-field measurements which show that hole Landau levels do not necessarily cross. Furthermore, new activation-energy measurements of the energy gaps at $\nu = 4$ are presented which show that the energy gap versus B relation has a particularly abrupt turning point. In contrast, at the odd filling factor $\nu = 5$ the energy gap versus B relation exhibits curvature over large range of magnetic field.

The following chapter presents some interpretations of the tilted field data, in the context of valence band mixing and also an exchange-driven first-order phase transition. It is speculated that the latter effect may explain the sharp-

ness of the turning point at $\nu = 4$. There is scant evidence in the literature for such a phase transition in any material system, despite its prediction many years ago.

The thesis then turns to one-dimensional hole systems, with a description in Chapter 6 of the development of a technique for their fabrication. Measurements of conductance quantization in 1DHSs are presented. The superior device stability enables the first detailed experiments on the properties of these 1DHSs. In particular, the first measurements of the 1D subband energy spacings of a 1DHS are presented.

Chapter 7 describes the effect of a parallel magnetic field (applied in the plane of confinement) on the quantization of the 1DHS, and shows evidence for the crossing of the 1D subbands. From the magnetic fields of the crossing points, and the subband energy spacings, parallel g factors of the 1D subbands are deduced. They are found to increase by approximately a factor of two as the number of occupied subbands decreases. It is argued that this effect could be due to one-dimensional exchange interactions, although possible mixing explanations are also discussed.

The final chapter of experimental work presents strong evidence for the multiple crossing of 1D subbands. From the pattern of conductance features at high parallel fields, it is shown that the 1D subbands have crossed many times and that the system is very strongly polarized. This regime is not accessible to electron systems because of the larger 1D subband energy spacings of the 1DES.

A 'Conclusions and Further Work' chapter and some appendices, mainly concerning clean-room processing and measurement techniques, complete this thesis.

Chapter 2

Subbands of the two-dimensional hole system

2.1 Introduction

This chapter presents a mainly theoretical discussion of the single-particle band structure of GaAs based devices, concentrating on general results for the valence band. The properties of the holes in three and two dimensions are described in the context of the Luttinger Hamiltonian; the results of calculations (by others) for some devices are included. The formation of Landau levels in a perpendicular magnetic field is also covered. Finally, some new experimental results which demonstrate the sensitivity of the 2DHS to perpendicular *electric* fields are presented.

2.2 Bulk (3D) GaAs

2.2.1 3D energy bands

GaAs is a zinc-blende semiconductor crystal with a direct band gap of 1.52 eV at liquid-helium temperatures. Symmetries of the Hamiltonian include translational and time reversal invariance, and the symmetries of the crystal point group T_d [40]. For a description of the symmetry operations of T_d, see reference [41]. Whilst the Hamiltonian retains these symmetries, certain essential degeneracies cannot be lifted whatever the strength of the crystal potential.

Surprisingly, the nearly-free electron model is a very good starting point for a discussion of the properties of the bands [42, 43], although it cannot determine the actual ordering of the states even at the centre of the Brillouin zone (the Γ point). It is found that at the Γ point, the Bloch functions of the valence band edge have the same symmetries under the operations of the group

T_d as p orbitals and are therefore six-fold degenerate. Similarly, the conduction band edge is s-like with a two-fold degeneracy. The inclusion of the spin-orbit interaction lifts the degeneracy of the Γ point into a four-fold degeneracy with the symmetries of a total angular-momentum quantum number $J = 3/2$ atomic state, and a $J = 1/2$-like doublet. In the language of group theory, the $J = 3/2$-like states transform as the Γ_8 irreducible representation of the group T_d, whilst the $J = 1/2$-like doublet transforms as Γ_7 [40]. Figure 2.1(a) shows the results of pseudopotential calculations [44] for the band structure in the whole of the Brillouin zone. Figure 2.1(b) shows experimental data obtained in optical experiments [45]. Each k branch is, within the experimental error, two-fold degenerate (see the next section). The letters on the horizontal axis represent the reduced wavevectors of the special, high symmetry, points of the Brillouin zone, which are Γ at the zone centre and $X, \mathrm{U}, \mathrm{K}, \mathrm{L}$ at the boundary.

The physics of holes is determined in part by the properties of the valence band edge, which is defined to be at $E = 0$. The figure shows the lifting of the four-fold degeneracy of the Γ point as k increases, into the so-called light- and heavy-hole dispersions. Displaced at an energy of 341 meV below the band edge are the Γ_7 split-off holes. The different curvatures, and their dependence on direction in the crystal, are discussed using a perturbation theory in the next section.

2.2.2 The Luttinger Hamiltonian

To a reasonable approximation, the conduction (Γ_6) and split-off (Γ_7) bands may be ignored in a perturbation theory. Using group-theoretical arguments and restricting himself to the Γ_8 sub-space, Luttinger discovered a general $\mathbf{k}.\mathbf{p}$ Hamiltonian correct to second order in the components of $\mathbf{k}$ for crystals of the diamond structure, subject to arbitrary strength spin-orbit interaction [46]. This may be written as

$$\begin{aligned} H &= \beta_1 \sum_\alpha k_\alpha^2 + \beta_2 \sum_\alpha k_\alpha^2 J_\alpha^2 + \beta_3(\{k_x, k_y\}\{J_x, J_y\} + \\ &\quad \{k_y, k_z\}\{J_y, J_z\} + \{k_z, k_x\}\{J_z, J_x\}) \end{aligned} \tag{2.1}$$

where the brackets $\{\}$ denote the anticommutator. The J_α are 4×4 angular momentum matrices representing $J = 3/2$; the Hamiltonian is equivalent to the 4×4 secular equation which is arrived at in a (second order) treatment of the problem in degenerate perturbation theory. The zeroth-order basis is composed of four states $|J, M_J\rangle$ formed by the superposition of p-like band-edge Bloch functions. The number M_J is equivalent to the eigenvalue of the J_z operator in cylindrically symmetric systems, and may take the values $3/2, 1/2, -1/2, -3/2$. The Hamiltonian has been expressed in terms of a

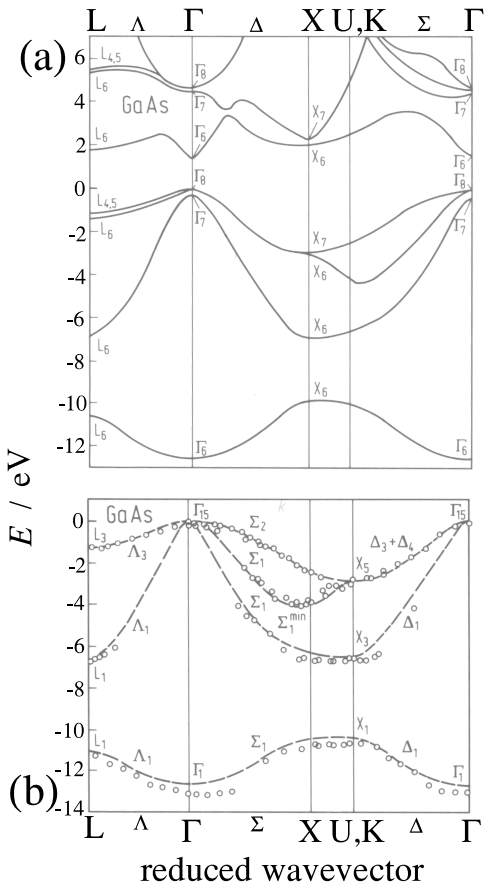

Figure 2.1: Band structure of GaAs from theory (a) and experiments (b) showing the complexity of the valence band edge (which occurs at the centre of the Brillouin zone). The horizontal axes represent wavevector, in the direction of the high-symmetry points $\Gamma, \mathrm{X}, \mathrm{L}, \mathrm{U}$ and K of the Brillouin zone.

complete set of matrices constructed from the identity matrix and the angular momentum matrices, and is invariant to the symmetry operations of the crystal point group.

The eigenvalues of the matrix form two anisotropic bands, with different curvatures, which describe the dispersion of the heavy and light holes (HH,LH) near to the Γ point, visible in Fig. 2.1. At each particular k value in either of these bands, there are two solutions corresponding to an effective spin degeneracy, which arise because the Luttinger Hamiltonian is symmetric with respect to space inversion [43]. However, the group T_d of GaAs does not contain this operation and this two-fold degeneracy should be lifted at non-zero

k. This may be achieved by adding terms linear in k to the Luttinger Hamiltonian [40, 47]. However, this splitting is estimated to be very small for the wavevector range of interest and is usually neglected.

The Hamiltonian (2.1) may be expressed as a single matrix. It is conventional to replace the β_i by the Luttinger parameters $\gamma_1, \gamma_2, \gamma_3$ according to $\beta_1 = \gamma_1 + 5\gamma_2/2, \beta_2 = -\gamma_2, \beta_3 = -2\gamma_3$. See Appendix E for the values of these parameters and an example of the matrix.

The energy bands described by the Luttinger Hamiltonian are anisotropic, as required by the more sophisticated theory and also high resolution experiments [48]. However, the Hamiltonian may be re-expressed to emphasize the terms which, besides having cubic symmetry, also are spherically symmetric [49, 50]. It turns out that the spherically asymmetric terms are quite small, and proportional to $\gamma_3 - \gamma_2$. Therefore two further approximation schemes may be employed. Firstly, there is the spherical approximation, which neglects all of the terms without spherical symmetry. The bands so calculated are isotropic. In the axial approximation, one of the terms neglected in the spherical approximation, which has cylindrical symmetry, is now included. In this way, anisotropy in the (100) plane may be neglected [51].

In either of these two approximations, the eigenvectors of the Luttinger Hamiltonian retain their M_J symmetries for non-zero k provided that the z direction is chosen to lie along the direction of travel through the crystal. The HH dispersion is then $M_J = \pm 3/2$; the LH has $M_J = \pm 1/2$.

2.3 Confinement to two dimensions

The two-dimensional samples studied in this work were mostly confined to symmetrically-doped GaAs quantum wells sandwiched between undoped barriers of $Ga_{0.67}Al_{0.33}As$. The band structure of the 2DHS has been studied extensively, both theoretically and experimentally. Early theoretical papers [47, 52] dealt with single-interface heterostructures; these differ from symmetric quantum wells because the holes are subject to a strong electric field perpendicular to the interface. More recent calculations [53, 54, 55, 56] have been performed in a larger subspace of band-edge states (e.g. $\Gamma_6, \Gamma_7, \Gamma_8$), and for wells grown in a variety of crystal orientations.

2.3.1 Symmetry effects

Confining the holes to motion in two dimensions reduces the symmetry of the Hamiltonian and lifts the four-fold LH-HH degeneracy of the Γ point. The lifting of this degeneracy may be seen to occur because of the different masses of the 3D LH and HH bands. When confined, they have different zero-point

energies and subband spacings; each forms a ladder of 2D subbands, the lowest energy of which is a HH subband. They are labelled HH1, HH2, .., HH_i (or LH_i) in order of increasing hole energy.

The point group of the two-dimensional crystal now depends on the plane of the interface. If this is the highly symmetric (100) plane, then in the case of diamond the group is reduced from O_h to D_{4h} for an inversion-symmetric quantum well and $C_{4\nu}$ for an asymmetric one. In the case of zinc blende, the symmetry is reduced from T_d to D_{2d} or $C_{2\nu}$. However, if the plane of the interface has high index, then most of the symmetries are lost. In the case of the diamond structure, the group is ultimately reduced to C_i for the symmetric well (and C_1 for an asymmetric well); for zinc blende there remains only the identity operation and the group is C_1 [55].

The potential remains periodic for translations parallel to the plane of the interface. Therefore the in-plane wavevector $k_{||}$ is a good quantum number. The momentum $k_\perp$ however is not, and the motion in the z direction is quantized (as discussed for the simple case of parabolic bands in Chapter 1).

At $k_{||} = 0$, the $M_J = \pm 3/2$ and $M_J = \pm 1/2$ symmetry of the HH and LH 2D subbands is retained exactly for (100) and (111) heterostructures, where the z axis is taken to be perpendicular to the growth plane. For samples grown on lower symmetry planes, this decoupling of the LH and HH subbands does not occur, except in the axial approximation, and there is mixing between the states. They are now labelled according to their dominant spinor component. In practice, the $k_{||} = 0$ mixing is rather small and the labelling of the subbands as heavy or light hole is meaningful. In all approximations, mixing between LH and HH states occurs when $k_{||}$ is greater then zero. This is because the choice of a non-zero parallel wavevector reduces the symmetry of the system further.

2.3.2 Results of calculations

The wavefunctions and eigenstates of the Hamiltonian of a heterostructure are found using the envelope-function approximation, the details of which are described in reference [57]. Results are obtained by modifying the Luttinger Hamiltonian as follows:

$$H \rightarrow H + q\Phi(z)I \tag{2.2}$$

$$k_z \rightarrow -i\frac{\partial}{\partial z} \tag{2.3}$$

where $\Phi(z)$ represents the confinement potential and I is the identity matrix. In the 4×4 case, a set of four coupled differential equations is obtained for each value of $k_{||}$. These equations are supplemented by boundary conditions.

If the Bloch functions in the two materials are taken to be equal, then these are expressed only in terms of the envelope functions. They are: (i) continuity of the envelope function; (ii) conservation of current through the interfaces [57].

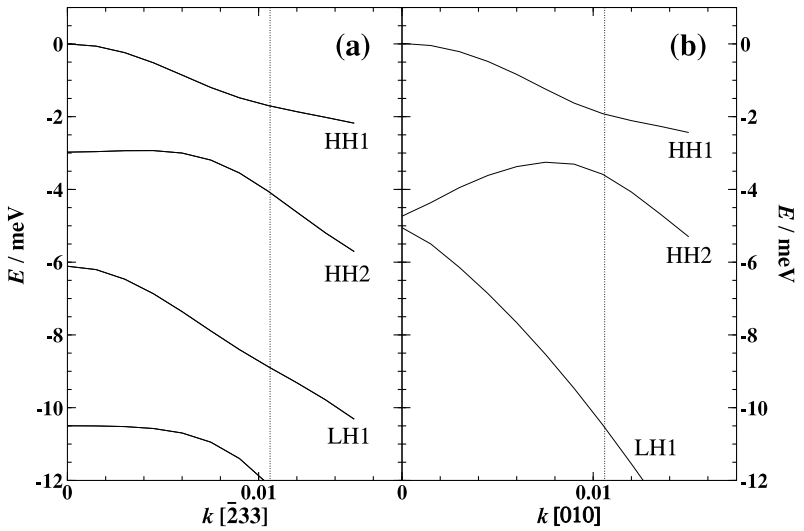

Figure 2.2: HH and LH subbands for 200 Å symmetric quantum wells in the GaAs/AlGaAs material system: (a) Plane of confinement (311); (b) Plane of confinement (100). [Courtesy of Roland Winkler].

Figure 2.2 shows the results of calculations performed in the envelope function approximation in the 8×8 subspace of the $\Gamma_6, \Gamma_7, \Gamma_8$ representations, by Roland Winkler. The details of the calculations are contained in reference [55]; they were calculated in this case using a self-consistently determined inversion-symmetric confinement potential assuming a hole carrier concentration of 1.8×10^{15} m^{-2}, to model T240. For comparison, the calculations were performed with the [311] and [100] directions normal to the plane of confinement, shown in Figs. 2.2(a) and (b) respectively. The vertical dotted lines correspond to the Fermi wavevector of wafer T240, assuming that the Fermi contour is circular. Each subband is two-fold degenerate.

The strong non-parabolicity of the HH and LH subbands is a consequence of their differing curvatures, which causes them to approach one another and then anticross strongly. Hence, the origin of 2D non-parabolicity differs from that in 3D, where the effect is quite subtle. For wavevectors accessible to this experiment, the Fermi contour is close to isotropic [55]. In fact, both the anisotropy and anticrossing of these subbands have been mapped out directly

for (100)- and (311)-oriented quantum wells using hot-electron luminescence [58] and resonant magneto-tunnelling [59, 60]. They confirm the expectation that for $k \leq 0.01$ Å^{-1} the HH1 band may be considered to be isotropic.

In symmetrically-doped quantum well samples, it may be expected that the confinement potential of the particles is symmetric. Hence, the net electric field across the 2DHS is zero. In asymmetrically doped samples, there can be a strong electric field perpendicular to the interface. This lack of inversion symmetry lifts the 'spin' degeneracy of each subband for $k_{||} > 0$. At $k_{||} = 0$, the two-fold degeneracy must remain because of time-reversal symmetry [43].

2.4 Non-zero magnetic field

The application of a magnetic field perpendicular to the interface causes the formation of Landau levels. As anticipated from the anisotropic and non-parabolic properties of the zero-field band structure, the energies of the Landau levels are found to be strongly non-linear functions of $B_\perp$. A theoretical treatment of the problem was first formulated by Ekenberg and Altarelli [51] in the axial approximation.

The k_x and k_y are replaced by the Landau raising and lowering operators

$$a^\dagger = \sqrt{\frac{\hbar}{2eB}}(k_x + ik_y), a = \sqrt{\frac{\hbar}{2eB}}(k_x - ik_y), \tag{2.4}$$

see for example reference [56]. In the presence of a magnetic field, the Luttinger Hamiltonian also gains diagonal terms $\sum_{\alpha=x,y,z} 2\mu_B(\kappa B_\alpha J_\alpha + q_L B_\alpha J_\alpha^3)$ [46]. It is found experimentally that the Zeeman-like κ term dominates the q_L term, which is therefore usually neglected [61]. A suitable ansatz for the four-component wavefunction is now

$$\begin{pmatrix} c_1(z)\phi_{m-1} \\ c_2(z)\phi_m \\ c_3(z)\phi_{m+1} \\ c_4(z)\phi_{m+2} \end{pmatrix}$$

where the ϕ_m are the usual harmonic oscillator functions. In the axial approximation, the ϕ_m may be eliminated to leave a set of coupled differential equations for the $c_i(z)$. A different set is obtained for each choice of m. If $m \geq 1$ then there are four coupled differential equations (and four Landau levels are obtained for that particular value of m). If $m \leq 0$ then some of the coefficients $c_i(z)$ must be set to zero, because (for example) there is no function ϕ_{-1}, and fewer Landau levels are found.

The calculations of Cole *et al.* are reproduced in Fig. 2.3, for a 150 Å asymmetric (311)A quantum well [62]. The integers labelling each level indicate

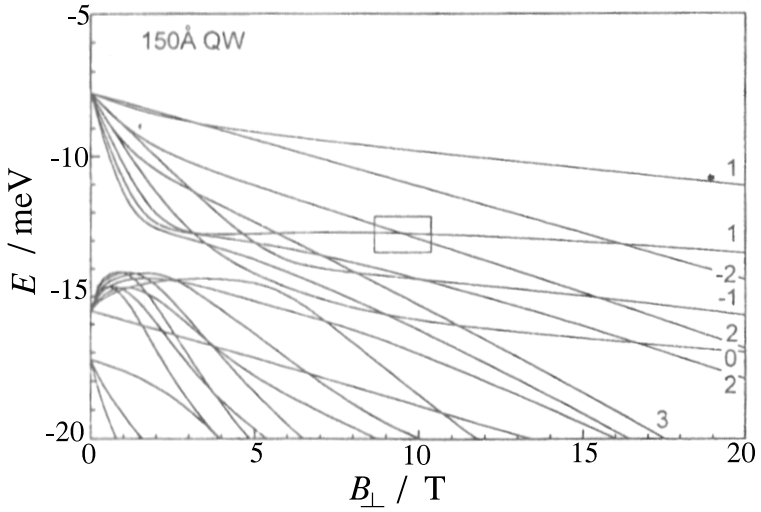

Figure 2.3: HH1 and HH2 Landau levels of a 150 Å (311) asymmetrically-doped quantum well (From Cole *et al.*)

which value of m led to the solution. The levels are separated into two groups, which originate from the HH1 and HH2 subbands of the system at $B = 0$. The HH2 dispersion at low fields has the opposite sign to that of HH1; this is a manifestation of the electron-like dispersion of the HH2 subband at zero B. The strong anticrossing behaviour occurs between Landau levels of the same index but from the different subbands. Note that in the axial approximation, crossing between Landau levels originating from the same $B = 0$ subband is allowed.

The relaxation of the axial approximation has been studied by Bangert *et al.* [63]. An important refinement is that, for (100) systems in the 4×4 approximation, Landau levels from the same $B = 0$ subband with equal (m modulo 4) do not cross. For the lower symmetry (311) planes, it is found that levels with the same index (m modulo 3) also anticross [62]. It should be noted that most of the data presented in later chapters of this thesis are obtained for $B_\perp < 2$ T. Inspection of Fig. 2.3 shows that in this regime, the Landau level dispersion is rather linear. However, it should be borne in mind that the samples studied in this work were about 33% wider, which would decrease the energy separation of the 2D subbands at zero magnetic field and move the complicated anticrossing part of the diagram to lower $B_\perp$.

2.5 Confinement symmetry

The significance of the symmetry of the confinement potential of the 2DHS on its low-field Shubnikov-de Haas oscillations is well known; it was addressed in the first paper reporting the quantum Hall effect in holes [23], and was investigated further soon afterward [64]. Measurements of different samples with approximately symmetric or strongly asymmetric in-grown confinement potentials yield very different low-field ρ_{xx} oscillations. In the asymmetric case, an apparent 'beating' effect is observed whereas in inversion-symmetric samples the Shubnikov-de Haas oscillation amplitudes increase monotonically with $B_\perp$ [64]. The new feature of the results to be presented here is that these symmetry effects may be observed in the *same* sample, on just one cooldown.

2.5.1 Experimental details

This experimental section describes electrical transport measurements of a 2DHS in the T335n+ wafer, subject to a purely perpendicular magnetic field in a ^{3}He cryostat at 0.29 K. Experimental techniques are summarized in Appendix D. The Hall bar studied was oriented in the [$\overline{2}$33] crystallographic direction.

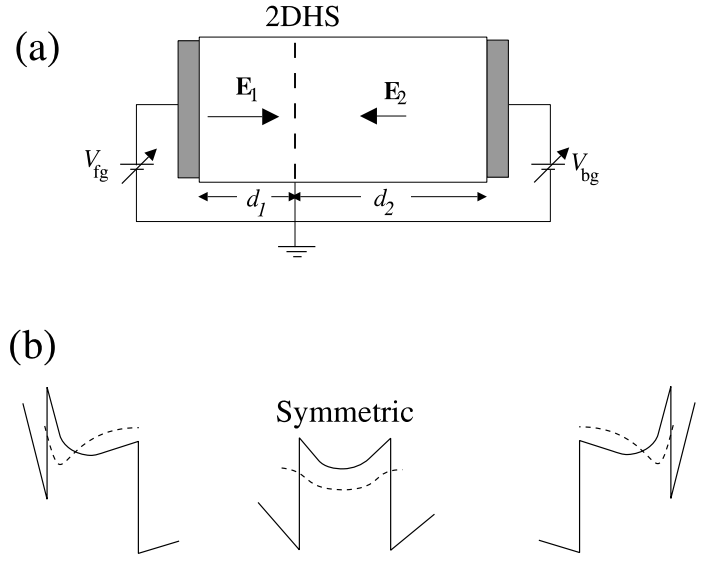

Figure 2.4: (a) Schematic diagram of a front and back gated 2DHS labelled with the distances and voltages discussed in the text. (b) Three confinement potentials, with wavefunctions plotted as the dotted lines, showing the symmetric and asymmetric regimes accessible in a sample with front and back gates.

Wafer T335n+ was grown on a (311)A n+ substrate which can be used as a back gate [65]. In contrast to front gates, which are fabricated by the evaporation of a Schottky contact on to the top surface of a chip thereby covering the Hall bar (see Appendix C), the back gate is situated *underneath* the 2DHS. By applying voltages to front and back gates ($V_{\rm fg}, V_{\rm bg}$ respectively), it is possible to vary the electric field across the 2DHS whilst keeping the hole concentration constant (see Fig. 2.4(a)). In such a sample, it is therefore possible in principle to change the confinement potential of the 2DHS from asymmetric, through to symmetric (with respect to inversion), and then to asymmetric again (Fig. 2.4(b)).

The back gate was found to have a range of $-0.7 < V_{\rm bg}/{\rm V} < 0.5$ with sub-picoamp leakage currents, and was situated approximately 2.7 μm below the 2DHS. In contrast, the front gate was separated from the carriers by 0.34 μm. Simple capacitive arguments using these values show that a change in front-gate voltage $\delta V_{\rm fg}$ requires a change $-\delta V_{\rm bg} = (d_2/d_1)V_{\rm fg} = 8.0 \times \delta V_{\rm fg}$, to keep n constant. In fact, the experimental factor was measured to be (8.8 ± 0.1). This discrepancy cannot be explained by the differing dielectric constants of the materials above and below the 2DHS. Errors of this kind are also observed in front and back gated 2DESs [66], and may arise from redistributions of charge in the doped regions of the device.

2.5.2 Results

Figure 2.5(a) shows $\rho_{\rm xx}$ as a function of $B_\perp$ for a range of front and back gate voltages. Each trace has been offset by an amount proportional to the electric field (due to the gates) across the 2DHS. The minima of each sweep are well aligned at high magnetic fields, indicating that the carrier concentration was constant. The lowest trace, corresponding to $V_{\rm fg} = -0.232$ V, $V_{\rm bg} = -0.7$ V, exhibits smooth electron-like Shubnikov-de Haas oscillations indicating that the confinement potential was close to symmetric. However, the highest trace (corresponding to $V_{\rm fg} = -0.368$ V, $V_{\rm bg} = 0.5$ V), exhibits the beating (with a node at approximately 0.8 T) usually associated with an asymmetric confinement potential. In contrast to the lowest trace, the hole wavefunction is pressed against the top interface of the quantum well. The difference in the electric fields between the two extremes is approximately 4 kVcm^{-1}.

The periodicity of the oscillations (in $1/B_\perp$) may be investigated by inverting the $B_\perp$ axis, and taking the Fourier transform of the data. Figure 2.5(b) shows the padded fast Fourier transforms (FFT) of the data, with each trace offset by an amount proportional to the total electric field due to the gates. The data were tapered before applying the FFT routine to limit 'ringing' effects which arise from the finite range in $1/B_\perp$ of the data.

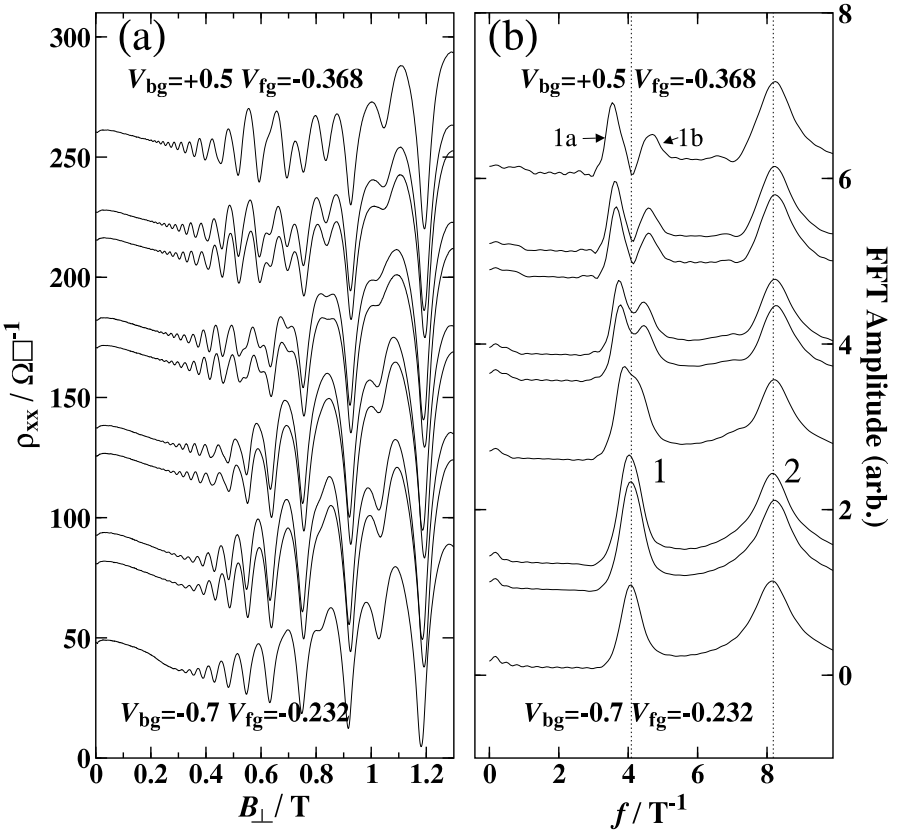

Figure 2.5: (a) ρ_{xx} versus $B_\perp$ measured for a variety of gate-voltage combinations at fixed carrier concentration. The sweeps have been offset vertically by an amount proportional to the electric field induced by the gates across the 2DHS. (b) Fast Fourier Transforms (FFTs) of the data in (a).

The traces show two distinct peaks, marked by the dotted lines. The higher-frequency peak (peak 2) reflects the $1/B_\perp$ periodicity of clearly resolved spin-split Landau levels, and agrees with the carrier concentration measured from the Hall voltage to be $(1.98 \pm 0.04) \times 10^{15}$ m^{-2}. It necessarily contains contributions from the anharmonicity of the Shubnikov-de Haas oscillations. The dotted line at lower frequency was positioned at exactly half the higher frequency; its alignment with peak 1 in the data demonstrates that peak 1 is associated with the spin-unresolved Landau levels which are observed at low magnetic fields. As the back-gate voltage becomes more positive, peak 1 evolves into a pair of clearly resolved peaks (1a and 1b) centred about the frequency of the dotted line.

It is clear that the beating and corresponding splitting of peak 1 observed

in Fig. 2.5 are directly related to the symmetry properties of the confinement potential. In order to determine a pair of gate voltages for which the latter is perfectly symmetric, it is necessary to observe the splitting of peak 1 for both positive and negative electric fields. However, this was not possible at the carrier concentration of the data in Fig. 2.5 because of the limited range in back-gate voltage.

Measurements which show hints of such a splitting, for the same device at slightly lower carrier concentration, are presented in Figs. 2.6(a) and (b). The

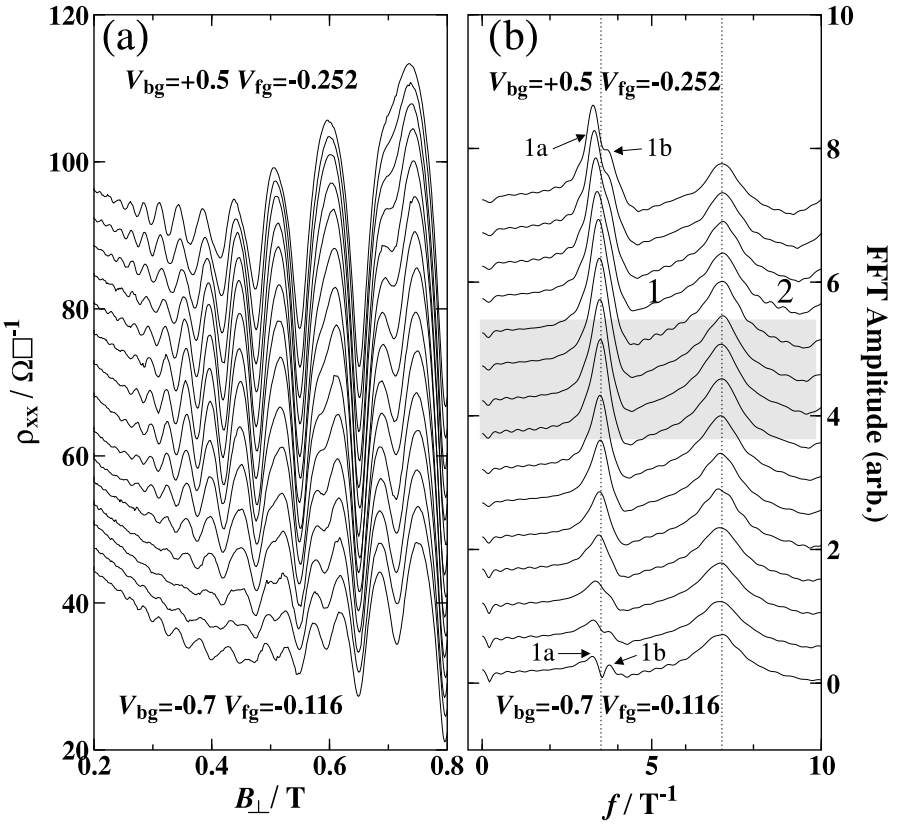

Figure 2.6: Data presented for the same sample, but at a lower carrier concentration than in Fig. 2.5. The Fourier transform traces in (b) indicate a splitting of peak 1 at both large negative and large positive back-gate voltages. The grey box highlights the gate voltages for which the confinement potential is close to symmetric (see text).

average front-gate voltage in these measurements is less negative than in those of Fig. 2.5, which means that the wavefunction of the 2DHS is less attracted to the top hetero-interface. Therefore, the wavefunction is likely to be nearer to symmetric in this case, enhancing the chance that a doublet feature may

be observed at both positive and negative back-gate voltages.

Again, the Fourier transform traces show two distinct peaks, marked by the dotted lines. As before, the line marking the lower-frequency peak (peak 1) was positioned at exactly half the frequency of the higher-frequency peak. The topmost trace again exhibits the doublet structure of the higher traces of Fig. 2.5, labelled 1a and 1b, although in this case it is less well resolved. At the other extreme of the gate-voltage range, and in contrast to Fig. 2.5, peak 1 is split into two peaks again.

2.5.3 Discussion

The explanation of all of these observations lies in the complicated Landau fan diagram of the 2DHS (see Fig. 2.3) [63], and its sensitivity to the symmetry of the confinement potential. As $B_\perp$ is increased, ρ_{xx} oscillates as the chemical potential coincides with the different Landau levels. A node of the beating occurs when the chemical potential passes through two Landau levels simultaneously, which happens when these levels are crossing. The hole Landau fan diagram is characterized by such crossings; and it seems reasonable that by changing the confinement potential, the chemical potential can be tuned to a crossing-point.

A more intuitive explanation relates the splitting of peak 1 to the effect of the symmetry of the confinement potential on the band structure at $B_\perp = 0$ [23, 64]. At zero magnetic field, the two-fold degeneracy of the energy dispersions for $k_{||} > 0$ occurs only if the Hamiltonian has inversion symmetry [43]. If the confinement potential lacks this symmetry, then the degeneracy is lifted. However, at $k_{||} = 0$ there must remain a two-fold degeneracy because of time-reversal symmetry. Thus, in the asymmetric case the HH1 subband effectively splits into a pair of non-degenerate subbands with different curvatures. This is depicted in Fig. 2.7.

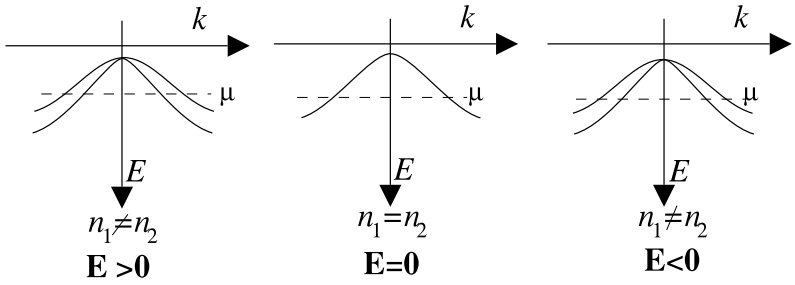

Figure 2.7: A schematic diagram of the variation of the 2D HH1 subband as a function of the electric field across the 2DHS.

In this picture, the application of a perpendicular magnetic field causes the heavier and lighter branches of the HH1 subband to develop into sets of unevenly spaced Landau levels [64]; the beating is caused by the crossing of these Landau levels at low fields, which occurs as the two ladders evolve at different rates as a function of $B_\perp$.

Referring to Fig. 2.4(a), which shows the voltages applied schematically, the magnitude of the electric field $\mathbf{E}$ across the 2DHS may be seen to be:

$$|\mathbf{E}| = \left| \frac{-\delta V_{\mathrm{fg}} + \delta V_{\mathrm{bg}}}{d_1 + d_2} \right|. \tag{2.5}$$

It has been assumed that the $\mathbf{E} = 0$ occurs at some non-zero pair of gate voltages. At constant carrier concentration, this equation reduces to $|\mathbf{E}| = |V_{\mathrm{fg}}/d_1| = |V_{\mathrm{bg}}/d_2|$.

The peaks 1a and 1b of Figs. 2.5 and 2.6 reflect two carrier concentrations, corresponding to the differing occupations of the lighter and heavier HH1 subband (n_1 and n_2 respectively). When the electric field is sufficiently strong, this splitting is resolved in the Fourier transform (see Fig. 2.7). As $\mathbf{E}$ is reduced towards zero by varying the gate voltages, the 1a and 1b peaks merge.

Figure 2.8 plots the splitting of the well-resolved peaks of Fig. 2.5, versus electric field across the quantum well. The figure was constructed by measuring the frequency splitting of peaks 1a and 1b in Fig. 2.5(b). This frequency Δf was converted to a carrier concentration using $\Delta n = n_1 - n_2 = \Delta f \times e/h$.

There is an uncertainty of approximately 10% in the electric field values, because of the differing dielectric constants of the material above and below the 2DHS. Although this splitting is related to the lifting of the degeneracy of the HH1 subband by $|\mathbf{E}|$ [64], it is not possible to convert it into an energy difference without knowledge of the Fermi energy.

The splitting of peak 1 at very negative back-gate voltages in Fig. 2.6(b) could be taken as evidence that the sign of the average electric field across the 2DHS had changed, in which case one of the sweeps at intermediate gate voltages must have been measured for a symmetric confinement potential. The approximate region of symmetric confinement is highlighted in Fig 2.6(b) using the grey box. Features of the data which cast doubt on this interpretation include trends that do not reverse as the symmetric point is passed. More experiments, on samples with greater back-gate voltage ranges, will be required to clarify these observations.

The recent work of Muraki *et al.* [67] describes results similar to the ones presented here. However, they did not observe a splitting of peak 1 at both negative and positive back-gate voltages.

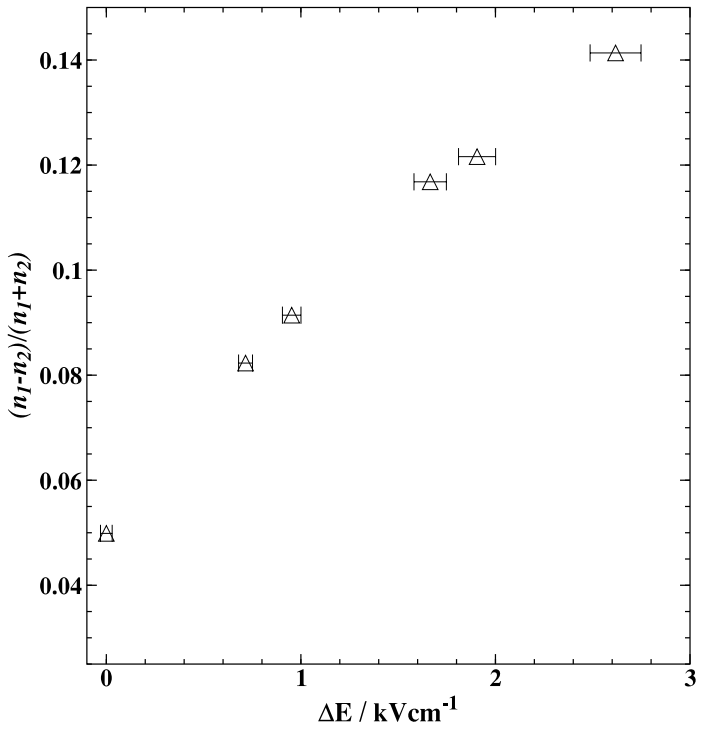

Figure 2.8: Plot of the fractional difference in carrier concentrations of the heavier and lighter branches of the HH1 2D subband, as a function of the changes in electric field induced by the front and back gates. The data points were measured as peak positions 1a and 1b in Fig. 2.5(b)

2.6 Summary

This chapter has described the band structure of the valence band of GaAs, discussing its anisotropy and non-parabolicity in the context of the Luttinger Hamiltonian. The confinement of the holes to two dimensions has been shown to increase the non-parabolicity strongly, due to the anticrossing of adjacent LH or HH 2D subbands. It has been argued that the Fermi wavevector of the samples studied in this thesis are sufficiently small that the Fermi contour may be taken to be close to circular. Calculations performed by Roland Winkler support this idea, and show that the bands deviate significantly from parabolic at the Fermi energy.

The description of the band structure then moved on to the formation of Landau levels in a magnetic field. The labelling scheme of these levels was discussed, as well as their anticrossing properties.

Finally, new experimental data showing the effect of symmetry on the low-

field magnetoresistance were presented. Through the simultaneous use of a front and back gate, to vary the symmetry of the confinement potential at constant carrier concentration, direct evidence of the splitting of subbands at non-zero wavevector was demonstrated.

Chapter 3

Interacting fermions

3.1 Introduction

Much of this thesis is concerned with the effects of Coulomb interactions on transport measurements in the 2DHS. A theory of interactions between particles occupying non-parabolic, anisotropic and strongly mixed bands in two dimensions is non-existent. A pragmatic approach is to treat holes as heavy fermions; at zero magnetic field, these are considered to occupy a simple two-fold degenerate parabolic band. The theoretical results obtained for electrons confined to two dimensions may then be applied to the hole system.

In this chapter, the properties of such particles are described, mainly in the Hartree-Fock approximation (HFA), from zero to high magnetic field. A simple formalism for exchange interactions at integral filling factors is introduced which is then used to describe a first-order phase transition which has been predicted to occur in the 2DS. A discussion of experimental results in Chapter 5 will utilize many of the concepts introduced here.

The penultimate section of this chapter contains a concise review of the literature concerning interaction effects in hole systems.

3.2 The Hartree-Fock approximation

The M-particle wavefunction Ψ of a system of indistinguishable fermions must be antisymmetric with respect to the interchange of any two particles. The single-particle Schrödinger equation is assumed to generate a set of wavefunctions ψ_i of energy λ_i. Starting with the non-interacting case, the many-particle wavefunction may be written as the (Slater) determinant of an $M \times M$ matrix

of the single-particle wavefunctions:

$$\Psi = \begin{vmatrix} \psi_1(\mathbf{r}_1, s_1) & \psi_1(\mathbf{r}_2, s_2) & \cdot & \psi_1(\mathbf{r}_M, s_M) \\ \psi_2(\mathbf{r}_1, s_1) & \psi_2(\mathbf{r}_2, s_2) & \cdot & \psi_2(\mathbf{r}_M, s_M) \\ \cdot & \cdot & \cdot & \cdot \\ \psi_M(\mathbf{r}_1, s_1) & \psi_M(\mathbf{r}_2, s_2) & \cdot & \psi_M(\mathbf{r}_M, s_M) \end{vmatrix} \tag{3.1}$$

where $\mathbf{r}_i$ represents the position of the ith particle, and s_i represents its spin. A property of this wavefunction is that Ψ vanishes as any two particles of the *same spin* approach. However, the separation of particles of different spin is subject to no constraints. Hence, particles of the same spin are on average further apart than particles of opposite spin. The Coulomb energy of interaction of a pair of same-spin fermions is therefore lower than that of opposite-spin fermions. This is the origin of the exchange interaction, which favours aligned spins.

The Hartree-Fock equations are obtained by minimizing the total energy with respect to the ψ_i [68]:

$$-\frac{\hbar^2}{2m_0}\nabla^2\psi_i(\mathbf{r}) \quad + \quad U^{ion}(\mathbf{r})\psi_i(\mathbf{r}) + U^{int}(\mathbf{r})\psi_i(\mathbf{r}) - \sum_j \int d\mathbf{r}' \frac{e^2}{4\pi\epsilon|\mathbf{r}' - \mathbf{r}|}\psi_j^*(\mathbf{r}')\psi_i(\mathbf{r})\delta_{s_i s_j} = \lambda_i\psi_i(\mathbf{r}) \tag{3.2}$$

where U^{ion} represents the attractive Coulomb interaction between the particles and the lattice, and U^{int} the direct, repulsive, Coulomb interaction between the particles. In general this equation is intractable, because of the integral term.

In the case of free particles, which arises when the ionic charge is replaced by a smooth background of charge, plane-wave solutions are found to form an exact solution of equation 3.2. The uniform background is matched by a uniform distribution of free particles (of opposite charge), causing charge neutrality and the cancellation of the U^{ion} and U^{int} terms [68].

This leaves only the 'exchange' integral to be evaluated. This is achieved in momentum space; the solution depends on the dimensionality of the system, through the form of the Fourier transform of the Coulomb interaction. It is conventional to express Hartree-Fock energies in units of the effective Rydberg

$$\mathrm{Ry}^* = \frac{m^* e^4}{2(4\pi\epsilon)^2\hbar^2}. \tag{3.3}$$

In three and two dimensions, the total energies per particle are found to be

[69, 70]:

$$E_{HF}^{3D}/\mathrm{Ry}^* = \frac{2.21}{r_S^2} - \frac{0.916}{r_S}, \tag{3.4}$$

$$E_{HF}^{2D}/\mathrm{Ry}^* = \frac{1}{r_S^2} - \frac{1.2}{r_S}, \tag{3.5}$$

where r_S is the average inter-particle spacing in units of the effective Bohr radius, $a_0^* = 4\pi\epsilon\hbar^2/m^*e^2$. In 2D, $r_S = 1/(a_0^*\sqrt{\pi n})$. The first term represents the kinetic energy, and is inversely proportional to the effective mass of the system. The second term is the energy saving due to exchange, and is independent of the effective mass (when expressed in SI units). These equations show that the relative importance of interactions increases as r_S increases (corresponding to lower carrier density), as the effective mass increases (which quenches the kinetic energy) and as the dimensionality is reduced. For a 2DES with $n = 1 \times 10^{15}$ m^{-2} and $m^* = 0.067m_0$, $r_S = 1.8$. The effective mass of the hole in a 2DHS is not well defined, because of the non-parabolicity of the 2D subbands. An approximate effective mass can be estimated from Fig. 2.2 by expressing the Fermi energy as $\hbar^2k_F^2/2m^*$. This provides $m^* \approx 0.25m_0$, which is rather lower than the values estimated for single-interface heterostructures [64, 9, 71] but is in rough agreement with cyclotron resonance measurements of asymmetric quantum wells [62]. Using this value for the hole effective mass gives $r_S \approx 7$ for the 2DHS. In spite of the obvious crudity of the approximation, this demonstrates that interactions should be expected to be particularly important in the 2DHS.

Because E_{HF} is determined by a variational procedure, it must exceed (or be equal to) the true ground-state energy. The difference is termed the correlation energy; whilst the exchange energy arises from a correlation between particles of the same spin (leading to a lowering of their Coulomb energy), the correlation energy arises from the fact that particles of opposite spin also avoid each other (through Coulomb repulsion).

In the limit of very large r_S, the 2D system is thought to crystallize into a Wigner solid, in which the particles fall onto a triangular lattice. This occurs when the kinetic energy becomes so small that the zero-point kinetic energy ceases to free the particle from the effective confinement potential due to the surrounding electrons and the (smooth) background of dopant charge [16].

Screening at $B = 0$ Screening is a redistribution of charge, in response to an electric field, which acts to lower the energy of the system. At zero magnetic field the Coulomb interaction in 3D electron systems is reduced by screening to a decaying exponential, in the Thomas-Fermi approximation [68]. However,

in the 2D Thomas-Fermi approximation, the screened potential takes the form [21]

$$U(r) \propto \frac{a_0^{*2}}{r^3}. \tag{3.6}$$

Although this is much reduced from its unscreened value, it remains long-ranged and demonstrates that screening strength is diminished significantly by a reduction in dimensionality.

3.3 Strong magnetic field

The measurements to be presented in Chapters 4 and 5 were performed in the quantum Hall regime, in which the density of states is strongly quantized. It is therefore appropriate to introduce a formalism for treating the exchange interaction at integral filling factors. In most of the remainder of this chapter, it will be assumed that the 2DS has zero thickness (i.e. it is ideal), that the density of states is well described by a sum of delta functions, and that the sample temperature is zero.

In a strong perpendicular magnetic field $B_\perp$, the length scale which characterizes inter-particle interactions is the magnetic length l_B, which is defined to be

$$l_B = \sqrt{\frac{\hbar}{eB_\perp}}. \tag{3.7}$$

The corresponding scale of the Coulomb energy per particle, and the exchange interaction E_X in particular, is

$$E_X = \frac{1}{4\pi\epsilon}\frac{e^2}{l_B}. \tag{3.8}$$

The particles now occupy the lowest energy Landau levels of the system, which are labelled by the two quantum numbers N and s. N is an integer denoting the harmonic-oscillator quantum number of the single-particle wavefunction (see Section 1.5.1), whilst s represents the spin of the Landau level. The non-interacting energy of a particle takes the form

$$E = \hbar\omega_C(N + \frac{1}{2}) + g\mu_B \mathbf{B}.\hat{\mathbf{s}}. \tag{3.9}$$

Consider the interaction between a single particle occupying the Landau level with $N = i$, and all of the particles in the full Landau level with $N = j$. The exchange interaction reduces the energy of the particle by an amount

A_{ij} if the spins of the two Landau levels are the same. In the Hartree-Fock approximation in the quantum limit ($E_X \ll \hbar\omega_C$), these 'exchange coefficients' may be calculated to be [72]:

$$A_{ij} = \frac{1}{4\pi\epsilon}\frac{e^2}{l_B}\frac{j!}{i!}\int_0^\infty \sqrt{2}\exp(-k^2)(k^2)^{i-j}[L_i^{i-j}(k^2)]^2 dk \tag{3.10}$$

where L_i^α is an associated Laguerre polynomial [73] and $i \geq j$. The exchange self-energy of a particle in Landau level N is therefore a sum of its exchange interactions with all occupied same-spin Landau levels. The total energy of the particle may be expressed as

$$E_{Ns} = \hbar\omega_C(N + \frac{1}{2}) + g\mu_B \mathbf{B}.\hat{\mathbf{s}} - \sum_i A_{Ni}\rho_i^s, \tag{3.11}$$

where ρ_i^s represents the fractional filling of the ith Landau level with spin s.

3.3.1 Single-particle excitations

An example of an excitation of a system at integer filling factor is the promotion of a particle from the highest (fully) occupied Landau level to the nearest unoccupied one; this is depicted schematically in Fig. 3.1(a). The system may now be described in terms of a 'magnetoexciton' composed of a quasiparticle in Landau level $N + 1$ and a quasihole (of opposite sign) in Landau level N [74].

The energy of these two quasiparticles is defined to be the excitation energy Δ_ν, where ν represents the filling factor of the ground state. To the interaction part of this, there are three contributions [74]: (i) the Coulomb energy due to the attraction between them; (ii) the exchange energy of the particle minus the exchange energy of the hole; (iii) an exchange term arising from the overlap of the particle and hole wavefunctions. Thus Δ_ν depends on the spatial separation of the particle and hole. In the Landau gauge, one component of the wavevector $\mathbf{k}$ is a good quantum number; the magnitude of k is related to the displacement of the guiding centre from the origin. If the excited particle has a wavevector k then the (single particle) wavefunction of the hole has wavevector $-k$; the particles are therefore displaced from one another. Thus the k value of the excitation is proportional to the separation of the particles, so Δ_ν is a function of the wavevector of the magnetoexciton.

The exchange contribution to the dispersion relation $\Delta_\nu(k)$ of the magnetoexciton for the excitation at $\nu = 2$ is reproduced in Fig. 3.1(b) from reference [74]. Terms (i) and (iii) vanish as k tends to infinity, because the particle and hole do not interact in this limit. Thus, the asymptotic value of the dispersion relation is determined by the difference in exchange energies of

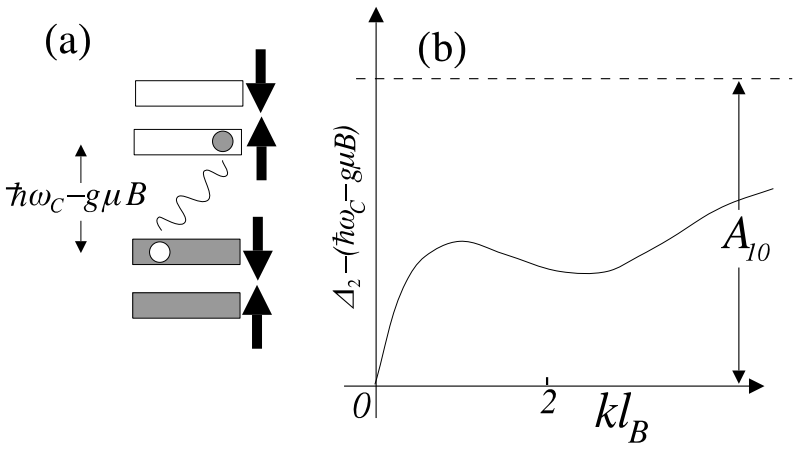

Figure 3.1: (a) An example of a single-particle excitation at $\nu = 2$. The quasiparticle and quasihole created interact, unless they are infinitely separated. (b) Schematic reproduction of the interactions contribution to the single-particle excitation energy at $\nu = 2$. At large k values, the excitation energy is enhanced by the difference in self-energies of the excited particle in the two levels.

the particle in the two Landau levels; this is the limit probed by most transport measurements at integral filling factor. At odd filling factors $\nu = 2N + 1$, the single-particle excitation energy is given by

$$\Delta_{2N+1} = g\mu_B B + A_{NN} \tag{3.12}$$

and at even filling factors $\nu = 2N + 2$ it is

$$\begin{aligned} \Delta_{2N+2} &= (\hbar\omega_C - g\mu_B B) + \sum_{i \le N} A_{Ni} - \sum_{i \le N} A_{(N+1)i}, \\ &= (\hbar\omega_C - g\mu_B B) + A_{(N+1)N}. \end{aligned} \tag{3.13}$$

The latter step results from the orthogonality properties of the associated Laguerre polynomials in two dimensions.

At both even and odd integral filling factors, the energy gap to single-particle excitations has been increased above the non-interacting values by the exchange interaction. At odd filling factors, this is the famous exchange enhancement of the g factor [75, 72].

Screening in a field In the quantum limit, in the absence of disorder and at very low temperatures, screening at integer filling factors is strongly inhibited because of the energy gaps at the chemical potential, which prevent charge

redistribution in the plane. However, the quantum limit is reached only at very high magnetic fields and in many practical examples of 2D electron and hole systems, $E_X \geq \hbar\omega_C$. This leads to mixing of the Landau levels, which permits screening because the Landau levels are then essentially partially occupied [76]. Thus, Landau level mixing reduces the values of the exchange coefficients. Interactions are also softened by disorder, which broadens the density of states of the Landau levels, thereby introducing gapless excitations.

3.4 Spin-polarization instability

In the simplest Hartree-Fock approximation, the ground state of a system of M fermions in a strong magnetic field may be specified using a set of occupation numbers for each Landau level. The incorporation of the exchange interaction can cause the particular lowest energy set of occupation numbers to be different from the intuitively obvious non-interacting set.

To investigate this, we consider the total energy per particle of a system at integral filling factor $\nu = 2N + 2$, depicted in Fig. 3.2. Using the notation developed earlier, it may be written as

$$E = \left(\sum_{i,s} (\hbar\omega_C (i + \frac{1}{2}) + g\mu_B \mathbf{B}.\hat{\mathbf{s}}) \rho_i^s - \frac{1}{2} \sum_{i,j,s} A_{ij} \rho_i^s \rho_j^s \right) / \nu. \tag{3.14}$$

At zero temperature, the ground state of the system may be determined by minimizing this quantity.

In the absence of interactions the $\{A_{ij}\} = 0$ and the lowest energy state is clearly given by $\rho_i^{\pm} = 1$ for $i \leq N$, and $\rho_i^{\pm} = 0$ for $i > N$. For sufficiently weak interaction energies, this remains the ground state (see Fig. 3.2(a)). Because the initial state is of even filling factor, its spin-polarization (or magnetization) is zero.

Figure 3.2(b) depicts the transfer of all of the particles in the highest occupied Landau level to the nearest unoccupied one, which has opposite spin. This process increases the magnetization of the system; it is conventional to describe the unmagnetized state as paramagnetic, and the magnetized state as ferromagnetic. The transfer of particles increases the number of same-spin fermions in the system, and might be expected to lower the interaction energy. For the cases $\nu = 2$ and $\nu = 4$, the differences in total interaction energy between the paramagnetic and ferromagnetic states are:

$$\Delta_{P,F} = \left(\frac{A_{00}}{2} - (\frac{A_{11}}{2} + A_{10}) \right) / \nu \tag{3.15}$$

and

$$\Delta_{P,F} = \left(\frac{A_{11}}{2} + A_{10} - (\frac{A_{22}}{2} + A_{20} + A_{21}) \right) / \nu \tag{3.16}$$

respectively. If the $\{A_{ij}\}$ are calculated in the extreme quantum limit, then

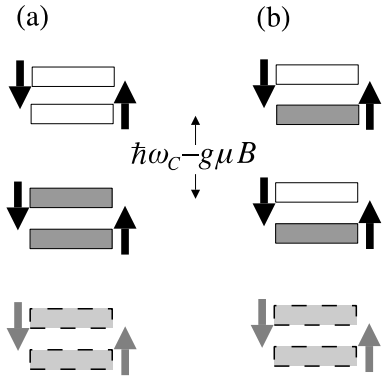

Figure 3.2: Filled and empty Landau levels at even filling factor. (a) The paramagnetic state in which the spin-polarization (or magnetization) is zero. (b) The ferromagnetic state, which has non-zero magnetization.

in both cases the total interaction energy of the system does become more negative.

The transfer of particles to the higher Landau level costs $\hbar\omega_C - g\mu_B B$ of non-interacting energy per particle. In real systems this energy usually outweighs the saving that would be made in interaction energy, and the transfer is not favoured.

However, the tilted-field measurement (see Section 4.2.1) allows the experimental variation of the quantity $\hbar\omega_C - g\mu_B B$ at fixed filling factor. Thus, there can arise a situation in a 2D system in which

$$\Delta_{P,F} + \hbar\omega_C - g\mu_B B = 0. \tag{3.17}$$

At this point, the total energies of the unmagnetized and magnetized ground states are equal. Any further tilting favours the magnetized state.

The change in magnetization of the system occurs discontinuously, and therefore may be described as a first-order paramagnetic-ferromagnetic phase transition. This effect was first discussed by Giuliani and Quinn [77, 78, 79] in the context of the 2DES. These papers consider more general ground states, in which the limit $\Delta_\nu(k) \to \Delta_\nu(\infty)$ is not assumed initially. Thus, transitions to spin-density wave (SDW) states are also allowed. However, they find that the first-order phase-transition pre-empts the SDW state in single-valley materials.

3.4.1 Measured energy gap

The energy gap measured in an experiment by activation-energy techniques (see Section 4.2.1) does not provide direct information about the total energy of the system. Instead, it provides an estimate of the single-particle excitation gap.

Referring to Fig. 3.3(a), and specializing to the $\nu = 2$ case, we see that before the transition the single-particle excitation energy is

$$\Delta_2 = \hbar\omega_C - g\mu_B B + A_{10} \tag{3.18}$$

from equation 3.13. At the transition point, $\hbar\omega_C - g\mu_B B + \Delta_{P,F} = 0$. Substituting this into equation 3.18 gives

$$\Delta_C = 2A_{10} + \frac{A_{11}}{2} - \frac{A_{00}}{2}. \tag{3.19}$$

Thus, the theory predicts that the measured energy gap at the transition point is greater than zero.

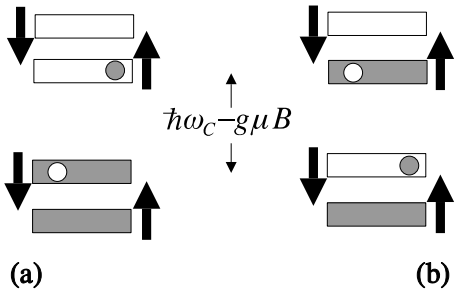

Figure 3.3: Model system at $\nu = 2$ showing single-particle excitations in the paramagnetic (a) and ferromagnetic (b) phases.

As a check, the energy gap may be calculated on the ferromagnetic side of the transition. In this case, referring to Fig. 3.3(b), the single-particle energy gap is given by

$$\Delta_C = g\mu_B B - \hbar\omega_C + A_{11} + A_{10} = \frac{A_{00} + A_{11}}{2}. \tag{3.20}$$

Substitution of the values obtained for the A_{ij} shows that expressions 3.19 and 3.20 are the same. At $\nu = 4$, the single-particle energy gap takes the value $(A_{11} + A_{22})/2$.

Therefore the simplest incorporation of the exchange interaction into a tilted-field experiment makes the following predictions: (i) at a certain critical value of $\hbar\omega_C - g\mu_B B$, a magnetization instability occurs in which the system lowers its ground-state energy by transferring the particles from the highest occupied Landau level to the nearest unoccupied one (which has opposite spin); (ii) the energy gap, Δ_C, at which this occurs is more than zero; (iii) the measured energy gap is continuous, but its derivative (with respect to B) is not.

Non-zero temperature, and disorder In the *non-interacting* case at zero temperature, the change of phase occurs abruptly when $\hbar\omega_C = g\mu_B B$ and the magnetization changes discontinuously. However, it is clear that an infinitesimal increase in the temperature removes the discontinuity in the magnetization. Therefore, the phase-transition is not first-order at realistic temperatures in a non-interacting system.

At temperatures sufficiently high that the Landau levels above the chemical potential become significantly occupied, exchange effects begin to be quenched. However, for non-zero temperatures below a certain critical temperature, the magnetization may still be expected to exhibit discontinuities at the change of phase. Thus, the phase-transition can remain first order in an interacting system at realistic temperatures. The change of order of the phase-transition occurs for $k_B T \approx E_X$.

The effect of disorder, and the extra screening that it introduces, have been investigated in reference [80], which shows that for small amounts of disorder, the phase-transition remains first-order.

3.5 Interacting holes

The theory of interactions between holes is complicated by the properties of the non-interacting valence band described in Chapter 2. There exists no theory which incorporates both the full Coulomb interaction and the anisotropy and non-parabolicity of the valence band, even in three dimensions.

In three-dimensional systems, the first theory treating hole-hole interactions was published by Combescot *et al.* [81]; this paper described the ground state of an electron-hole plasma, created by optical pumping, in Ge. It contains a derivation of the Hartree-Fock energy of the 3D isotropic hole system, resulting in an exchange energy per hole of

$$E_X = -\xi(w)\frac{0.916}{r_S}, \tag{3.21}$$

where w represents the ratio between the LH and HH Fermi wavevectors. The function $\xi(w)$ varies monotonically between the limits $\xi(0) = 0.71$ and $\xi(1) = 0.79$ [81]. Comparison of equation 3.21 with the exchange part of the 3D electronic result (equation 3.4) shows that the electron and hole results differ by the factor $\xi(w)$, which is of order unity. The difference arises because the angular momentum of the valence band (which *is* a good quantum number in the spherical approximation) has $J = 3/2$, rather than $J = 1/2$ as in the case of electrons, making the exclusion principle less effective. Even in the limit of zero LH mass, $w = 0$, the electron result is not obtained because the Coulomb interaction couples light and heavy holes [82].

Other results of importance include calculations of band-gap renormalization in both the bulk [83] and in quantum wells [84]; these are of importance in optical experiments.

A recent paper [85], concerning the 2DHS formed in p-type inversion and accumulation layers in Si, presents density-functional calculations of the hole band structure, and also a useful review of the theory to date on the subject of the 3DHS. A sister-paper [86] presents density-functional calculations of the Landau levels of the 2DHS. It represents the only theoretical treatment of the problem of inter-hole interactions in a strong magnetic field. However, the exchange-correlation potential is calculated at zero magnetic field. This work does not treat the problem of single-particle excitations from full Landau levels, and is therefore rather difficult to apply to our work.

A further calculation of the effects of exchange and correlation on the zero-field band structure of the 2DHS in the GaAs/AlGaAs material system may be found in reference [82].

Early experimental observations of interaction effects involving the valence band include band-gap renormalization, which is observed in doped quantum wells [87]. Other experimental observations of many-body effects are listed below.

Although exchange is the simplest interaction effect, and in spite of its direct relevance to the excitations of the system, there have been few experimental observations or studies of its effects in low-dimensional hole systems.

The Zeeman splitting of the exciton spectrum, probed optically in unoccupied quantum wells, contains a contribution due to the exchange interaction between the overlapping electron and hole wavefunctions [88]. Traynor *et al.* [89] suggest that discrepancies observed between an 8×8 $\mathbf{k}.\mathbf{p}$ calculation and their experimental results for wide quantum wells are due to extra mixing of LH and HH states by the Coulomb interaction.

In transport experiments, Coleridge *et al.* [90] claim to observe enhanced excitation gaps at even and odd filling factors, in the 2DHS formed at the

Si/SiGe interface. A recent paper by Kemerink *et al.* [91] presents a comparison of the Shubnikov-de Haas oscillations of a narrow quantum well, in the GaAs/AlGaAs material system, with non-interacting **k.p** calculations. It was shown that non-interacting calculations of the Landau levels using the 4×4 Luttinger Hamiltonian could not account for the temperature dependence of ρ_{xx} oscillations (with $B_\perp$), and that the discrepancies could be attributed to an exchange enhancement of these energy gaps (see Section 3.3.1). A more direct transport observation of the exchange interaction at $B = 0$ is reported in reference [92], which describes compressibility measurements in a bilayer hole system.

The most striking experimental manifestation of hole-hole interactions in the 2DHS is certainly the fractional quantum Hall effect, which was described in Chapter 1, and originates from correlations.

Measurements [62, 93] of anomalous temperature shifts of the cyclotron resonance frequencies in the 2DHS, at high magnetic fields, have been attributed to Coulomb-coupled single-particle inter Landau level transitions, of the type first described by Cooper and Chalker [94].

The Wigner crystal phase of the 2DS is a correlation effect which is thought to occur at unattainable values of r_S in the 2DHS at $B = 0$. However, the application of a strong perpendicular magnetic field can induce its formation in high-quality systems. A possible observation of this effect has been reported in reference [95], where an insulating phase is observed in the range $1/3 < \nu < 2/5$. A magnetically-induced Wigner crystal may also have been detected in photo-luminescence experiments in low-disorder 2DHSs [96].

Other possible effects arising from interactions between holes include the observation of insulating phases in the vicinity of $\nu = 1.5$, in the SiGe based 2DHS (see for example reference [97]), and the observation of a insulator-conductor phase transition as the carrier concentration of the 2DHS is reduced [98].

Chapter 4

Tilted magnetic field studies: experiment

4.1 Introduction

This chapter presents the results of a series of experiments performed on single 2DHSs confined to symmetrically-doped quantum wells, in tilted magnetic fields. The energy gaps of the 2DHS at fixed even and odd filling factors have been measured as a function of the angle of tilt, using the activation-energy method. These are found to increase and decrease in accordance with a simple picture of Landau levels of well defined spin, despite the complexities of the valence band structure.

However, in disagreement with the simplest of these pictures, the Landau levels do not cross. Instead, turning points are observed before the energy gap reaches zero. In the case of filling factor $\nu = 4$, it is observed that within the experimental error the energy gap Δ_4 (measured using an activation technique) is an approximately linear function of B right up to the turning point. The significance of this result, and a discussion of the physics of the system, are delayed until Chapter 5.

4.2 Tilted magnetic field

4.2.1 Basic concepts

This section begins with a description of the properties of a simple two-dimensional system with electron-like bands. The properties of the 2DHS in a tilted magnetic field are discussed fully in the next chapter.

The density of states of a zero-thickness 2DS of non-interacting free fermions subject to a strong, arbitrarily oriented, magnetic field forms a set of Landau

levels whose separation is determined by $B_\perp$, the component of B perpendicular to the plane. However, the spin degree of freedom couples to the total magnetic field. The generic energy gap Δ at the chemical potential of a non-interacting system may be written as

$$\Delta = \hbar\frac{eB_\perp}{m^*} - g\mu_B B \tag{4.1}$$

at even filling factors. $B_\perp$ and B may be varied independently by changing the parallel component of B; experimentally, this may be realized by tilting the sample with respect to the axis of the solenoid (see Fig. 4.1).

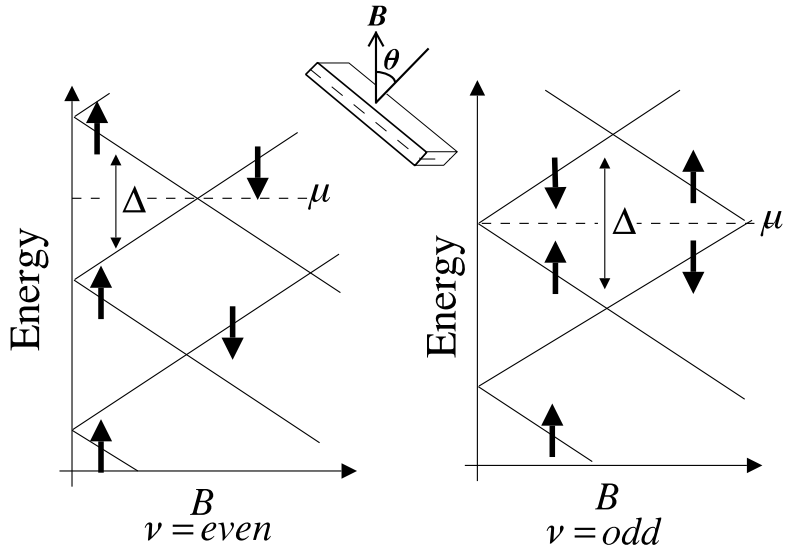

Figure 4.1: The effect of tilting the sample with respect to B, whilst keeping $B_\perp$ constant at either even or odd filling factor. Landau levels are represented by solid lines. Their 'spin' is depicted using arrows. Centre: Schematic diagram indicating the orientation of the sample with respect to B. A more realistic diagram for a 2DHS is provided in Fig. 5.1

Real systems are only quasi-two-dimensional. In the case of symmetric confinement, their thickness is best characterized by the half-width of the wavefunction, λ_z', in the confinement direction. The physics of the system remains two dimensional in the limit that the magnetic length $l_B \gg \lambda_z'$, whilst the three dimensional limit is reached when $l_B \ll \lambda_z'$. While the two-dimensional limit is maintained, properties of the 2DS such as the disorder broadening of Landau levels and the Coulomb interaction between particles, are independent of the parallel magnetic field.

The measurement of energy gaps in the quantum Hall regime using temperature dependences is commonplace in the literature; see Nicholas *et al.* [99], Usher *et al.* [100] and Schmeller *et al.* [101]. The so-called Arrhenius (or activation-energy) technique, in which the diagonal conductivity σ_{xx} of a 2DS is assumed to be activated according to the equation

$$\sigma_{xx} = \sigma_0 \exp\left(\frac{-\Delta}{2k_B T}\right), \tag{4.2}$$

is based on the idea that σ_{xx} is determined by the number of particles excited by the temperature into the nearest unoccupied Landau level. The prefactor σ_0 represents a minimum metallic conductivity, which is only weakly dependent on temperature. Early uses of this method include references [102] and [103]. Equation 4.2 requires that the density of states is composed of a series of delta function Landau levels and that $k_B T \ll \Delta$. Relaxation of either of these requirements changes equation 4.2. The consequences on the shape of $\ln \sigma_{xx}$ versus $1/T$ plots are discussed in section 4.3.3.

σ_{xx} can be measured directly using the Corbino disc geometry. However, Hall bars are experimentally more convenient because they offer a choice of ohmic contacts and allow both ρ_{xx} and ρ_{xy} to be measured; they were therefore utilized here. Experimental data may be converted from ρ_{xx} to σ_{xx} using the following relationship (see Section 1.4.2):

$$\sigma_{xx} = \frac{\rho_{xx}}{\rho_{xx}^2 + \rho_{xy}^2}. \tag{4.3}$$

4.2.2 Previous work

The ability to affect the spin and space degrees of freedom independently was first exploited by Fang and Stiles [104] to probe the g factors of the electron in silicon inversion layers. Of the many experiments since, one the most complete in the GaAs/AlGaAs system has been by Nicholas *et al.*, which demonstrated the effect of the exchange interaction on the energy gaps at odd filling factors in the 2DES. However, tilted magnetic field studies in the 2DHS are rarer. Experiments to date include reference [105], which presented two traces of the ρ_{xx} oscillations at non-zero tilt angles. The aim of that experiment was to investigate the spin splitting of the Shubnikov-de Haas oscillations in their beating regime (see Chapter 2), and showed the apparent independence of the traces to the parallel magnetic field. This was interpreted theoretically in terms of the decoupling of light and heavy hole states in the narrow well [106]. Other work published has been on the effect of a tilted field on the fractional quantum Hall effect of the GaAs/AlGaAs 2DHS [9, 30, 107], and a series of papers on the SiGe 2DHS [108, 90, 97]. A brief paper [109] presented a

comparison of theory and experiment for the effect of a parallel magnetic field on the Landau levels of a GaAs/AlGaAs 2DHS. Relevant papers are discussed in the context of this work in the next chapter.

4.3 Experimental details

4.3.1 Samples

Sample chips of wafers T240 and T335n+ were studied. Some of their properties are reproduced in table 4.3.1. They were surface processed (see Appendix C)into Hall bars; neither was front gated, but T335n+ was grown on an n+ substrate. The data obtained in the lengthy temperature-dependence

Wafer	n / 10^{15} m^{-2}	μ_{tr} / m^2/Vs	Well width / Å
T240	1.8±0.02	130±10	200
T335n+	1.3±0.02	56±2	200

experiments came from samples which were oriented with the current flowing in the $[01\overline{1}]$ direction (T240) or $[\overline{2}33]$ direction (T335n+); the axis of rotation was parallel to the current. The holes were confined to 200 Å quantum wells, giving a characteristic half-width of the wavefunction of approximately 80 Å. The magnetic length at the maximum available field of 12 T is 74 Å. Thus, at the highest fields, diamagnetic effects might be expected to become important. However, the 3D limit is certainly not reached.

4.3.2 Apparatus and measurement

Measurements were performed in a ^{3}He cryostat with a base temperature of approximately 270 mK. The temperature was controlled using an Oxford Instruments ITC4 temperature controller. The temperature was measured at zero magnetic field using a calibrated Ge thermometer; care was taken to avoid self heating by the excitation current. However, most of the measurements presented below were performed at non-zero magnetic fields, where the strong magnetoresistance of Ge prevents the use of such thermometers. In this case, the sample temperature was measured using a carbon 470 Ω 'Speer' resistor calibrated at $B = 0$ to the Ge thermometer. The relationship between the ITC4's calibration of the Speer and the Ge thermometer was found to be close to linear, between 0.3 K and 0.75 K (there were slight oscillatory deviations from linearity).

The magnetoresistance of the 470 Ω Speer resistor is small, but not negligible. It has been investigated thoroughly for magnetic fields up to 14 T in reference [110], and leads to total errors of less than 7% below temperatures of 1.5 K. The base temperature of the cryostat was found to be independent of time, twelve or more hours after the condensation of the ^{3}He. This enabled the B dependence of the Speer thermometer at base temperature to be determined accurately (eddy-current heating was avoided using low magnet sweep rates). The error measured at base temperature is plotted as a function of B in Fig. 4.2 as the two lines without symbols (marked 0.3 K). The other lines (with symbols) represent the B-dependent errors at higher temperatures, quoted from the literature [110]. T_0 has been defined to be the actual temperature of the thermometer, and T is the temperature deduced from its resistance using the zero-field calibration.

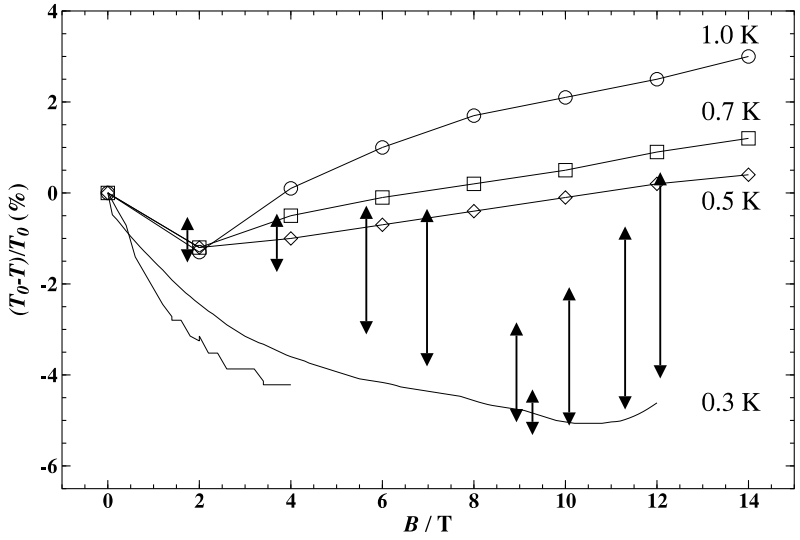

Figure 4.2: Percentage error in temperature $(T_0 - T)/T_0$ versus magnetic field. Symbols represent typical values for a 470 Ω Speer resistor, quoted in the literature at 0.5, 0.7 and 1.0 K. The two curves are data taken at 0.3 K. The arrows represent the ranges of temperatures used in section 4.5.1

The *in situ* rotation of the sample was achieved manually using a sample holder built by Oxford Instruments with a 'Swedish rotator' drive mechanism, providing a high degree of reproducibility, and very little hysteresis. The angle of tilt, as determined from the periodicity of the ρ_{xx} oscillations, was linearly related to the number of turns of the screw and agreed closely with the angle deduced from the linear portion of the Hall voltage. This demonstrates that

the assumptions concerning the two-dimensionality of the sample are justified.

The activation technique for the determination of the energy gap at the chemical potential requires the accurate measurement of small resistances. This is obviously facilitated by the use of high excitation currents. However, it is important to prevent Joule heating of the hole system. Below excitation currents of 38 nA, no change in the visibility of the magnetoresistance oscillations at low or high fields could be detected at base temperature (although the signal-to-noise ratio decreased). Above 38 nA, heating effects became apparent. In this work, constant currents of either 37.5 nA or 30 nA were employed.

Of crucial importance in the activation method is the elimination of offset voltages. There are at least two causes: (i) intrinsic offset on the output of the lock-in amplifier (LIA) when the inputs are shorted together; (ii) noise, which necessitates an increase in the dynamic reserve of the LIA and introduces an extra offset (see Appendix D). Both of these causes depend on the specific settings of the LIA; the former may be eliminated by measuring the offset regularly throughout the course of the experiment. The latter, however, is particularly difficult to control. The method employed in this work was to simplify the measurement circuit to just one LIA, measuring the diagonal resistance R_{xx}.

It is necessary to ensure that the LIA remains in phase throughout the temperature range. Bad ohmic contacts can change the phase of the measured signal as their resistance changes with temperature (the measuring circuit provides a stray capacitance). Such effects were minimized for these samples by carefully assessing the qualities of the available ohmic contacts.

Activation data obtained in one experiment are presented in Fig. 4.3. They show that, with appropriate care, linear plots of $\ln \sigma_{\mathrm{xx}}$ versus $1/T$ may be obtained. A detailed examination of the figure shows a slight kink in the line at $1/T = 2\ \mathrm{K}^{-1}$: this is due to the oscillatory deviation of the ITC4 Speer calibration from the true temperature. It is very difficult to eliminate, but does not cause a significant error. Slight time-dependent variations in the LIA offset, and the possibility of phase problems, made measurements of $R_{xx} < 2.5\ \Omega$ unreliable: for the purposes of data analysis, measurements below this threshold were discarded.

4.3.3 Deviations from ideal activation

It is convenient to consider first a model system in which there are $2\mathcal{N}$ microstates, labelled by $1 \leq i \leq 2\mathcal{N}$. $\mathcal{N}$ of these states are assumed to be degenerate with single-particle energies $-\Delta/2$, whilst the other $\mathcal{N}$ states are also degenerate but with energies of $\Delta/2$. Thus, the two levels represent

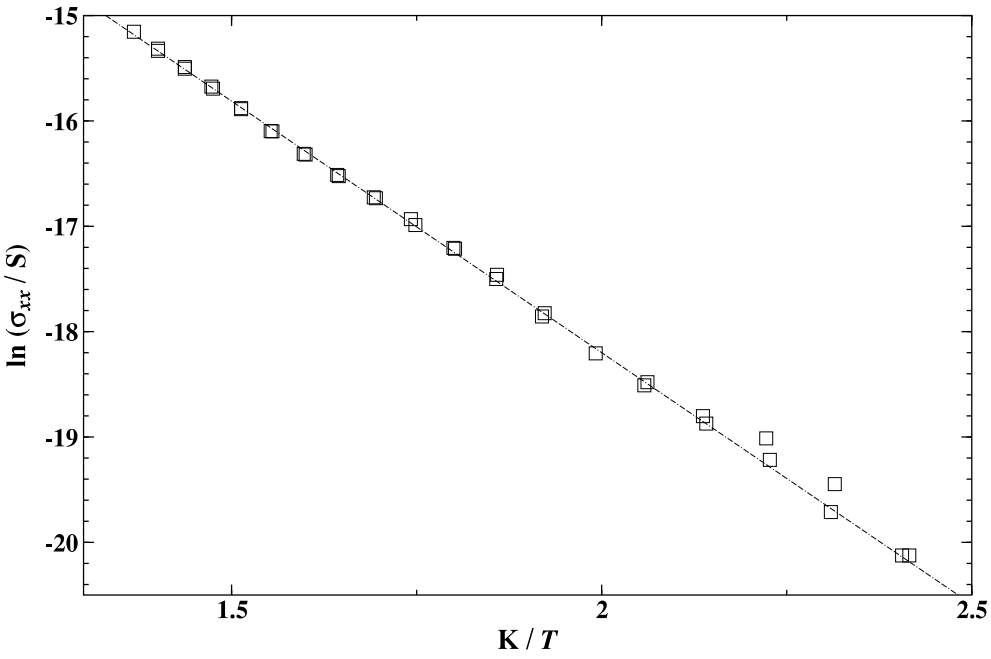

Figure 4.3: Plot of $\ln \sigma_{\rm xx}$ versus $1/T$ from experiment. The data are close to linear over the whole temperature range.

highly degenerate Landau levels. There are assumed to be $\mathcal{M}$ indistinguishable fermions in this system (clearly with $\mathcal{M} < 2\mathcal{N}$). The probability that a particular single-particle state i is occupied is given by the Fermi-Dirac distribution

$$f(E) = \frac{1}{1 + e^{\beta(E-\mu)}} \tag{4.4}$$

where $\beta = 1/k_B T$ and μ is the chemical potential. By conserving particle number, an implicit equation for μ is determined

$$\mathcal{M} = \frac{\mathcal{N}}{1 + e^{\beta(\Delta/2-\mu)}} + \frac{\mathcal{N}}{1 + e^{\beta(-\Delta/2-\mu)}}. \tag{4.5}$$

Therefore, in principle, the chemical potential is a function of temperature. However at integral filling factor ($\mathcal{M} = \mathcal{N}$) it is trivial to show that $\mu = 0$ (i.e. mid-gap) for all temperatures. The diagonal conductivity is then assumed to be proportional to the occupation of the higher state, and the following equation is obtained:

$$\sigma_{\rm xx} \propto \frac{1}{1 + e^{\Delta/2k_B T}}. \tag{4.6}$$

In the low temperature limit, equation 4.2 is regained, and an activation plot will yield a straight line. However, at high temperatures, the activation plot becomes sub-linear because of the constant term in the denominator of equation 4.6. A suggestive flattening off may be observed at low $1/T$ in the experimental data presented in Fig. 4.7. However, the curvature observed there proved to be too strong to fit to the above theory. A plausible mechanism for the experimental flattening off is a change in the effective mobility of the particles involved in the conduction. At sufficiently high temperatures, this mobility may be expected to drop, thereby introducing a temperature dependent pre-factor into equation 4.6.

Incorporating scattering effectively lifts the degeneracy in each Landau level. The density of states $D(E)$ is then introduced to facilitate the counting of the states. The density of states for a real system of Landau levels is discussed in Chapter 1. It is assumed here that the delocalized states occupy a region of total width Γ in energy. Thus $D(E)$ is implicitly assumed to represent the transport density of states. Functional forms which incorporate the physics of a mobility edge include the top-hat function or the Gaussian distribution. It is convenient to define $D(E) = d_+(E) + d_-(E)$ where d_+ and d_- represent the suitable approximations for the densities of states of the two separate Landau levels. Explicitly,

$$d_\pm(E) = \begin{cases} \mathcal{N}/\Gamma & \text{for } (\pm\Delta/2 - \Gamma/2) < E < (\pm\Delta/2 + \Gamma/2) \\ 0 & \text{elsewhere,} \end{cases}$$

or

$$d_\pm(E) = \mathcal{N}\frac{2}{\Gamma\sqrt{2\pi}} \exp\left(-\frac{2(E \pm \Delta/2)^2}{\Gamma^2}\right). \tag{4.7}$$

Again, at integer filling factor, the chemical potential remains at the centre of the energy gap. Fig. 4.4 shows a numerical calculation of the diagonal conductivity for the Gaussian density of states, where the gap between the peaks in the density of states (Δ) has been taken to be 5 K, for three different disorder widths $\Gamma = 0.5, 1$ and 1.5 K. At the lowest temperatures, the disorder causes a flattening off of the data. The slope of the linear portion of each graph corresponds to an apparent energy gap of $\Delta = \Delta - \Gamma$: this demonstrates the important result that the Arrhenius method gives an energy gap affected by disorder. A alternative technique for the direct determination of the energy gaps between peaks in the density of states is that of Lifshitz and Kosevich [111]; it was not utilized in this work because the exchange effects under investigation are quenched at the high temperatures used in this method.

At the lowest temperatures, the conductivity drops to very small values; the transport is thought to be dominated by hopping [112, 113] in the localized

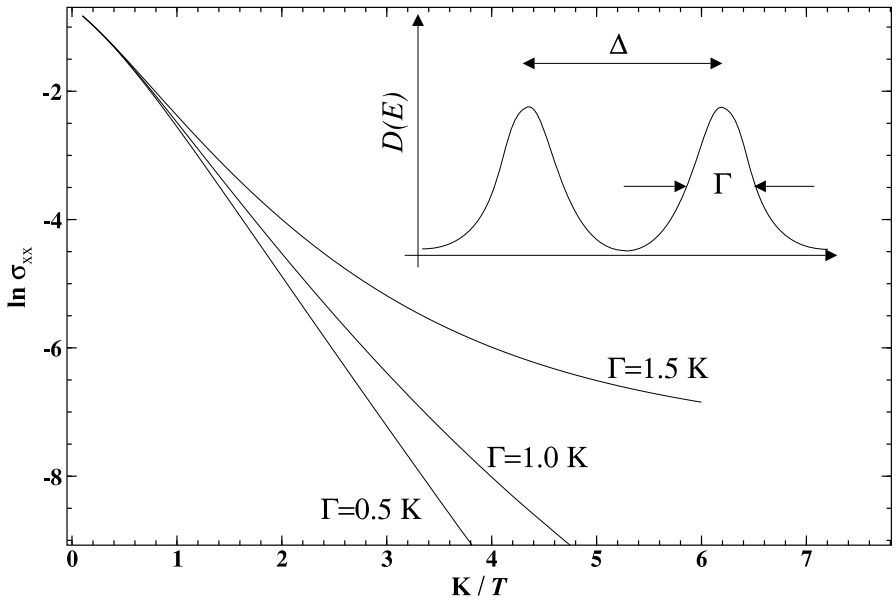

Figure 4.4: Numerically calculated examples of an activation plot, displaying non-linear behaviour, due to the Fermionic nature of the quasiparticles at high T and disorder broadening of the Landau level density of states at low T. The solid line represents $\ln \sigma_{xx}$ calculated with a Gaussian density of states. Δ is 5 K, and Γ takes the values 0.5,1.0, and 1.5 K.

tails of the density of states, rather than by the excitation of carriers into the delocalized states near to the centre of the Landau level. The activation plots then show strong non-linearity at high values of $1/T$, as σ_{xx} exceeds the value expected from normal activation. Again, the data would be expected to flatten off. Thus, the effect would look similar to the non-linearity due to large Landau level width although its origin is clearly different. Useful discussions of these effects may be found in references [100] and [107].

Temperature-dependent energy gaps From Section 3.3, the gap to single-particle excitations at, for example, $\nu = 5$ may be written as

$$\Delta_5 = S + A_{22}(\rho_2^+ - \rho_2^-), \tag{4.8}$$

where S represents a single-particle 'spin' gap such as $g\mu_B B$, A_{22} is the intra-Landau-level exchange energy per particle, the $+$ and $-$ represent the spin of the Landau level, and ρ its fractional occupation. At low temperatures, the gap takes the value $S + A_{22}$ but at high temperatures it is simply S since $\rho^+ \approx \rho^-$. The transitionary behaviour between the two regimes may

be determined by solving equation 4.8 for Δ (ρ is a function of Δ also). The

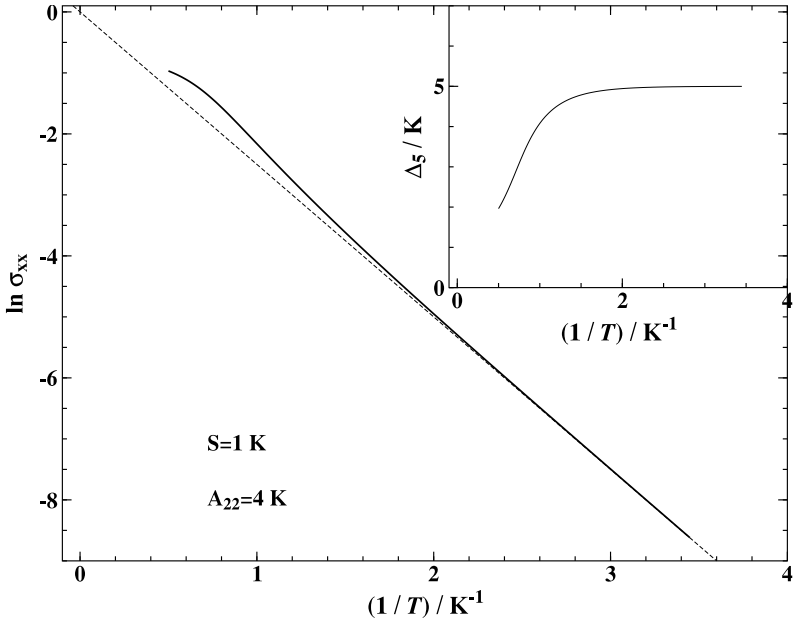

Figure 4.5: Calculated activation plot for an exchange enhanced gap. The dashed line shows the linear portion of the data.

results of such a calculation, for $S = 1$ and $A_{22} = 4$ are plotted as an activation plot in Fig. 4.5, with the inset showing the solution Δ versus $1/T$. The Landau levels were assumed to have a delta function density of states. The deviation from straight-line behaviour at high temperature occurs as the energy gap drops. The values of S and A_{22} were chosen to provide a stringent check of possible errors in the activation plot analysis. The calculation shows that for the temperatures over which the experimental data were fitted, there are no systematic effects due to the quenching of a possible exchange energy. None of the experimental traces was found to exhibit an up-turn at low $1/T$. This observation is not interpreted as evidence against the presence of sizeable exchange contributions to the energy gaps, because it is possible that the effect is masked by the drop in mobility at high temperatures.

4.4 Data for $\nu = 6$

In a sample for which $g\mu_B B < \hbar\omega_C$, the energy gaps at even filling factor decrease and the energy gaps at odd filling factor increase simultaneously (see Fig. 4.1), as the tilt angle is increased.

At sufficiently low temperature, the energy gap leads to an apparent zero in the diagonal resistivity ρ_{xx} which occurs because the chemical potential lies in the localized states in the disorder tails of the density of states. As the gap gets smaller, due to the tilting, the minimum value should lift off zero in an activated fashion. The oscillation should disappear entirely when the Landau levels cross. This is root of the 'coincidence' techniques used for the deduction of the g factor [99].

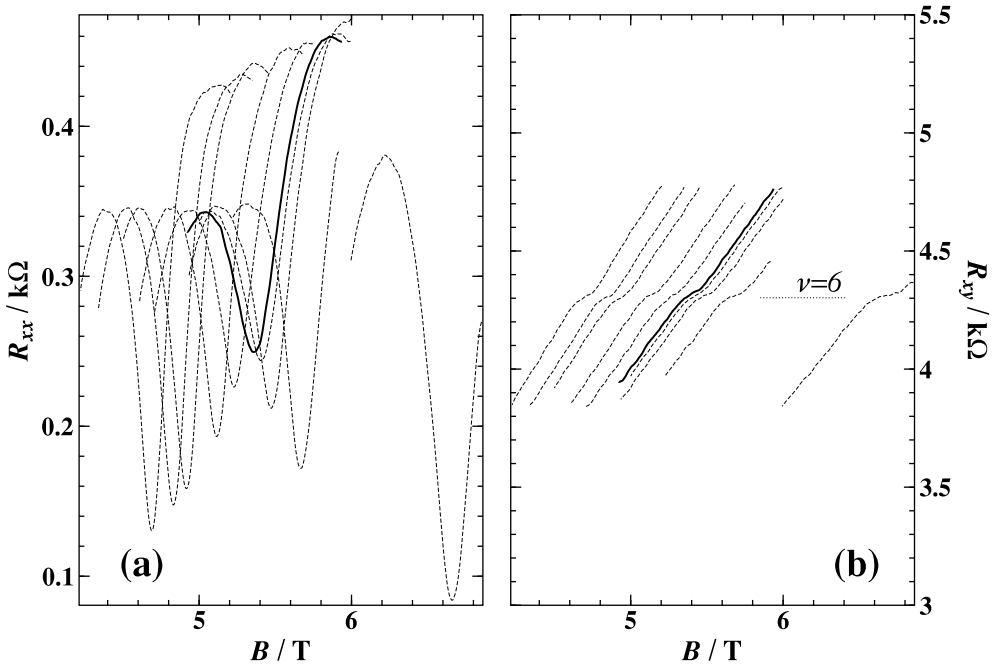

Figure 4.6: (a) The $\nu = 6$ oscillation in R_{xx} as a function of the total magnetic field B, for increasing tilt angles. The visibility of the oscillation decreases for fields up to 5.25 T (solid line), and then increases. (b) Measurements of ρ_{xy} indicate that the quantum Hall state survives over this range of angles. The angles vary between $\theta = 74°$ and $\theta = 79°$.

The data presented in Fig. 4.6(a) show the oscillation at 280 mK for $\nu = 6$ in a chip of wafer T240. The resistance of the oscillation minimum increases as the feature becomes less visible. This corresponds to the approach of a pair of Landau levels as B increases. However, there remains a clear oscillation for all angles displayed because for $B > 5.25$ T the trend is reversed, and the oscillation increases in visibility. Hence for $B > 5.25$ T the gap appears to increase despite never having reached zero. It remains possible that, with a finer grid of angles, a crossing point could have been found. In fact, an extra

four such angles on either side of the thick line in Fig. 4.6 were examined, but were omitted for clarity. They did not indicate a sudden collapse of the energy gap. For all of these angles, there remains a quantized plateau (to accuracy $\pm 3\%$) in the Hall resistivity ρ_{xy} (Fig. 4.6(b)).

The physics behind the failure of these Landau levels to cross is in principle very complex, not least because of the complexities of the valence band in III-V semiconductors. The possible processes involved are presented in Chapters 5 and 3, and include Landau level anticrossing and an exchange-driven phase transition. Important information is contained in the variation of the energy gap with magnetic field. However, the energy gaps at this filling factor are small compared with the measurement temperature and are therefore difficult to measure by the activation technique.

Similar behaviour was also observed at $\nu = 8$, although the minimum value of the energy gap was even smaller than for the $\nu = 6$ case. In the remainder of this thesis, the technique described above for determining the turning point of the energy gaps will be referred to as the 'visibility' method.

4.5 Behaviour at $\nu = 4$

Filling factor $\nu = 4$ is more convenient to study over the available temperature range. Because it occurs at higher perpendicular magnetic field, the energy gaps are suitable for measurement using the activation method. The visibility of the $\nu = 4$ oscillation exhibited a minimum turning point at (9.10 ± 0.06) T, which corresponds to a tilt angle of $\theta = (78.0 \pm 0.1)^\circ$. Activation data, which were obtained over 5.5 squares in this case, were converted from ρ_{xx} to σ_{xx} using relation 4.3. A sample of the data is plotted as $\ln \sigma_{xx}$ versus $1/T$ in Fig. 4.7(a) for a variety of angles up to the turning point.

The data have been linearly fitted over the range $-18.3 < \sigma_{xx} < -15.3$; the lower limit is set by the lowest measurable resistance (which is taken to be 2.5 Ω) whilst the higher one corresponds to the resistance at which some of the activation plots start to show curvature.

It is clear that the energy gaps, Δ_4, decrease as the tilt angle increases. The most steep plot corresponds to a total energy gap of (9.0 ± 0.1) K; the plot with the lowest gradient gives $\Delta_4 = (3.7 \pm 0.1)$ K. These errors represent the random error associated with the extraction of the energy gaps from the activation plots; the absolute values of Δ_ν are also subject to systematic errors, which are discussed later. The intersection of all of the straight lines with the y axis occurs at approximately the same value: $\ln \sigma_0 = (-9.0 \pm 0.1)$. This fact is also commented on in the forthcoming errors discussion.

Data obtained at magnetic fields higher than 9.10 T are plotted in Fig. 4.7(b),

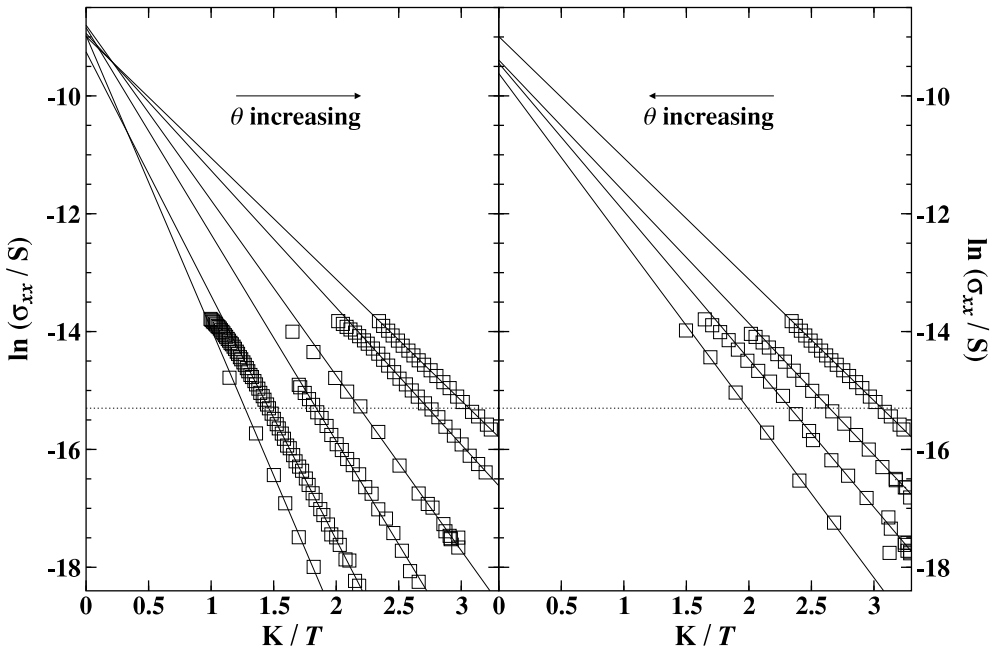

Figure 4.7: (a) Plots of $\ln \sigma_{xx}$ versus $1/T$ at $\nu = 4$ in a sample of T240, for a variety of tilt angles. The most steep line corresponds to perpendicular orientation of the sample. As the θ increases, the gradients (and energy gaps) decrease. The lowest-gradient line occurs at 9.10 T, (78.0°) and is a turning point. (b) As θ increases further, the energy gaps rise.

with *increasing gradients* as the tilt angle increases. An important difference is that the y-intercept is systematically lower than before the turning point: it is found to be $\ln \sigma_0 = (-9.5 \pm 0.1)$. The importance of the actual value of the intercept has been the subject of some discussion, especially in the fractional quantum Hall effect regime in both electron and hole systems [114, 100, 107].

A sample from wafer T335n+, which has a lower carrier density of $(1.3 \pm 0.02) \times 10^{15}$ m^{-2}, was also studied; the data for $\nu = 4$ are presented in Fig. 4.8. The turning point was located at (11.4±0.1) T, $\theta = (83.1 \pm 0.2)°$, as determined using the 'visibility' technique. The energy gap there was too small to be measured using the activation technique.

4.5.1 Energy Gaps

The energy gaps determined from the activation data are plotted in Fig. 4.9, for samples T240 and T335n+. Included in the T335n+ data is a dotted line at 11.4 T which indicates the turning point of the graph, as determined from

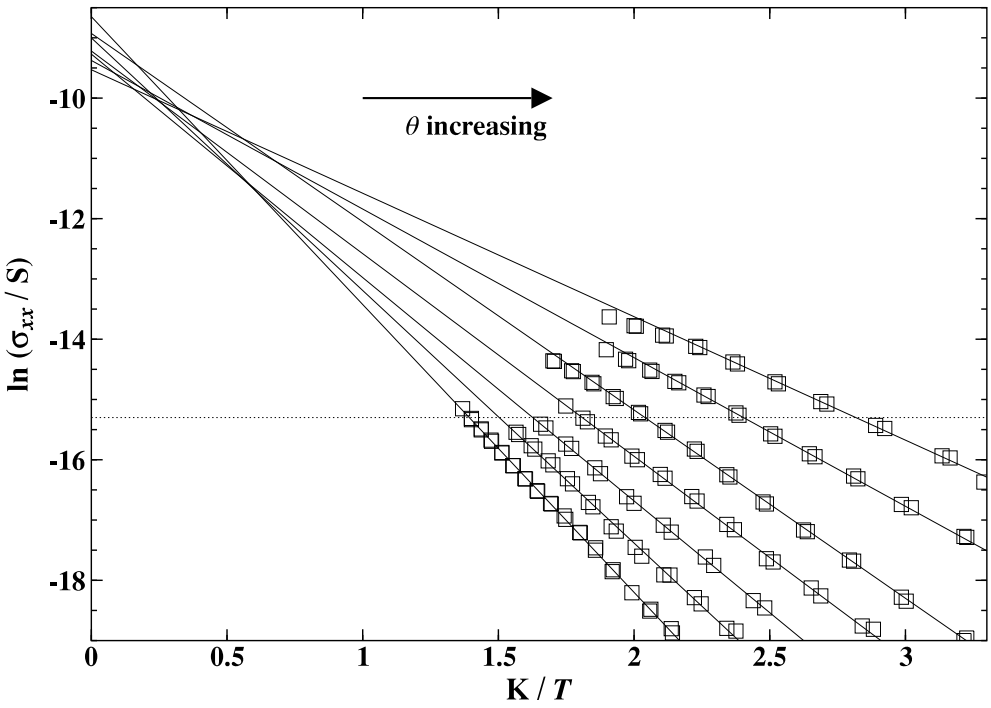

Figure 4.8: Activation plots for sample T335n+. The gradients of the best-fit lines decreases as the tilt angle increases.

visibility data obtained at base temperature. At $\nu = 4$, both samples exhibit turning points at non-zero energy gaps and the dependence up to the turning point is close to linear. In fact, the curvature appears to be slightly negative in both cases. In the picture of simple, electron-like Landau levels presented in Fig. 4.1, no curvature is expected because the levels have been assumed not to interact as they approach. The possibility that the Landau levels anticross, which might be expected from a model incorporating the full complexities of the valence band, should introduce some positive curvature in the vicinity of the turning point. However, this is not observed and the turning point remains sharp. The possibility that this is a systematic error is discussed below; other possibilities are discussed in detail in Chapter 5.

Examination of Fig. 4.2 indicates that the temperature error is a function of both T and B. In the course of the experiment, the data were taken at different magnetic fields and over different temperature ranges. The possibility that systematic error has masked curvature in the diagram must therefore be addressed.

The most important point to be made is that the activation plots were close

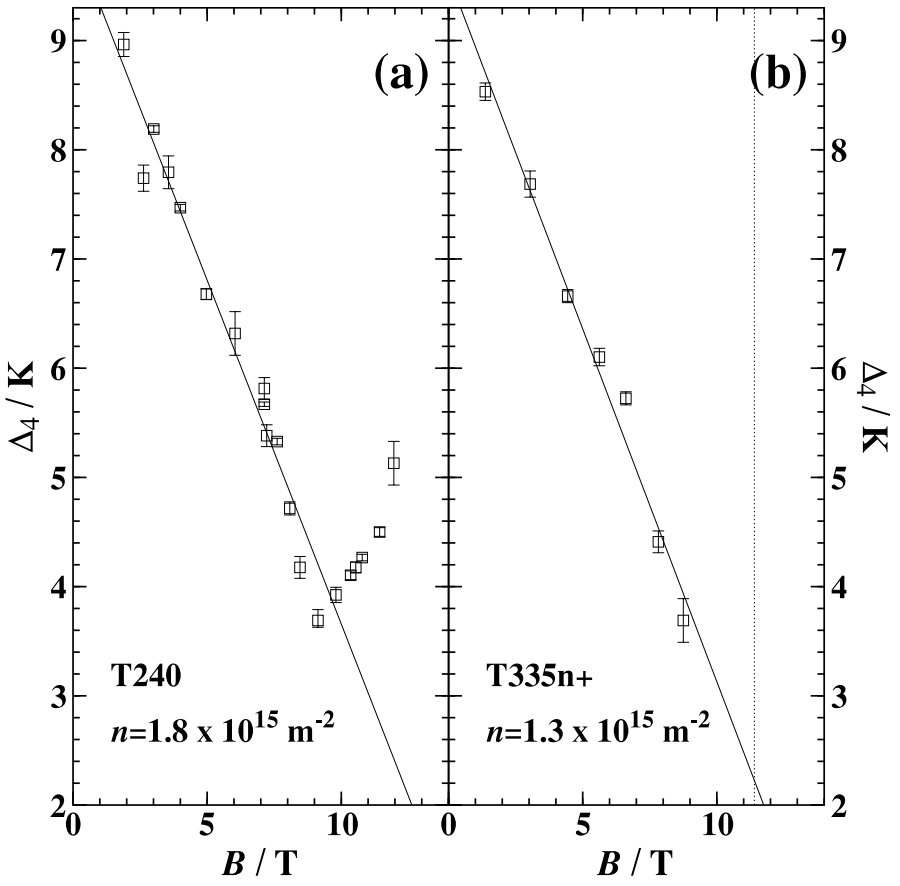

Figure 4.9: Energy gaps measured at $\nu = 4$ for sample: (a) T240; (b) T335n+. The dotted line indicates the turning point of the T335n+ data. Random error bars determined from the fits are included; the size of the error bars reflects the number of points fitted. It should be noted, however, that the primary source of error is systematic.

to linear. The fact that the straight-line fits shared a common intercept (see Section 4.5) indicates that each data set was fitted over its simply-activated range (and not in the high T regime in which the activation plots flatten off).

The ranges of temperature over which the activation plots were fitted are indicated by the double-headed arrows in Fig. 4.2. An estimate of the variation in error may be obtained by choosing the error at the centres of the arrows. This gives a suggested temperature error that varies between -1% and -5% at the turning point. The sign of the error means that the measured temperature was too high. This leads to a small (≈ 0.2 K) *over estimation* of the energy

gaps in the vicinity of the turning point plotted in Fig. 4.9. Therefore the slight negative curvature cannot be explained by thermometry errors.

It remains to discuss the possible effects of disorder. The experimental data presented in Figs. 4.7 and 4.8 do not exhibit the strong saturation at low temperature that is a signature of significant disorder (see Fig. 4.4). This suggests that the full-width of the energy broadening of transport density of states is less than 1 K (see Fig. 4.4). It proved to be impossible in numerical simulations to reproduce, with this disorder width, the negative curvature observed in the experimental data.

4.5.2 Dependence on orientation

Investigation showed that the relative orientations of the current direction, the in-plane component of B and the $[01\overline{1}]$ and $[\overline{2}33]$ axes of the crystal made no significant difference to the results. It was found, in samples of both T240 and T335n+, that the non-zero minimum energy gaps, the magnetic fields at which the minima occurred, and the gradients of the gaps as a function of B, did not depend on either the orientation of the current with respect to the axis of tilt or the crystal axes. This demonstrates the generality of the observations; the detailed experiments on T335n+ and T240 which are presented here were restricted to $B_{||}$ parallel to I. However, in T335n+ I was aligned in the $[\overline{2}33]$ direction whereas in T240 it was aligned to $[01\overline{1}]$.

4.6 Energy gaps at odd filling factors

The variation in energy gap at odd filling factors was also studied, using the same techniques. As expected, the variation of the resistance of the $\nu = 7, 5, 3$ oscillation minima showed that Δ_5 and Δ_3 increased at low tilt angles. The data for Δ_5 exhibited a turning point, but the $\nu = 3$ data did not.

The energy gap data presented in Fig. 4.10 were obtained using activation techniques for sample T240. It was not possible to measure Δ_5 for sample T335n+ using the activation technique because the energy gaps were not sufficiently large. The Δ_5 versus B relationship exhibits a turning point at 5.75 T. In contrast to the behaviour at $\nu = 4$, there appears to be curvature in the vicinity of the turning point. Again, this observation is independent of the estimated systematic errors in the measurement. At $\nu = 3$, there is again clear curvature; however, in the available field range it is not possible to identify a turning point. Away from the 5.75 T, the Δ_5 data are consistent with the straight lines imposed on the data points. The gradients of these lines have been chosen to be the same as the gradients fitted to the $\nu = 4$ data.

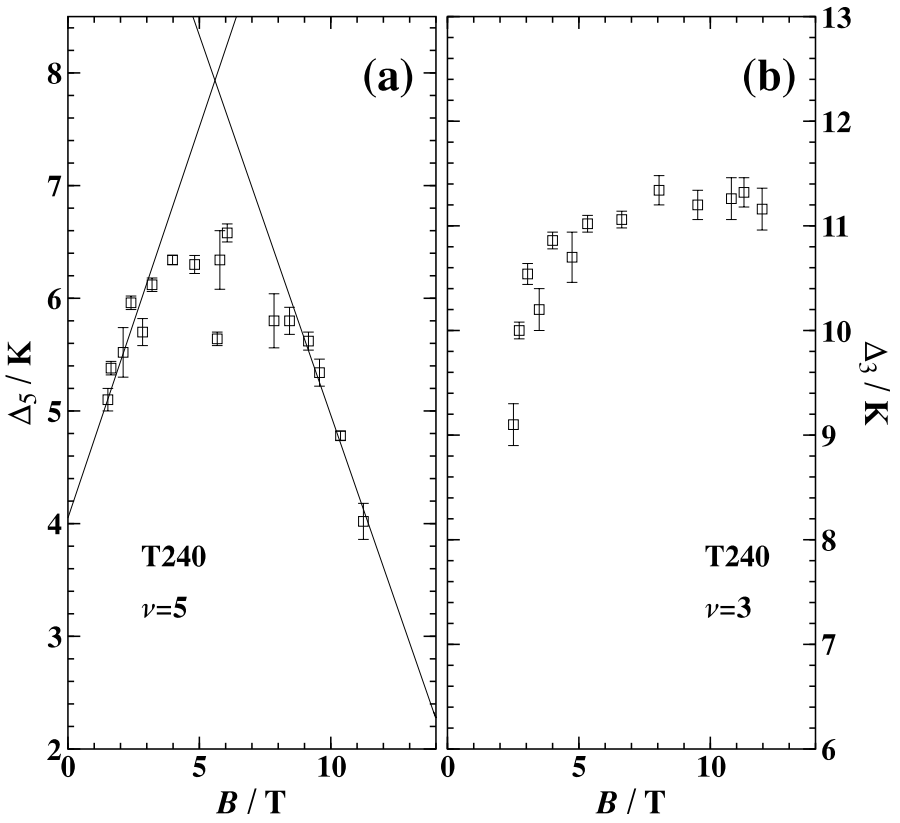

Figure 4.10: Energy gaps measured at (a) $\nu = 5$ and (b) $\nu = 3$ for sample T240.

4.7 Summary

This chapter has presented the results of tilted-field experiments performed on two-dimensional hole systems confined to 200 Å symmetric quantum wells. The measurements have been performed using the activation-energy technique to determine the energy gaps at fixed even and odd filling factors. The assumptions of the techniques and the consequences of relaxing them have been examined in some detail. Systematic errors due to thermometry in a magnetic field have also been discussed.

At low angles it has been found that Δ_i increases for odd i, and decreases for even i. Eventually, the even and odd gaps exhibit turning points at sufficiently high tilt angles. This is expected in a simple non-interacting picture, outlined previously, in which Landau levels cross when the cyclotron energy equals the Zeeman energy. However, two observations indicate that the physics requires a more complicated description: (i) the turning points at even filling

factors occur at non-zero energy gaps; (ii) Δ_4 is a linear function of B up to its minimum value. Also, the variation of Δ_5 is not well described by the simple electron-like description of the Landau levels, depicted in Fig. 4.1. These observations are addressed in Chapter 5, which contains a discussion of the data incorporating both the complexities of the valence band and also the role of interactions between the holes.

Chapter 5

Tilted magnetic field studies: discussion

5.1 Introduction

Tilted-field measurements presented in Chapter 4 showed that at $\nu = 4$, the energy gap to single-particle excitations decreased, and then increased with its turning point at non-zero gap. Explanations of this and other observations are considered here, in the context of Landau level coupling due to the low symmetry of the system, exchange interactions in the 2DHS and the possibility that the exchange interactions cause a phase transition between an unpolarized and a polarized ground state at even filling factors.

5.2 Properties of hole Landau levels

5.2.1 g factors of electron systems

The g factor of the electron, g_e, which describes the energy of interaction of its spin magnetic moment with a magnetic field, is renormalized by interactions with the crystal structure. It turns out that it remains isotropic in 3D GaAs, with $g_e = (-0.44 \pm 0.005)$ [4]. In a heterostructure, the electron g factor is altered again because the bulk g factor of the electron in AlGaAs has the opposite sign to that of GaAs, and the net g factor is determined in part by the penetration of the electron wavefunction into the barriers. In wide wells, this is small and a typical value is $g_e = -0.40$ for a 200 Å quantum well. For narrow wells, the electron spends a large proportion of its time in the barrier; therefore g_e is positive. The cross-over from negative to positive electronic g factor occurs at symmetric well widths of approximately 50 Å[115] (for barriers of $Al_{1-x}Ga_xAs$ with $x = 0.36$).

5.2.2 g factors of the 2DHS

The Zeeman-like coupling of a magnetic field to the magnetic moment of the hole (which contains orbital contributions) in 3D GaAs is usually written as $\sum_{\alpha=x,y,z} 2\mu_B(\kappa B_\alpha J_\alpha + q_L B_\alpha J_\alpha^3)$ [46]. The Luttinger parameter κ for GaAs is 1.2 ± 0.05 [4]. The confinement of the holes to two dimensions splits the LH-HH degeneracy at $k_{||} = 0$, and the lowest energy 2D subband is HH1. At $k_{||} = 0$, the light and heavy holes are completely decoupled for (100) and (111) planes, and close to decoupled for lower symmetry planes such as (311) (see Section 2.3).

The effect of a *non-quantizing* magnetic field on the two-fold degenerate HH1 states at $k_{||} = 0$ may be investigated using degenerate first-order perturbation theory. Labelling the two degenerate states as $|a\rangle$ and $|b\rangle$, the energy corrections to the states by a perturbation $H' = B_i J_i$ (where i represents x, y, z) are given by the solutions of:

$$\begin{vmatrix} H'_{aa} - \epsilon & H'_{ab} \\ H'_{ba} & H'_{bb} - \epsilon \end{vmatrix} = 0, \tag{5.1}$$

where $H'_{ab} = B_i \langle a|J_i|b\rangle$, etc. [20]. The kets $|a\rangle = |3/2, +3/2\rangle$ and $|b\rangle = |3/2, -3/2\rangle$ have been labelled according to their angular momentum components in the z direction. It is noted here that the angular momentum operators do not truly commute with the real Hamiltonian (see Chapter 2).

If $i = z$ the off-diagonal elements of equation 5.1 vanish but the diagonal ones do not. Two distinct energy corrections are found and 'spin splitting' is predicted. On the other hand, if $i = x$ or y then all of the elements vanish and to first order the two-fold degeneracy is not lifted.

Thus, the HH g factor is zero for fields applied parallel to the plane of confinement, but non-zero for fields applied perpendicular to it. This anisotropy is a direct consequence of the energy separation of the light and heavy holes; these mix as $k_{||}$ increases from zero and the 2D parallel HH g factor, $g_{||}$, increases.

As for the electron g factor, the perpendicular HH g factor, $g_\perp$, varies strongly with quantum-well width. It has been measured indirectly from excitonic g factors to be positive for large well widths, with a value of approximately $g_\perp = 1.0 \pm 0.1$ for a well of width 200 Å. It decreases as the width decreases, and passes through zero at 80 Å [115]. $g_{||}$ has been measured to be very close to zero using optically detected magneto-resonance in type II GaAs/AlAs superlattices [61]. The measurements of g factors in this thesis determine only their magnitude and not their sign.

5.2.3 Tilted fields and hole g factors

Martin *et al.* [106] showed that the spin splitting of the Landau levels of very strongly confined 2DHSs is caused by $B_\perp$ only (not the total magnetic field as in an electron system), thus explaining the earlier tilted-field observations of Iye *et al.* [105]. The authors of reference [106] provided explicit expressions for the Zeeman energies of pure HH and pure LH Landau levels in arbitrarily oriented magnetic fields:

$$\begin{array}{rcll} E_Z & = & 6\kappa\mu_B B_\perp & \text{HH} \\ E_Z & = & 2\kappa\mu_B\sqrt{B_\perp^2 + 4B_{||}^2} & \text{LH.} \end{array} \tag{5.2}$$

These expressions can also be obtained from equation 5.1; the HH result means that $g_{||} = 0$. The decoupling of the LH and HH Landau levels occurs when the separation of the 2D subbands is very large, and is therefore relevant to very narrow wells and also material systems subject to strong uniaxial strain such as SiGe. Indeed, measurements in Si/SiGe heterostructures have been reported to show little or no variation of quantum Hall effect energy gaps with B for $B_\perp$ fixed, because the parallel HH g factor in those systems is very small [116, 90, 97]. Martin *et al.* also provide diamagnetic corrections to the energies of the Landau levels, some of which affect the $|+3/2\rangle$ and $|-3/2\rangle$ states differently.

The case of intermediate mixing between the HH and LH states, which might be expected in typical GaAs/AlGaAs samples, has not been studied extensively. Calculations of the band structure of the 2DHS in a tilted magnetic field have been published by Heuring *et al.* [117, 109], in work that also presented some crude experimental results. A tilted-field measurement of the anisotropy of the HH g factor was published by Dorozhkin [118], for the Si-MOSFET system. The theoretical analysis was similar to that given above for the zero-field case.

5.2.4 Justification for the tilted-field analysis

In the absence of an intuitive or complete theory of hole Landau levels in a tilted magnetic field, the data are interpreted in this thesis using the approach described in this section. Figure 5.1(a) shows schematically the E versus $B_\perp$ relation for the valence band. The Landau levels exhibit some non-linearity due to mixing effects. The levels have been labelled in accordance with the discussion in Section 2.4 of Chapter 2, and are marked with $+$ or $-$ to show the dominant spinor component of the envelope function. As can be seen, at low magnetic fields the Landau levels form an alternating ladder of $+$ and $-$ states.

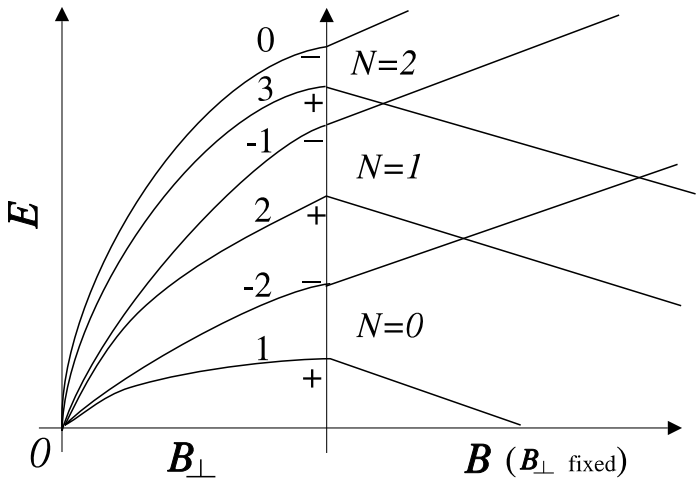

Figure 5.1: (a) The hole Landau level dispersion in a perpendicular magnetic field. The integers (m) are described in Section 2.4. (b) Tilting the sample, keeping $B_\perp$ constant. The labels N denote the harmonic oscillator labels of the Landau levels.

The tilted field experiment begins at zero angle of tilt. As $B_\perp$ is increased from zero to that of the required filling factor, the valence-band Landau-level structure evolves as depicted in Figs. 2.3 and 5.1(a). It is not well described by any single effective mass or perpendicular g factor. The angular momentum component of each Landau level is a certain mixture of the $|J, M_J\rangle$ states, and in principle depends strongly on $B_\perp$; it is therefore different for each filling factor.

The experiment proceeds by tilting the field, for fixed $B_\perp$, thereby introducing a parallel component $B_{||}$. To a first approximation, the effect of increasing B can be estimated using the perturbative approach outlined in Section 5.2.2. The Landau levels undergo changes in energy according to their zeroth-order spin mixtures, which are determined by $B_\perp$. If the particular Landau level has no LH components, then it is unaffected by $B_{||}$; this 'decoupled' limit is approached in a SiGe 2DHS. If the level has a small LH component then its energy varies according to a strongly anisotropic 2D g factor; the other limit is that of strong mixing, in which case $g_{||} \approx g_\perp$ and the g factor is roughly isotropic.

As $B_{||}$ increases further, the particular admixture of LH and HH states forming the Landau levels should change. This should alter the g factors of the levels. It is argued in the next section that such mixing does not appear to occur, or that it does not affect the g factors of the Landau levels.

5.2.5 Anisotropy of the g factor

Figure 5.2 reproduces Fig. 4.9, and shows the Δ_4 data obtained from samples T240 and T335n+, over a range of tilt angles. The horizontal axis is the *total* magnetic field B. The variation of Δ_4 appears to be a linear function of B, which implies that the 2D HH g factor is isotropic (i.e. electron-like) with $g_{||} = g_{\perp} = g$. Values for g of 0.95 ± 0.05 appear to fit both T240 and T335n+ rather well (straight lines in Fig. 5.2), although beyond 7 T, both sets of data systematically fall below the line. The linearity of the Δ_4 dependences implies

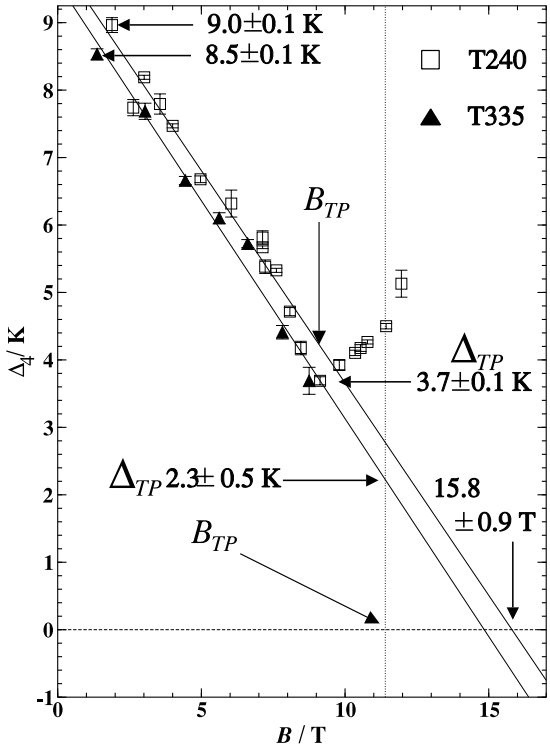

Figure 5.2: Reproduction of data obtained from T240 (empty squares) and T335n+ (solid triangles) for $\nu = 4$, including energy gaps (in K) to be used in later sections.

that the angular momentum admixtures of the Landau levels in the vicinity of the chemical potential are not changed significantly by the introduction of a strong $B_{||}$ component.

Given then that the properties of the Landau levels are mainly determined by $B_{\perp}$, it is valid to investigate the anisotropy of their g factors. An expression for the total Zeeman energy E_Z of a 2DHS with mixed LH and HH character

is not available; a pragmatic approach is to use the expression

$$E_Z = \mu_B \sqrt{g_\perp^2 B_\perp^2 + g_{||}^2 B_{||}^2}, \tag{5.3}$$

which has been applied in the analysis of tilted field measurements of a 2DHS before [119]. Comparison with equations 5.2 (which do not apply in the case of mixed hole character) shows that it is certain to be a simplification.

The data presented in Fig. 5.2 may be fitted to the form $C - E_Z$ where C is equivalent to a cyclotron splitting. It is found that fitting with three free parameters produces relatively good fits for a range of fitting parameters. The results for the g factors at $\nu = 4$ for the two samples investigated are summarized in table 5.2.5. Linear and anisotropic fits were performed for data points in the ranges $B < 9.1$ T and $B < 8.1$ T. The table shows that

Fit	C / K	$g_{\|\|}$	$g_\perp$
T240 Linear ($B < 9.1$ T)	10.3 ± 0.2	1.0 ± 0.05	1.0 ± 0.05
T240 Linear ($B < 8.1$ T)	10.1 ± 0.2	0.95 ± 0.05	0.95 ± 0.05
T240 Anis. ($B < 9.1$ T)	11.8 ± 2.0	1.1 ± 0.10	1.51 ± 0.6
T240 Anis. ($B < 8.1$ T)	9.8 ± 0.4	0.9 ± 0.07	0.63 ± 0.25
T335n+ Linear ($B < 9.1$ T)	9.6 ± 0.2	0.98 ± 0.05	0.98 ± 0.05
T335n+ Linear ($B < 8.1$ T)	9.4 ± 0.2	0.88 ± 0.05	0.88 ± 0.05
T335n+ Anis. ($B < 9.1$ T)	10.6 ± 0.6	1.1 ± 0.08	2.3 ± 0.75
T335n+ Anis. ($B < 8.1$ T)	9.6 ± 1.0	0.94 ± 0.07	1.21 ± 0.5

Table 5.1: Anisotropic g factors measured at $\nu = 4$ for samples T240 and T335n+.

when all the data points up to the turning point are included in the anisotropic fits, $g_\perp > g_{||}$. The particular values for $g_\perp$ are subject to a relatively large error because of the insensitivity of the fitting function in the regime $B_{||} > B_\perp$. Also, the values for $g_\perp$ exceed those quoted in the literature [115]; this could be because our experiment probes different Landau levels to optical experiments. However, the fits to the data points at fields less than 8.1 T reduce the apparent anisotropy.

Because of the large values for $g_{||}$, the possible g factor anisotropy is small and cannot be determined clearly by this experiment. For the remainder of this chapter, the 2D HH g factor will be assumed to be isotropic with $g = 0.95 \pm 0.05$, except during error considerations.

Fig. 5.4 reproduces data for Δ_5 versus B first presented in Fig. 4.10. It is difficult to define a slope for Δ_5, because of the apparent curvature of the data. However, lines of slope $\pm 0.95 \mu_B$ imposed on the data in Fig. 5.4 are also consistent with it, and strengthen our assumption of an isotropic g factor.

5.3 Anticrossing of Landau levels

In a purely perpendicular magnetic field, anticrossing is predicted to occur between hole Landau levels with index m differing by both 4 and 3, when the axial approximation is dropped (see Section 2.4). The introduction of an in-plane magnetic field removes the axial symmetry altogether; extra couplings are to be expected even when the crystal Hamiltonian is approximated to be axially symmetric. In this section, the possibility that such anticrossings can explain the data is examined.

Arguments are presented which show that some, but not all, of the features of the Δ_4 and Δ_5 may be explained using anticrossing ideas. The observations of non-vanishing quantum Hall effect states as a function of tilt angle, at $\nu = 6$ (Fig. 4.6) and $\nu = 8$, are probably such anticrossing effects.

5.3.1 Previous work

There exists in the literature a number of papers describing optical measurements of the valence band in a strong *perpendicular* magnetic field. Hirakawa *et al.* [120], who present cyclotron resonance data, argue that anomalies in the line splitting indicate the crossing or anticrossing of Landau levels originating from the zero-field HH1 and LH1 subbands (see also reference [121]).

This interpretation is strengthened by a subsequent paper [122], which presents a rather complete experimental study of the cyclotron resonance in the single-interface (i.e. very asymmetric) (311)-oriented 2DHS. It provides clear evidence of the anticrossing between Landau levels originating from different 2D subbands (in the axial approximation, this crossing is allowed). The size of the minimum energy gap is found to vary linearly with carrier density.

The cyclotron resonance measurements of Cole *et al.* [62] indicate more directly the crossing between the two lowest HH Landau levels (indices 1 and -2) as a function of $B_\perp$. They argue that for (311) samples, this becomes an anticrossing when the axial approximation is relaxed. However, they were unable to distinguish clearly the extent of mixing because the sample temperature was rather high compared with the energy gap.

These optical measurements were performed for $B_\perp > 6$ T, mostly corresponding to $\nu < 1$. In contrast, the measurements described in this thesis were performed for $B_\perp < 2$ T, and the observation of possible anticrossings was achieved by tilting the sample.

To the author's knowledge, there have been no measurements of the anticrossing of hole Landau levels in a tilted magnetic field in any two dimensional system. The only published calculations of the Landau level structure of the 2DHS in a tilted magnetic field are by Heuring *et al.* [117, 109]. They concern

an asymmetric single-interface heterostructure of rather high carrier density, and are compared with our experimental data in more detail in a later section.

5.3.2 Model

The expected behaviour of the energy gaps at even and odd filling factors is plotted in Fig. 5.3. The diagram has been constructed using the experimental fact that the turning point of the Δ_4 data, which occurs at $B_{TP} = (9.10 \pm 0.06)$ T in sample T240, has an energy $\Delta_{TP} = (3.7 \pm 0.1)$ K. Thus, the intersection of the $m = 3$ and $m = -1$ Landau levels of Fig. 5.1 has been replaced by an 'anticrossing' in Fig. 5.3.

In contrast to the electron case (Fig. 4.1), in which Δ_{odd} rises to a maximal point and then starts to fall immediately, the Δ_{odd} dependence is seen (Fig. 5.3(a)) to level off. This occurs at odd filling factors because of the irregular spacing of the Landau levels, which makes levels below the chemical potential cross at a different B to the levels above the chemical potential. In the regime between these two crossings, the energy gap remains constant at a value that might be interpreted as a cyclotron gap.

The model fits approximately the data obtained at $\nu = 5$, plotted in Fig. 5.4, for sample T240. Thus the flattened portion of the Δ_5 dispersion may be interpreted not as an anticrossing of the approaching Landau levels but instead as a saturation of the gap because of the irregular spacing of the hole Landau levels. On the other hand, the curve traced by the Δ_5 does exhibit curvature at all magnetic fields; this is not accounted for by Fig. 5.3(a).

5.3.3 Quantitative Tests

For convenience, the notation used in this section is clarified here. The energy gap measured at the chemical potential, by an activation measurement, is defined to be Δ_ν where ν is an integer denoting the filling factor of the system. It is convenient to define $\Delta_{i,j}$ to be the energy gap between the hole Landau levels with indices $m = i$ and $m = j$. This energy gap can exist (in a non-interacting picture) for Landau levels below the chemical potential. In this section, it is assumed that the minimum energy gap of the Δ_4 versus B dependence, Δ_{TP}, is entirely due to an anticrossing of the Landau levels.

At $B_{||} = 0$, the energy gaps at integer filling factor have been measured using activation techniques to be $\Delta_4 = (9.0 \pm 0.1)$ K, $\Delta_5 = (5.1 \pm 0.1)$ K and $\Delta_6 = (4.2 \pm 0.1)$ K for T240. For T335n+, $\Delta_4 = (8.5 \pm 0.1)$ K, $\Delta_5 > (2.2 \pm 0.1)$ K and $\Delta_6 = (4.4 \pm 0.1)$ K.

These figures are *not* consistent with a single effective mass or value of

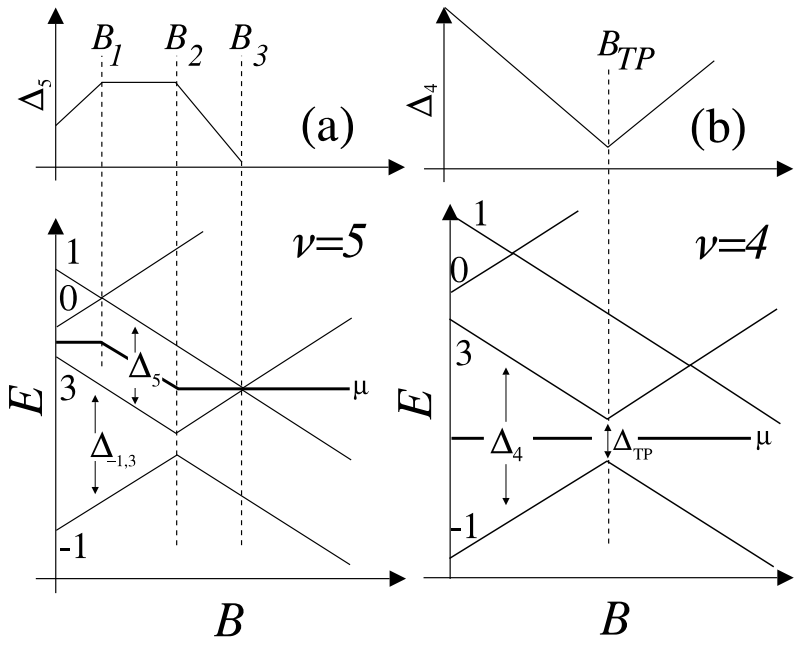

Figure 5.3: (a) Non-interacting Landau levels of a hole system, with energy gap at $\nu = 5$ inset. The chemical potential is shown as the thick line. The Landau levels with index $m = 3$ and $m = -1$ have been assumed to anticross. The indices are explained in section 2.4. (b) Same as (a) except at $\nu = 4$.

$g_\perp$. For example, the Δ_4 and Δ_6 of each wafer differ by factor of two despite the fact that $B_\perp$ increases by only a factor of 1.5 between the two filling factors. Furthermore, the values of these energy gaps are very similar in the two samples, despite the differing carrier densities. These observations are not surprising given the complexity of the hole Landau level structure as a function of $B_\perp$ (see Fig. 2.3 for $B_\perp < 2$ T).

We turn now to the tilted field behaviour. The magnetic field B_2 in Fig. 5.3, which is obtained from the Δ_5 data (Fig. 5.4), corresponds to the anticrossing of the occupied $m = 3$ and $m = -1$ Landau levels. These are the Landau levels which are probed directly at $\nu = 4$. B_2 has the value (8.2 ± 0.2) T. The energy gap between the $m = 3$ and $m = -1$ levels, $\Delta_{-1,3}$, changes by an amount $\tilde{\Delta}$ as the magnetic field varies from $B = B_2$ to $B = B_\perp$. $\tilde{\Delta}$ may be calculated to be a Zeeman energy $g\mu_B(B_2 - B_\perp) = (4.3 \pm 0.2)$ K.

It has been assumed that the $\Delta_{-1,3}$ versus B dependence is very similar to that of Δ_4 versus B, despite the fact that the former anticrossing occurs below the chemical potential but the latter occurs at the chemical potential. This assumption does not hold if inter-particle interactions are considered to

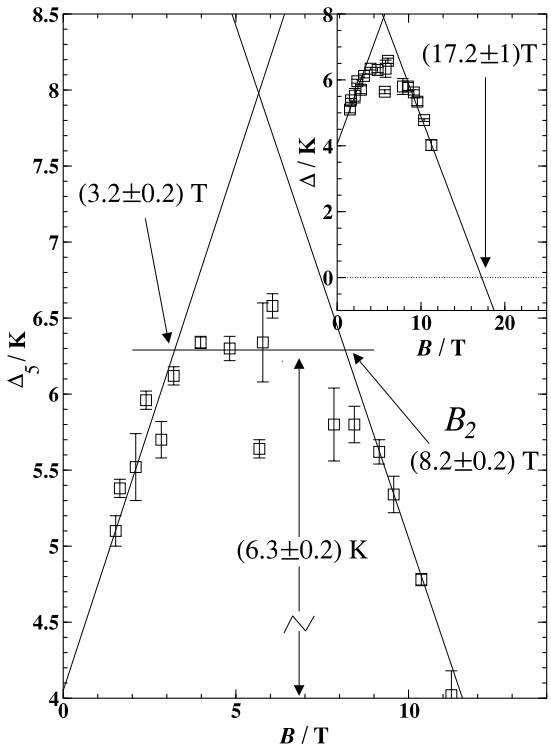

Figure 5.4: Data reproduced from Fig. 4.10, including various fitting lines discussed in the text. The extrapolation to $\Delta = 0$ is shown in the inset, and is rather dependent on the last two points.

be important, and is discussed in Section 5.4.

The actual value of $\Delta_{-1,3}$ at $B_{||} = 0$ may then be calculated to be the sum of $\tilde{\Delta}$ and the size of the anticrossing gap. Using the value of $\Delta_{TP} = (3.7 \pm 0.1)$ K, a total energy gap of $\Delta_{-1,3} = (8 \pm 0.3)$ K at $B_{||} = 0$ for $\nu = 5$ is obtained. This number is probably an overestimate, because Δ_{TP} is likely to be an increasing function of $B_\perp$.

From the Δ_4 data of Fig. 5.2, it is known that $\Delta_{-1,3}$ is (9.0 ± 0.1) K at $\nu = 4$, with $B_{||} = 0$, for an increase in $B_\perp$ of 25%. Furthermore, the anticrossing field increases from $B_2 = (8.2 \pm 0.2)$ T to $B_{TP} = (9.10 \pm 0.06)$ T. All of these numbers seem plausible, and the anticrossing theory (which is non-interacting) appears to account for the variation of the energy gaps and magnetic fields as $B_\perp$ increases from $\nu = 5$ to $\nu = 4$.

5.3.4 Comparison with Heuring *et al.* at $\nu = 4$

Figure 5.5(a) shows the energy difference between the Landau levels corresponding to $\nu = 4$, from a non-interacting calculation described in references [109] and [117], versus total magnetic field. The sample modelled in these calculations was a (100)-oriented single-interface 2DHS in the GaAs/AlGaAs material system, with a carrier concentration of approximately 2.4×10^{15} m^{-2}. $B_\perp$ was held constant at 5.2 T, which corresponded to $\nu = 2$.

The anticrossing observed is characterized by positive curvature in the vicinity of the turning point, and also by the different g factor after the levels have anticrossed. The energy gap at the turning point is approximately 2.8 K, which is similar to the experimental gap observed in samples T240 and T335n+ (Fig. 5.2). The sample considered in the calculation and those measured in this work differ significantly. The calculation's sample had higher carrier concentration, stronger confinement-potential asymmetry, and higher growth-plane symmetry. Nevertheless, the calculation shows that the order of magnitude of Δ_{TP} may be explained in the anticrossing picture. Furthermore, the differing gradients on either side of the turning point are also mirrored in the experimental data. The calculation does seem to capture some features of the data.

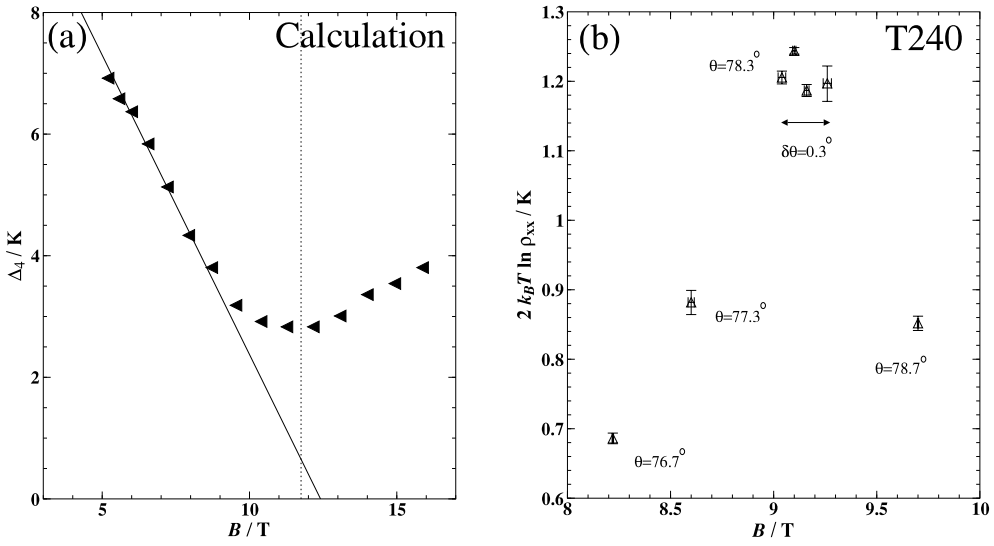

Figure 5.5: (a) The energy difference between the Landau levels on either side of the chemical potential at $\nu = 4$, extracted from the calculation of Heuring *et al.* The magnetic field of the turning point is marked by the vertical line. (b) Processed 'visibility' data showing the sharpness of the turning point in the T240 data: see text.

There are some important differences between the data and the calculation. Figure 5.2 shows that the experimental data exhibit slight *negative* curvature near to the turning point whereas the calculation shows rather clear positive curvature in that region.

Further evidence indicating the apparent sharpness of the turning point of the experimental data is presented in Fig. 5.5(b). Because Δ_4 for T240 was sufficiently large for all tilt angles, the resistance of the $\nu = 4$ oscillation minimum at base temperature remained rather low. This resistance should therefore have varied in an activated manner according to equation 4.2, which may be rearranged to give $\Delta = C - 2k_BT \ln \rho_{xx}$. Figure 5.5(b) plots the quantity $2k_BT \ln \rho_{xx}$ versus B in the vicinity of B_{TP}, for the T240 $\nu = 4$ oscillation minimum at (constant) base temperature. The data are of much higher resolution than those presented in Fig. 5.2; they show that the energy gap exhibits an abrupt turning point even in the highest resolution data obtained. This should be compared with the anticrossing of Fig. 5.5(a), which exhibits a very smoothly varying energy gap when examined at this resolution.

Another difference between the calculation of Heuring *et al.* and the data is apparent. The extrapolation of the low-field linear portion of the calculation to higher B (shown by the sloping line in Fig. 5.5) crosses the $\Delta = 0$ axis near to the turning point. In contrast, Fig. 5.2 shows that the extrapolations of the experimental points cross the axis at fields of approximately 16 T, which are significantly higher than the turning points of the data. This observation is independent of possible systematic errors which cause the underestimation of small energy gaps.

The differences between the extrapolations of the experimental data and the calculation of Heuring *et al.* may originate from the differences in the two sample specifications. However, the linearity of the Δ_4 versus B lines right up to their turning points (with some possible negative curvature) suggests that processes other than just mixing and anticrossing may be involved.

5.4 Spin-polarization instability?

5.4.1 Introduction

The magnetization of the 2DHS is determined by summing the individual angular momenta of the holes. It therefore depends on the 'spin' nature of the occupied Landau levels. The experimental data for $\nu = 4$ suggest that at $B = (9.10 \pm 0.06)$ T in T240, and $B = (11.4 \pm 0.1)$ T in T335n+, the uppermost Landau level is depopulated and replaced by one of different spin character. Thus, the magnetization of the 2DHS changes; if the spin assignments of the levels in Fig. 5.1 accurately describe the samples, then the system goes from

a paramagnetic phase (small magnetization) to a ferromagnetic phase (large magnetization) at the turning points.

This change of phase may occur continuously, by the mixing of the approaching Landau levels. This 'anticrossing' possibility has been discussed in Section 5.3; despite some successes it fails to account for the sharpness of the turning points observed in the experiment. Alternatively, the change of phase may occur abruptly. Such a first-order phase transition occurs because the interaction energy of the ferromagnetic phase is lower than that of the paramagnetic phase, and was discussed in detail for the case of electron-like fermions in Chapter 3. For convenience, some of the important points are repeated below.

Figures 4.1(a) and (b) (in Section 4.2.1) show the dependence of non-interacting electron-like Landau levels on the total magnetic field B for a system at constant even and odd filling factors respectively. At odd filling factors, the two Landau levels that approach each other are empty whereas at even filling factors one is unoccupied but the other is full. In the latter case, the system has the opportunity to lower its energy of interaction by promoting all of the particles in the highest occupied Landau level into the nearest unoccupied Landau level of opposite spin. This process dramatically lowers the Coulomb interaction energy of the system, by the exchange mechanism, because it increases the total number of particles of the same spin. The non-interacting energy cost of this transfer may be tuned using the Zeeman energy until it is outweighed by the reduction in the total interaction energy. The system then undergoes a first-order paramagnetic-ferromagnetic phase transition *before* the energy gap to single-particle excitations reaches zero.

5.4.2 Previous work

Although the theory of this phase transition is fairly well developed (see [80] and references therein), there has to date been no clear observation of the effect in any material system. One reason for this is that disorder, which has been shown to inhibit the transition [80], confines the search to small even filling factors. The low g factor and effective mass of electrons in an GaAs/AlGaAs heterostructure, which represent the cleanest experimental system currently available, require very large tilt angles (from perpendicular) and therefore prohibitively high magnetic fields. The high effective mass and g factor of holes in GaAs eliminate this problem whilst retaining a low level of disorder.

Electrons in the InGaAs/InP system have a particularly large g factor, which, in samples of reasonable carrier concentration, allows Landau levels to cross at accessible magnetic fields. Koch *et al.* [123] have observed that the $\nu = 2$ ρ_{xx} minimum does not disappear as a function of tilt, in samples

of sufficiently high mobility. This observation is similar to our observations at even filling factors in the 2DHS. Koch *et al.* argue that this indicates the occurrence of the phase transition. The authors state that they were unable to measure the energy gaps at the 'transition' point. An examination of their data at 200 mK and 500 mK (Fig. 4 of reference [123]) shows that ρ_{xx} increases by a factor of 2.5, corresponding to an energy gap of approximately 0.6 K. In the opinion of the author of this thesis, the gap is too small to be attributed (without further evidence) to exchange interactions; it could well be due to an ordinary anticrossing of the Landau levels of the system. The latter possibility was not discussed by Koch *et al.* They go on to show that usual crossings are observed in samples of lower mobility, and argue that there is a mobility threshold for the transition at 9.8 $m^2V^{-1}s^{-1}$. Obviously, very small anticrossing energy gaps would also cease to be observed in low mobility samples.

A more recent paper, by Coleridge *et al.*[90] also claims the observation of the phase transition in the SiGe material system. Measurements are presented which indicate that, as a function of perpendicular field, the Landau levels cross between $\nu = 2$ and $\nu = 3$, because of a large value of $g_\perp$. It is argued that anomalous features in the ρ_{xx} versus $B_\perp$ data are associated with the phase transition. This evidence is rather indirect, and no mechanism explaining the anomalous features in terms of the transition is given.

For completeness, attention is drawn to the angle dependence of fractional quantum Hall effect states. In the 2DES, it is found that the energy gap at $\nu = 8/5$ decreases with increasing B, and then increases again before reaching zero [124]. It is argued that the turning point corresponds to a change in the polarization of the system. Measurements in the vicinity of $\nu = 3/2$ indicate the presence of composite fermions with spin [125], lending support to this idea. Measurements of the $\nu = 4/3$ state in the 2DHS show that it also has an energy-gap dependence on the tilt angle [30]; measurements performed in a perpendicular magnetic field as a function of carrier density show weakening of the depth of the minimum, followed by its complete disappearance and then re-emergence [126].

5.4.3 Assumptions of the theory

The Hartree-Fock theory of the exchange interaction, described in Chapter 3, is calculated in the extreme quantum limit. This means that the condition $\hbar\omega_C \gg e^2/4\pi\epsilon l_B$ holds. Because ω_C varies as $B_\perp$ and l_B as $1/\sqrt{B}$, this condition is met only at very high perpendicular magnetic fields.

Owing to the high effective mass, the extreme quantum limit cannot be reached in these hole systems for $\nu \geq 1$. In fact, the Coulomb energy of the

system appears to exceed its kinetic energy by a factor of seven even at $\nu = 1$ for T240, using the effective mass extracted from Fig. 2.2. One consequence of the large exchange energy is mixing of the Landau levels. This then allows effective screening at integer filling factor, which might be expected to reduce the exchange energy. In the literature, mixing has been invoked repeatedly as a cause of rather small observed exchange energies in *electron* systems, where discrepancies of a factor of about two or more are commonplace [99].

The assumption of zero thickness also needs to be relaxed. The non-zero width of the layer allows particles to avoid one another more effectively; the effect is to reduce further the exchange energies from their screened values. In order to estimate the reduction of the exchange interaction energy due to these effects, we compare the thickness of the wavefunction, which is about 200 Å, to the magnetic length at 1.9 T ($\nu = 4$ for T240), which is 190 Å. The separation of the particles increases from 190 Å to $\sqrt{190^2 + 200^2} = 280$ Å, which is a factor of 1.5. Thus the Coulomb energy will be reduced by a similar factor.

The mechanisms described so far have been of equal importance to both electron and hole systems. However, the differences in exchange interaction in hole systems extend beyond arguments concerning effective mass and kinetic energy (as described in Section 3.5).

The lack of an appropriate theoretical framework makes the discussion of the results rather difficult. A pragmatic approach will be taken henceforth, in which the hole system will be assumed to be similar to a heavy-electron system at zero B. At higher B the interactions between holes in Landau levels of mixed spin character will be assumed to be described by a Hartree-Fock-like equation (see equations 3.11 to 3.13). The coefficients A_{ij} (see below) will be 'measured' from experiment.

5.4.4 Qualitative extension for the 2DHS

The predictions of the first-order phase-transition theory were calculated in Chapter 3, for electron-like Landau levels, and are repeated below. The reader is reminded that coefficients A_{ij} represent the exchange energy of interaction between a particle in Landau level i with all of the particles in Landau level j of the same spin, where the i and j are *harmonic oscillator* labels. Hole Landau levels are conventionally labelled with the index m, which is an integer defining the set of coupled differential equations from which the Landau level was calculated. However, in the axial approximation, the particular solution labelled m may also be labelled according to its harmonic oscillator function. For the values of $B_\perp$ used in this thesis, the Landau levels have harmonic oscillator labels $N = 0, 0, 1, 1, 2, 2, ...$ in order of increasing energy, just as in

the electron case (see Fig. 5.1). Thus the conventions for the A_{ij} are retained.

The important predictions of the theory outlined in Section 3.4, and depicted in Fig. 5.6, are that: (i) the transition occurs at some magnetic field B_C which does not necessarily equal the non-interacting crossing point; (ii) the single-particle excitation gap Δ_C is non-zero at this magnetic field.

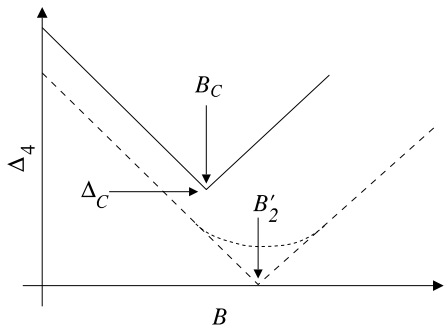

Figure 5.6: Schematic diagram showing the expected properties of the phase transition described in Section 3.4. The dashed line shows the non-interacting energy gap; the dotted line shows a non-interacting anticrossing.

In the simple electron theory for an ideal 2DS, the phase transition occurs at a *lower* magnetic field than that defined by $g\mu_B B = \hbar\omega_C$, and with a single-particle excitation gap $\Delta_C = (A_{11} + A_{22})/2$.

The energy of excitation at odd filling factor $\nu = 2N + 1$ may be written as $\Delta_{2N+1} = g\mu_B B + A_{NN}(l_B)$, following equation 3.12. In a tilted field experiment at constant filling factor, $B_\perp$ is held constant. Hence the exchange energy remains constant and Δ_{2N+1} traces a straight line starting at the minimum total magnetic field $B = B_\perp$, with a positive gradient of $g\mu_B$. For simple electron-like bands, the value of A_{NN} (which represents the exchange enhancement of the g factor) can therefore be obtained by extrapolating the data to $B = 0$.

From Fig. 5.4, the value of A_{22} may be determined by extrapolation to be (4.0 ± 0.1) K, for sample T240. In this simple electron-like analysis, the exchange energy per particle of the system has been measured at $\nu = 5$. The apparent consistency of the 2D g factors at $\nu = 4$ and $\nu = 5$ suggests that the spin compositions of the levels are similar. This means that it is valid to estimate the A_{22} exchange energy at $\nu = 4$ by scaling the $\nu = 5$ result by the magnetic length. The steep gradient and scatter of the Δ_3 data (Fig. 4.10(b)) prevent a similar extrapolation for the A_{11} coefficient.

The measured quantity $\Delta_{TP} = (3.7 \pm 0.1)$ K at $\nu = 4$ appears to be roughly consistent with the value of Δ_C calculated from the value of A_{22} estimated from the data: $(4.0 \pm 0.1) \times \sqrt{5/4} = (4.4 \pm 0.12)$ K, assuming that $A_{11} \approx A_{22}$. In the simple electron-like theory, A_{11} and A_{22} differ by just 17%, which partially justifies the approximation $(A_{11} + A_{22})/2 \approx A_{11}$.

Continuing this analysis it is possible to show, using equation 3.17, that the exchange-driven phase transition occurs approximately 2 T before the non-interacting Landau levels would have crossed.

5.4.5 Discussion

It has been argued that the concept of exchange should be incorporated into the understanding of the energy gaps at both even and odd filling factors. That the exchange energy then drives a rearrangement of the levels, as a function of tilt-angle and total magnetic field, seems natural. It is therefore possible that the lack of positive curvature in the Δ_4 versus B dependences of T240 and T335n+ occurs because the levels have not yet approached sufficiently to mix strongly. The first-order phase transition pre-empts this mixing, so the turning point is rather sharp.

The value of A_{22} has been determined by extrapolation. This procedure implicitly assumes that the g factor is isotropic and independent of both $B_\perp$ and $B_{||}$. The simplistic analysis of the data for the tilted field regime, $B > B_\perp$, is partially defensible because of the linear Δ_4 versus B relationships in two samples. However, it is not realistic to assume that the Landau level structure as a function of $B_\perp$ is well described in terms of simple g factors and effective masses (see Section 5.3.3). Hence, the value of A_{22} has entirely neglected the non-linearities of the hole Landau level splittings as a function of $B_\perp$. The error caused by this assumption is difficult to estimate, and could result in either an overestimation or an underestimation of the exchange energy.

Figure 5.3(a) shows that at the turning-point for $\Delta_{-1,3}$, marked by B_2, $\Delta_{-1,3}$ is greater than zero. This energy gap was included in that diagram because, in that discussion, Δ_{TP} was assumed to be due to a non-interacting anticrossing effect which could also occur below the chemical potential.

In the simplest interactions theory, Δ_{TP} is equal to Δ_C, and $\Delta_{-1,3}$ must equal zero at B_2 (assuming there is no anticrossing): there is no interaction-driven phase transition between two occupied Landau levels.

In Fig. 5.3(a), the magnetic field B_2 represents the crossing point of the $m = 3$ and $m = -1$ Landau levels at $\nu = 5$, and occurs at (8.2 ± 0.2) T. The change in $B_\perp$ between $\nu = 4$ and $\nu = 5$ should increase this non-interacting crossing field to some new field B_2'. In the phase-transition theory, $B_{TP} = B_C < B_2'$ (see Fig. 5.6). It was estimated in the previous section that $B_2' -$

$B_C \approx 2$ T. Thus, the phase-transition theory predicts that $B_2' \approx 11$ T.

To test this prediction, we refer to the measured value of $B_2 = (8.2 \pm 0.2)$ T. If a simple phase transition does occur, it is required that the B_2 increases by a factor of 1.35 to 11 T due to an increase in $B_\perp$ by a factor of only 1.25. Although this could not happen in an electron-like system, because of the linearity of the electron Landau fan diagram, it is possible in the hole system. This test therefore does not distinguish between the anticrossing and phase-transition theories.

It is appropriate now to consider the results of Kemerink *et al.* [91] in more detail. The latter paper was published independently of, and after, the publications resulting from this thesis. The samples studied in that work were (100) asymmetrically-doped GaAs/AlGaAs quantum wells of width 90 Å. The carrier concentration was 9.55×10^{15} m^{-2}, which is very high; the mobility of their samples was omitted from the paper but may be expected to have been rather low. They performed **k**.**p** calculations beyond the axial approximation, and found that the ρ_{xx} versus $B_\perp$ data could not be fitted for any choice of disorder broadening.

However, by introducing simplistic exchange effects at odd filling factors only (which corresponds to selecting $A_{ij} = 0$ if $i \neq j$), they were able to reproduce their experimental data. They determined the value of the exchange energy to be approximately $4 \times \sqrt{B}$ KT$^{-1/2}$. Scaling this value for our carrier concentration gives an exchange coefficient $A_{22} \approx 2.4$ K, which is in approximate agreement with our estimate of (3.7 ± 0.1) K.

Kemerink *et al.* end their paper by stating that the rearrangement of Landau levels, as a function of $B_\perp$, due to exchange interactions is essential for a proper description of the 2DHS.

The role of disorder has been neglected so far. It is argued in Chapter 3 that disorder affects the phase-transition if the disorder tails of the Landau levels start to overlap. The effect is to rapidly quench the exchange contribution to the single-particle excitation gap, thereby causing negative curvature in the vicinity of the turning point. From the estimates of the disorder width of the Landau levels presented in Section 4.3.3, it is clear that disorder is unlikely to affect the existence of a transition. It is tempting to attribute the negative curvature of the data in Fig. 5.2 in the vicinity of B_{TP} to the disorder. However, the data exhibit only a small deviation from linearity, which could originate from systematic effects in the activation plots (see Section 4.3.3).

5.4.6 Comparison of T335n+ and T240

Sample T335n+ was chosen for study because of its lower carrier concentration (1.3×10^{15} m^{-2} in comparison with 1.8×10^{15} m^{-2}). It was hoped that

the changes in Δ_{TP} and B_{TP} would make it possible to distinguish between possible physical mechanisms.

In fact, it was found that the energy gaps at $\nu = 4$ were very similar in size but that the gaps at $\nu = 5$ were much smaller. This is contrary to what would be expected for the electron system, where the cyclotron energy (at fixed filling factor) would be reduced by the ratio of the densities, but is not surprising given the complex hole Landau level structure.

At fixed filling factor, any linear function of the exchange energy varies as $\sqrt{n}$. Hence, the size of the exchange gap Δ_C can be expected to be smaller by a factor of $\sqrt{1.8/1.3}$. Thus, the first-order phase-transition theory predicts that the Δ_C of T335n+ should be approximately (3 ± 0.1) K. By extrapolating the data in Fig. 5.2 to the turning point the gap may be estimated to be $\Delta_{TP} \approx (2.25 \pm 0.5)$ K. The trend is therefore in the right direction but the measured value is a little too small. The discrepancy might be explained by the differences between the disorder widths of the Landau levels, which are greater in the case of T335n+ due to that wafer's significantly lower mobility.

5.5 Mixing and exchange

The previous sections have presented discussions in opposite limits of the same problem. A complete explanation of the data is certain to incorporate both anticrossing and interaction elements. This experiment takes the sample between a paramagnetic and a ferromagnetic phase. Although the exchange interaction is complex in the valence band, it must exist and therefore favour the ferromagnetic state. Indeed, unscreened Coulomb interactions are the largest energy scale in this problem.

The exchange contribution to the single-particle excitation gaps of the system requires there to be a distinction between the Landau levels involved. In the regime of strong mixing, the 'spin' character of the approaching Landau levels is blurred. Therefore, it seems plausible that the exchange contribution, which is at full strength when the Landau levels are well separated, is quenched as the Landau levels approach. Thus, as the energy gap decreases, the exchange contribution to it decreases also. This process could offset the positive curvature which would have indicated anticrossing, thereby sharpening the Δ versus B dependence in the vicinity of B_{TP}. Indeed, if the mixing is sufficiently strong, the first-order phase-transition may not occur [127]. This effect is depicted schematically in Fig. 5.7.

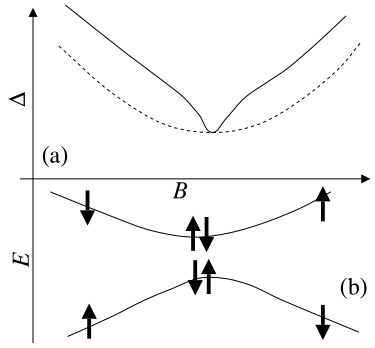

Figure 5.7: Schematic diagram showing how mixing could quench the exchange enhancement of an energy gap, and offset positive curvature due to anticrossing. The measured energy gap is plotted using a solid line in (a). The dotted line shows the non-interacting energy gap between the anticrossing Landau levels, the energies of which are plotted in (b).

5.6 Conclusions

The discussion of the possible explanations of the observations at $\nu = 4$ in samples T240 and T335n+ has centred on attempting to distinguish between a 'perturbative' mechanism in which the approaching Landau levels anticross, and a first-order phase transition of the type described in Chapter 3 in which exchange interactions drive a discontinuous change in the magnetization of the system.

The non-interacting hole picture can explain some of the features of the data. The failure of the Landau levels to cross at even filling factors is to be expected because of the low symmetry of the system. This certainly explains the observations at filling factors $\nu = 6$ and $\nu = 8$, where the Shubnikov-de Haas oscillations indicate non-zero energy gaps for all tilt angles. This picture explains the difference in the shapes of the Δ versus B curves at $\nu = 4$ and $\nu = 5$ to be due to the fact that at $\nu = 5$, the Landau levels above and below the chemical potential cross at different angles. However, the non-interacting hole model fails to explain the sharpness of the Δ_4 turning point.

In contrast, the interactions mechanism accounts for the sharp turning point at $\nu = 4$ quite naturally in terms of a first-order phase transition which pre-empts an anticrossing. The concept that the energy gaps at integral filling factors are enhanced by exchange interactions is a standard part of the understanding of electron systems. However, there are very few measurements

demonstrating its importance in hole systems, despite the fact that exchange is a fundamental property of many-particle fermionic systems. Simple considerations indicate that the Coulomb interaction is the dominant energy scale of the system.

In the presence of an exchange energy, it is natural that the system will undergo a rearrangement of its Landau levels at some critical angle of tilt. This is because the exchange energies of the paramagnetic and ferromagnetic states are very different. Convincing experimental observations of such a phase transition have not been reported previously. We have argued that, in our samples at $\nu = 4$, this process may occur before the Landau levels start to anticross strongly and therefore appears as a lack of curvature in the Δ_4 versus B data. The energy gap at the 'transition' point is consistent with the exchange energy crudely estimated from $\nu = 5$ data, and also with values published in a very recent paper by another group. This picture can also account for trends observed between two samples of differing carrier density.

At present, it is impossible to rule out a single-particle explanation of the data. The final answer will require further experiments and new calculations; ultimately, the explanation will no doubt incorporate elements of both arguments.

Chapter 6

One-dimensional hole systems

6.1 Introduction

6.1.1 Previous Work

Schottky gates were first used for the imposition of a potential varying on the length scale of the Fermi wavelength over ten years ago [33]. The subsequent discovery of the quantization of conductance in short quasi-1D electron systems [36, 37] stimulated extensive research into the properties of electrons in small structures [15]. However, the study of the quantum transport properties of low-dimensional hole systems has barely begun. Work on the latter subject in the GaAs/AlGaAs system is mostly restricted to that of Zailer [71, 14], which reported a number of new experimental observations. The first observation of conductance quantization in the 1DHS, over five years after its discovery in the 1DES, demonstrated the quantum ballistic properties of holes. The structures measured were plagued by intrinsic noise, which prevented anything but the simplest of experimental investigations of their properties. Very clear Aharanov-Bohm oscillations were observed at high magnetic fields in anti-dot structures, demonstrating clearly the phase-coherent nature of the hole transport.

The tunnelling of holes in small Si-based structures [128], and a number of papers describing the transport properties of hole systems containing very small self-organized dots [129, 130] offering large confinement energies, have also been published.

Other experiments, which demonstrate the classical ballistic transport of holes in small structures, have also been reported. Of these, the most significant are the magnetic focussing experiments of Heremans *et al.* [38, 39, 11].

The reason for the lack of progress in the study of the transport properties of holes confined to less than two dimensions is twofold. Firstly, the high

hole effective mass reduces characteristic quantum confinement energies thus necessitating lower disorder and measurement temperatures. Secondly, the fabrication technology was significantly less developed.

For completeness, we mention optical measurements of long quantum wires which reveal strongly anisotropic behaviour when the light is linearly polarized with the electric field parallel or perpendicular to the wire axis (see for example reference [131]). Such effects are attributed to a combination of the 1D quantization of the electronic states and valence band mixing effects [132, 133, 134].

6.1.2 Contents of this chapter

This chapter begins with a description of the properties of 'ideal' one-dimensional systems. It goes on to describe a method for the fabrication of one-dimensional hole systems. After a description of the basic properties of these devices, DC source-drain bias measurements are presented which enable the determination of the energy spacings between the 1D subband edges of a constriction. This result will be used in later chapters, and represents the first measurement of the subband spacings of a 1DHS. In addition, data analysis techniques are introduced which will be used throughout the remainder of this thesis. A discussion of the differences between the 1DES and 1DHS, in the context of **k**.**p** theory and interactions, is deferred until Chapter 7.

6.2 Ideal split-gate devices

6.2.1 Formation of a constriction

In this section, the electrostatic properties of ideal split-gate devices are briefly described. The 1DS is created by the application of a voltage, V_{g}, to lithographically defined split gates, which remove charge capacitively from the 2D regions in their vicinity. This is depicted schematically in Fig. 6.1(a).

The potential energy, $q\Phi$, of particles in the two-dimensional plane forms a smooth surface exhibiting a saddle-point in the vicinity of the constriction, as depicted in Fig. 6.1(b). The lateral confinement, which quantizes the planar motion of the particle into 1D subbands, is provided in the x direction; and current flow occurs in the y direction. Where the confinement is weak, the energy spacing between 1D subbands is very small and many are occupied for a particular chemical potential. In contrast, at the saddle-point, the confinement is strong; the energy spacing between the 1D subbands is increased and very few are occupied. They are marked in the Fig. 6.1(b) by the dotted lines.

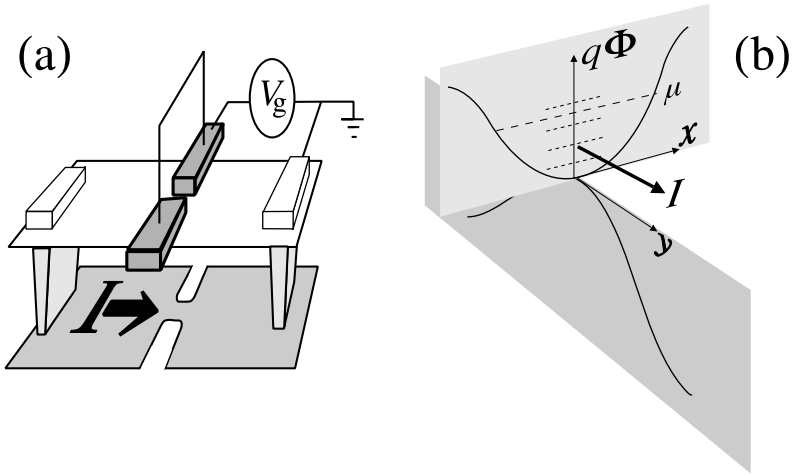

Figure 6.1: (a) A schematic diagram of the split-gate technique for the definition of short 1D constrictions on 2D layers. Metal (dark) is deposited on the surface of a chip. By the application of a voltage with respect to ohmic contacts connected to the 2D layer, particles are excluded from regions beneath the metal and a constriction is formed. (b) Diagram showing the potential energy as a function of position in the plane, near to the constriction. The dotted lines represent the energies of 1D subbands formed by the lateral confinement. The dashed line is the chemical potential.

6.2.2 A high-quality electron system

Figure 6.2 is a plot of the conductance G versus V_g for a very high quality electron split gate. The conductance was measured by the application of a small oscillating voltage V between the ohmic contacts, and by detecting the resulting current using low-frequency lock-in amplifier techniques: see Appendix D. The curve features three distinct regions. In the first, at low gate voltage, G is roughly constant. At -0.8V there is a sharp drop in conductance which is termed 'definition' and corresponds to the total depletion of the carriers from beneath the gate metal. The following gentle decrease in conductance is described as 'pinching off', and occurs as the width and number of electrons of the constriction are reduced. The conductance is quantized in even integral multiples of e^2/h (see the inset to Fig. 6.2).

6.2.3 Conductance quantization

The conductance quantization may be explained by consideration of the processes occurring as the constriction is pinched off. It is therefore necessary to introduce some more notation. The density of states at the saddle-point is

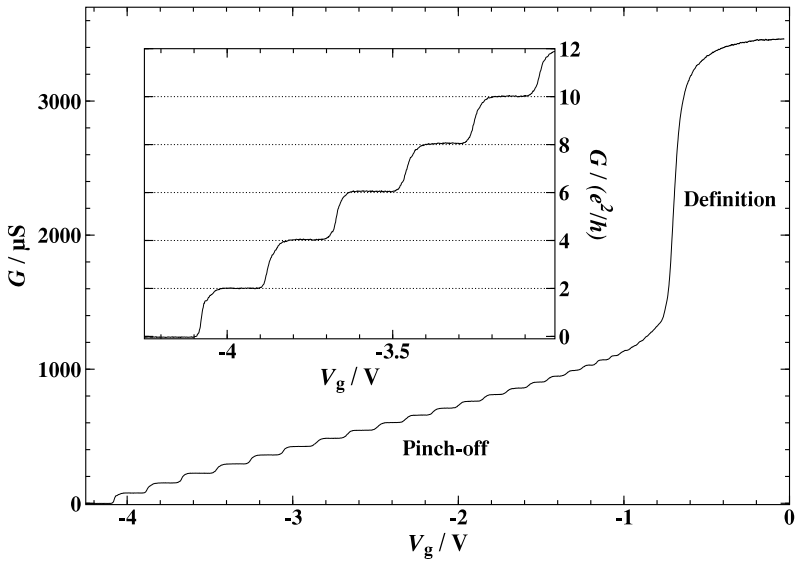

Figure 6.2: G versus $V_{\rm g}$, at $B = 0$ and $T < 80$ mK, for a very high quality *electron* split-gate device [courtesy of K. J. Thomas]. The curve shows characteristic 'definition' and 'pinch off'. There are plateaux in the pinch-off region (inset).

depicted in Fig. 6.3. It is characterized by cusps, which occur at the edges of each 1D subband and arise from the form of the density of states of one 1D subband, $d(E)$:

$$d(E) = \frac{1}{\pi}\frac{\partial k}{\partial E} = \frac{1}{h}\sqrt{\frac{m^*}{2E}} \tag{6.1}$$

which diverges at $E = 0$. The total density of states, $D(E)$, is a sum over 1D subbands. The energies of the subband edges have been labelled E_i.

In Section 1.6.1, it was shown that the conductance, G, of the device is determined by the one-dimensional modes which are transmitted between the source and drain ohmic contacts:

$$G = \frac{e^2}{h}\sum_{kl} T_{kl} \tag{6.2}$$

where T_{kl} represents the probability that a particle emitted by the source in the kth mode is transmitted into the lth mode of the drain, *at the chemical potential*.

The simplest way to explain the quantization of Fig. 6.2 begins with the assumption that there is no inter-subband scattering; see also references [135] and [15]. Then, $T_{kl} = T_{kl}\delta_{kl} = T_l$. In the ideal case, $T_l = 1$ for $E_l < \mu$ and

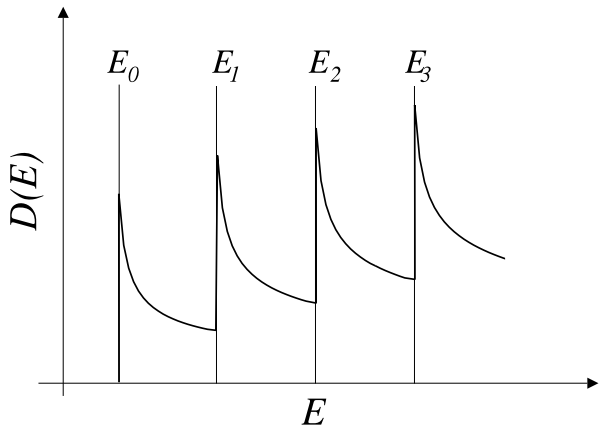

Figure 6.3: The density of states of a quasi-1D system.

$T_l = 0$ for $E_l > \mu$. Then, the conductance simply 'counts' the number of 1D subband edges below the chemical potential; it is therefore quantized in some integer multiple of e^2/h. As the device is pinched off, the energy spacings between the 1D subbands increase as the confinement increases. Thus, the ladder of 1D subbands moves with respect to the chemical potential. For a range of $V_{\rm g}$, the same number of 1D subbands remain occupied, and despite the fact that the number of particles in each subband decreases, G is unchanged. Hence, a plateau is observed in the G versus $V_{\rm g}$ data. Eventually, a 1D subband edge passes through the chemical potential, and the conductance very quickly becomes quantized at a new, lower, multiple of e^2/h.

Figure 6.2 exhibits quantization in even integral multiples of e^2/h because of the spin-degeneracy of the electron system.

6.2.4 Limits on observation of quantization

The simplistic analysis presented above was based on a model in which 1D modes connected perfectly to the two reservoirs between which the current flowed (see Section 1.6.1). It provides two criteria that a real device must satisfy in order that its conductance be quantized.

The first is that the sample temperature is sufficiently low that the Fermi-Dirac distribution does not 'smear' the plateaux out. The characteristic width of the 'smearing' of the Fermi-Dirac distribution is approximately $4k_BT$; it is therefore required that the energy gap between 1D subbands at the chemical potential, $\Delta_i^{\rm 1D}$, exceeds $4k_BT$.

Secondly, it is required that there be no back-scattering of particles in modes below the chemical potential. The presence of impurities in the vicinity

of the constriction can cause back-scattering, which destroys the quantization. The average distance travelled by a particle before it suffers a back-scattering event has been defined to be the transport length, l_{tr} (see Section 1.3.2). Hence, it is required that l_{tr} is much greater than the length of the 1D constriction. In this regime, the trajectory of the particle through the constriction is essentially ballistic; for this reason, conductance quantization in short 1DSs is often described as 'ballistic quantization'.

In a real device, the 'contacts' to the 1DS are those parts of the 2DHS more than l_ϕ from the constriction; and the nature of the coupling between the device and the 'contacts' is not necessarily ideal. These points are discussed in detail in reference [135]. In the case of an abrupt join between the 2D and 1D regions, quantum-mechanical reflection effects can result in so called 'length resonances' which introduce structure to the plateaux. These turn out to be more important in long devices. In short abrupt devices, plateaux acquire a non-zero slope.

The other case concerns an adiabatic widening of the 1D region into the 2D region. In this case, there are no reflection effects because the 2D and 1D regions are 'impedance matched', and the plateaux are well quantized provided that the entrance and exit to the constriction are much wider than its narrowest point.

6.3 Fabrication of 1DHSs

All of the one-dimensional hole devices to be described in this thesis were fabricated by the surface processing of 2DHSs, grown using MBE by Dr M. Y. Simmons on the (311)A facets of semi-insulating GaAs wafers. The surface processing was carried out using standard optical and electron lithographic techniques which are included for completeness in Appendix C.

6.3.1 Gating problems in hole systems

Figure 1.3(a), in Chapter 1, depicts schematically the spatial band structure of the shallow wafers used in the preliminary gating studies performed as part of this work. Important features include the shallow depth of the 2DHS (≈ 800 Å), which is confined to an asymmetric single-interface heterostructure, and the high silicon doping concentration of 1.2×10^{18} m^{-3}.

Figure 6.4(a) shows that one such wafer (T136) could be pinched off by increasing the voltage on optically-defined side gates, despite the 40 μm separation of the gate fingers. This effect, which has been termed 'lateral depletion' has been observed before [71]. The conductance of a similar electron system would show little or no variation over this gate-voltage range. Figure 6.4(b)

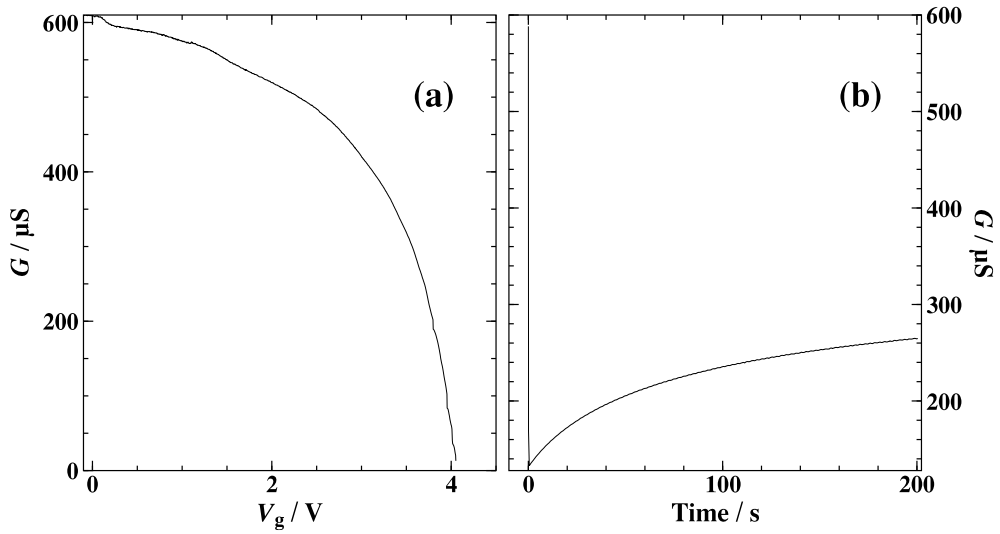

Figure 6.4: (a) The conductance of nine squares of 2DHS (T136) could be reduced to zero by the application of quite modest *side-gate* voltages. This effect is termed 'lateral depletion' and is a particular problem in small-structure fabrication. Similar behaviour is not observed in typical 2DESs. (b) The time response of G following a step increase in the voltage on a full gate, indicating charging effects.

shows the transient reponse of the system to a step increase of the voltage on 2D front gates. Such front gates differ from split gates because they entirely cover many squares of the 2DHS, and are therefore essentially macroscopic. The conductance is seen to drop sharply for positive steps in the gate voltage and then to decay approximately exponentially to a less pinched-off value. If the front-gates of such a system are swept, G is found to vary hysteretically.

The problems of hysteresis and lateral depletion were observed in measurements of all of the 'shallow' wafers (T116, T136, T119, T97, A676) used for these studies. They are examples of the effects of the transfer of charge from the 2DHS, or front gate, to states either at the interfaces or in the semiconductor itself. The lateral depletion is particularly undesirable, because the large connecting gate pads would tend to pinch off the constriction before the fine features were defined, thus prohibiting the formation of a narrow channel.

At important stages in the processing of the chips, such as immediately before the evaporation of metals, it is standard clean-room practice to wash them in an aqueous HCl solution for ten or more seconds (see Appendix C). HCl is believed to strip the oxide which forms on the surfaces of the samples, and thereby to remove 'dirt' which may have adhered to the oxide. To investigate whether a different cleaning process would solve the problems of lateral

depletion and hysteresis, a comparison was made of the properties of chips of T136 subjected to cleaning by NH_3 or HCl solutions, or simply water. At a temperature of 4.3 K, no differences were observed between the samples.

The first ever 1DHSs to exhibit ballistic quantization [71, 14] were fabricated on a similar wafer (T97), with a carrier concentration and mobility of approximately 2×10^{15} m^{-2} and 50 $m^2V^{-1}s^{-1}$ respectively. The 2DHS was contacted using annealed InZn ohmic contacts. The 1D channel was defined using an etching technique, whilst pinch off was achieved using NiCr/Au split gates. These were evaporated onto the chip following an acid etch, which was performed after the development of the resist [71]. The etch, which was used to limit lateral depletion effects, removes much of the flexibility of Schottky gating, because it leaves regions of the device depleted at $V_g = 0$. Furthermore, devices fabricated in this way suffered from serious intrinsic noise problems; only three 1D plateaux were observed after the averaging of fifty data sets, and experiments on the properties of the split gates proved to be impossible.

6.3.2 A new method for the fabrication of 1DHSs

Many problems were encountered during the attempts to fabricate a working 1DHS. Over 150 split gates were tested at temperatures of 4 K or below. The majority of these were patterned on the shallow, high dopant concentration single-interface wafers. Although designs using combinations of etching and gating were fabricated, those tested at 'millikelvin' temperatures did not exhibit ballistic quantization. The primary reason for this failure is thought to have been the lateral depletion effect, which prevents the formation of a narrow constriction. Secondary reasons may have included relatively small gate leakages of around 1 nA at pinch off. It is remarked that, in contrast to the work of Zailer (which used InZn ohmic contacts), AuBe ohmic contacts were employed in all of the studies presented here.

Success followed the change from these shallow, highly doped wafers, to T240. This exceptional wafer, whose properties are discussed in Chapter 1, differs by: (i) having lower dopant concentrations; (ii) a commensurately larger doped region, and therefore a deeper 2DHS; (iii) close to symmetric confinement; (iv) a very high mobility.

The lateral depletion problem of the shallow wafers was found to be much reduced in wafer T240. It seems likely that the observation of conductance quantization in devices made from this wafer is related to this improvement. It is tempting then to attribute the lateral depletion effect to low temperature charge mobility in the doped regions of the semiconductor, because such processes should be inhibited by an increase in the mean inter-dopant spacing.

The particular samples (or chips) measured in the course of this work were

labelled J1 to J12. On a typical chip, as many as six split-gate structures (or devices) can be fabricated. The study of split gates on T240 began with a measurement of the lateral depletion from optical side gates. Then, a series of split gates were patterned onto chips J5 and J6 (see Fig. 6.5). Those on J6 were of standard geometry, with lengths of 0.4 μm and widths in the range $0.9 \rightarrow 0.5$ μm. They were measured at 300 mK, and were not found to be ballistic. More importantly, they were also found to be particularly unstable: if $V_{\rm g}$ was increased so that G decreased to 350 μS, the whole channel was found to pinch off in approximately 200 seconds.

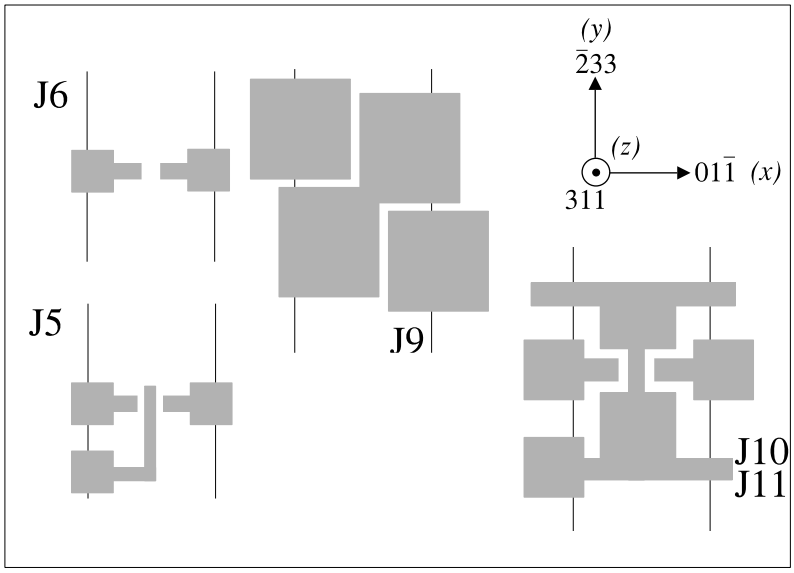

Figure 6.5: Gate-pattern designs for a series of split gates on chips of T240. Metal is shaded.

In contrast, the J5 devices incorporated an extra sub-micron gate oriented along the channel. The purpose of this 'mid-line' was to provide more control of the constriction potential; in particular it was thought that it might have limited the instability that had been observed in earlier devices. Devices on J5 were tested at 4 K and below, and were indeed found to have improved stability properties. Figure 6.6(a) shows the stability of G for incremented $V_{\rm g}$, obtained at 70 mK. Figure 6.6(b) shows a typical pinch-off curve, in which two quasi-plateaux are visible at low conductances. However, it proved to be difficult to show that they were of ballistic origin.

Given the partial success of this technique, it was decided to extend the mid-line to divide the two sides of the Hall bar completely. The resulting chips exhibited smoother pinch-off characteristics. An SEM micrograph of

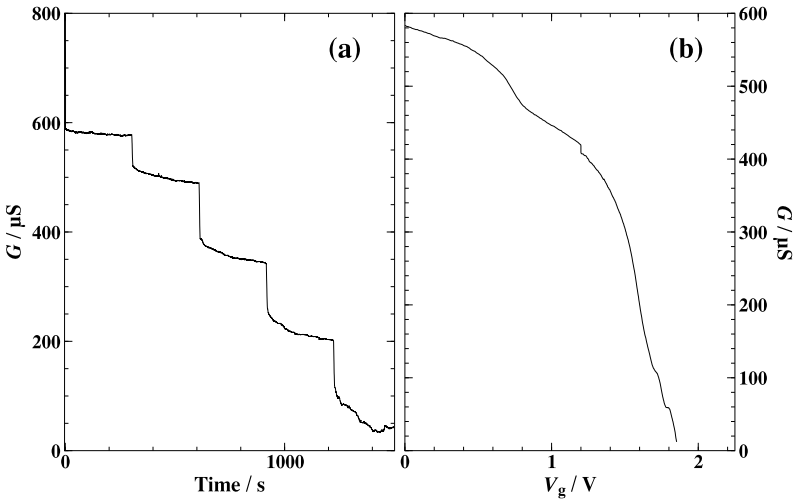

Figure 6.6: (a) Stability and (b) pinch-off curves for a split-gate device on chip J5. The mid line was set to -0.37 V, and the temperature of the device was 70 mK. Note the two 'plateaux' at approximately 1.8 V, with conductances of about 100 μS and 50 μS. (The discontinuity at 1.2 V is due to a change of the sweep rate of V_g.)

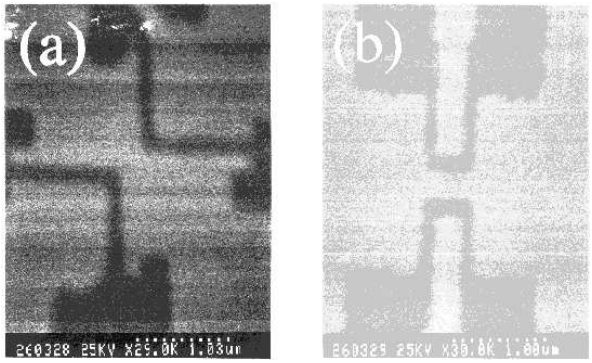

Figure 6.7: (a) J9 and (b) J10 working split-gates. Metal is lightly shaded. The Hall bars run from left to right, and were oriented in the $[\overline{2}33]$ crystallographic direction in each case.

one working design (J9) is presented in Fig. 6.7(a). It was defined between two offset squares of gate metal, which have been shown to produce large 1D-subband energy spacings in the 1DES [136]. Another pair of squares were inset to form a 'bowtie'-shaped mid-line. Finally, a layer of cross-linked PMMA was deposited on top of the active area of each device.

Devices J10 and J11 were patterned more conventionally, as indicated in Fig. 6.5; an SEM micrograph of a working device from chip J10 is presented in Fig. 6.7(b).

Although the chips J9 and J10 contained more than one device, it happened that in both cases one of the devices displayed superior properties to the others on the chip. Results presented henceforth will come from the best devices in each case, and which will be referred to as J9 or J10.

The crystallographic orientations of the devices are indicated in Fig. 6.5. Although the Hall bars were oriented along the $[\overline{2}33]$ direction in both cases, the current through the 1D region of device J9 flowed at 45° to this direction.

Measurements at temperatures below 70 mK are presented in Fig. 6.8, for devices J9 and J10. All of the 1DHS conductance measurements to be presented in this thesis were performed in the constant-voltage configuration, with excitation voltages of less than 10 μV; see Appendix D for more details. Unless otherwise stated, the data were obtained at temperatures below 100 mK.

The data exhibit numerous plateaux at low conductances, which proved to be robust to thermal cycling. It was found that the best 'plateaux' were obtained for the most negative possible mid-line voltages. The thresholds for forward bias of the mid-lines of the devices studied as part of this work varied between -0.42 V and -0.5 V, and depended on the particular cooldown. The mid-line voltages were set to -0.4 V in all of the measurements to be described in the remainder of this thesis.

6.4 Basic properties

6.4.1 Plateau quantization

Representative data in the region of interest, from devices J9 and J10, are plotted in Fig. 6.9(a). The conductance axis has been divided by e^2/h, and horizontal lines representing quantized conductance values have been provided as guides to the eye. It is immediately apparent that the plateaux do not take correctly quantized values. Part of the reason for this is that the data plotted are the two-terminal conductances of the *whole device*, and include the series resistances of the wires connecting the sample to the measurement apparatus, and the annealed ohmic contacts. These were not considered in the simple model used earlier to explain the occurrence of conductance quantization.

The resistances of the wires and ohmic contacts may be eliminated experimentally using four-terminal measurement techniques (see Appendix D) in which different contacts are used for voltage probes and current sources and sinks. However, in order that such voltage probes measure an equilibrium

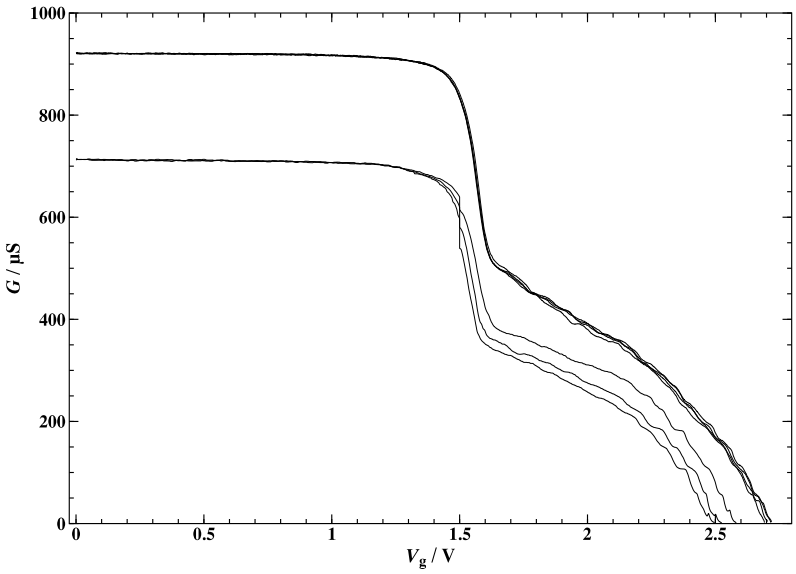

Figure 6.8: Three traces from training sweeps of devices J9 and J10, for $T < 70$ mK. The conductances at $V_g = 0$ are different because of different ohmic contact resistances (J10 data are lower). The mid-line voltage is -0.4 V.

quantity, it is necessary that they are situated more than a few transport mean free paths from the constriction. Thus, there will always be some additional contribution to the resistance of the actual constriction. In a high mobility device, this 'extra' resistance is small. Nevertheless, it limits the quantization accuracy to around 1% [15]. This is far poorer than the accuracy achieved in the quantum Hall effect, where values accurate to 1 in 10^7 may be measured in large Hall bars [25].

In a typical electron sample, it is found that the plateaux may be fitted to quantized values by the elimination of a series resistance with values close to the measured two-terminal resistance at $V_g = 0$ [137]. However, it is impossible to 'correct' the plateaux observed in the 1DHSs measured here by the choice of any constant series resistance.

6.4.2 Series-resistance corrections: discussion

As discussed above, measured plateau conductances may deviate from the expected conductance because of contact resistances. For the purposes of this discussion, we define R_0 to denote a constant contact resistance arising from the connections to the 1D constriction. It can include contributions from the wires and ohmic contacts, the 2DHS and also the coupling between the 2D

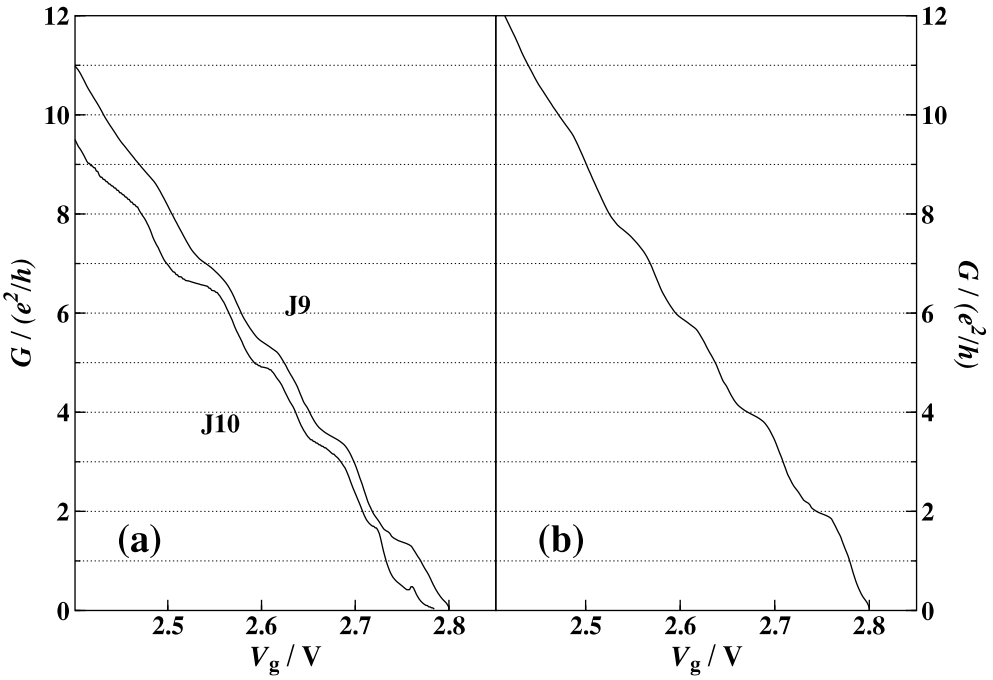

Figure 6.9: (a) G versus V_g for J9 and J10, showing plateaux. (b) The plateaux can be forced to line up, using a contact-resistance correction which increases as the device is pinched off. (Device J9)

and 1D regions.

As mentioned earlier, R_0 can never be fully eliminated or measured, even by a four-terminal measurement. Furthermore, the latter confers no significant advantage over two-terminal measurements, provided that R_0 is small.

A second reason for lack of quantization could be that the true conductance of the constriction is not quantized in multiples of e^2/h. It has been suggested [138] that inter-particle interactions in an infinitely long 1DS (known as a Luttinger liquid) could cause a renormalization of the quantum of conductance

$$e^2/h \rightarrow Ke^2/h. \tag{6.3}$$

K is a constant with a value less than one for repulsive interactions, and one in the absence of interactions.

A circuit calibration error would also 'renormalize' the conductance in this way. However, the circuits employed in this work were calibrated to around 1% accuracy using a calibrated 10 kΩ resistor. The sizes of the quantization discrepancies eliminate this mechanism, which is therefore discounted from this point on.

Thirdly, it is conceivable that as V_g is increased towards pinch off, the series resistance to the constriction increases i.e. $R = R_0 + r(V_g)$. This effect could occur because the coupling between the 2D and 1D regions changes with V_g.

To investigate these possibilities, it is useful to eliminate the effect of the constant series resistance R_0. In Fig. 6.10, the dimensionless 'conductance'

$$F_i = \frac{1}{i}\frac{G}{e^2/h} \times \frac{1}{1 - R_0 \cdot G} \tag{6.4}$$

is plotted against i (where i counts the number of spin-resolved 1D subband edges below the chemical potential). Equation 6.4 was derived by considering the 'measured' conductance G of a resistor R_0 in series with a 1DS. Consider the case in which the plateaux are 'renormalized' by a constant factor K, because of some hypothetical physical process. The dimensionless conductance F simply equals K, provided the constant R_0 is known.

In Fig. 6.10, it has been assumed that R_0 is the resistance at $V_g = 0$, which in these samples was around 1 kΩ. Data presented come from three samples. In each case, F decreases as i is decreased and the peak value is less than one. Because it is unphysical to select a value of R_0 which is less than the ohmic

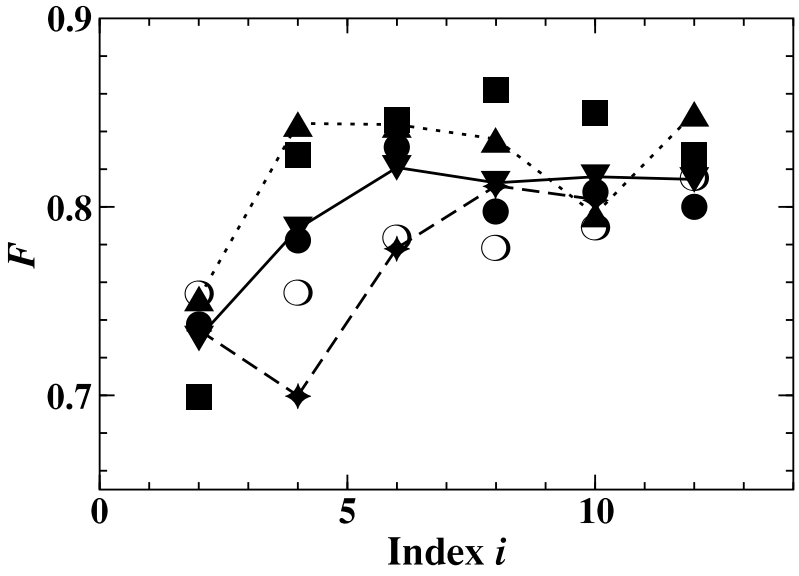

Figure 6.10: Dimensionless conductance F versus plateau index i for all measured cooldowns of three samples. See the text.

contact resistance, it proves to be impossible to force the data points to lie

on a horizontal line. If the highest index points are made to take $F_i = 1$, the slope on the data increases.

The figure shows that either R_0 or K varies with V_g. It is currently believed that the 1D conductance quantization is not renormalized by interactions in systems with non-interacting contacts [139, 140]. The qualitative reason for this is the conservation of momentum in the wire.

It therefore appears that the simplest explanation of the variation of F with i is a V_g-dependent series resistance. The variation in the resistance might be expected to occur due to changes in the coupling between the 2D and 1D states.

6.4.3 Instability

All of the devices measured in this work exhibited some degree of irreproducibility. A typical set of four sweeps measured in succession are plotted in Fig. 6.11. Crucially, each sweep exhibits features at the same conductances, although the gate voltage at which they occur varies randomly by approximately 50 mV. Furthermore, it was found that if the split-gate voltage was increased and then held constant at a conductance of less than 150 μS, then the device would pinch off against time. See also Fig. 6.4.

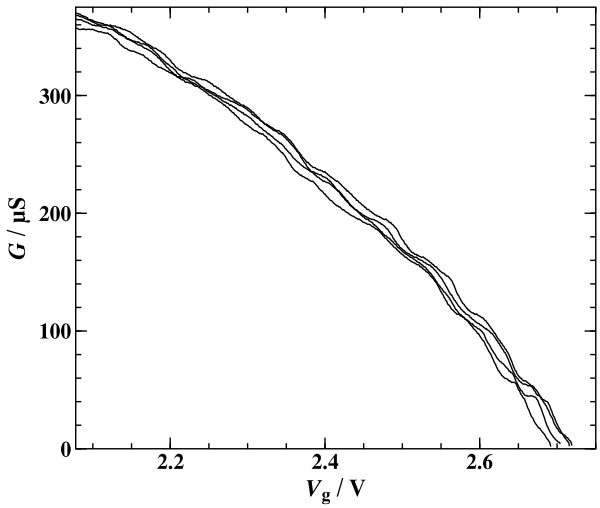

Figure 6.11: Four sweeps demonstrating device instability, showing that features in conductance are robust.

These properties were observed on different cryostats and experimental set-ups. These observations are largely independent of temperature, and can

be observed at 4 K (although there is no ballistic quantization). The possibility that they were caused by a trivial error in the experimental set-up was eliminated by the measurement of similar electron systems, which were found to behave normally. The possibility that the effect was in some way due to hyper-sensitivity to noise of mesoscopic hole systems is unlikely: no change in the effect was measured in constant-voltage or constant-current circuits deliberately designed to either minimize or maximize the noise.

One possible mechanism for this apparent 'V_g noise' utilizes the observation of lateral depletion. Lateral depletion occurs because of the flow of charge from gates to states either at the surface or interfaces of the sample, or to states in the bulk of the semiconductor. Strong evidence that the surface is not central to the lateral depletion problem was obtained in the course of the fabrication of the many split gates which led ultimately to the working designs outlined above. The band structures of the two types of wafer studied are presented in Fig. 1.3.

Despite the similarities between the surfaces, the shallow highly-doped samples (e.g. T136) exhibited far worse lateral depletion and no measurable time-dependent instabilities, whereas the samples with lower dopant concentrations (which also incorporated larger spacers) were unstable but suffered limited lateral depletion (e.g. T240).

One plausible explanation of these observations is that charge transport occurs between dopant sites in the bulk-doped regions, with a time constant that varies with inter-dopant separation. Thus, in the case of the stable samples, the lateral depletion would have occurred on a much shorter time-scale, and the device would have stabilized in its useless state 'instantly'. In the samples with dopants on average two times further apart, the screening effect of charge mobility in the bulk should be limited for measurements performed in a time less than the characteristic charging time and the lateral depletion effect would be inhibited. The motion of charge near to the constriction changes the local potential and introduce the observed instability.

6.4.4 Numerical averaging and greyscales

The quality of plateaux was found to decrease during experiments in which split gates were continuously swept from zero volts to pinch off. It was found that by sweeping the mid-line from -0.4 V $\rightarrow$ 0 V $\rightarrow$ -0.4 V after every eighth sweep of the split gates, the device retained its properties and lengthy experiments became reproducible.

A typical experiment involves the measurement of G versus V_g, as a function of a third variable X, which might be e.g. a magnetic field or DC source-drain bias. The data were often best represented as a greyscale of X versus G,

with a z axis of $-\partial V_g/\partial G$. Note that this method eliminates direct information about V_g; in high quality electron devices, greyscales are usually plotted as X versus V_g. This is preferable because of the capacitive link between V_g and energy. However, it was found that the instabilities of the devices precluded this possibility.

First, the data were corrected for series resistance as outlined above. This correction was determined from the data at $X = 0$ only. The V_g axis was then divided into equal length segments using a beta-spline algorithm. The numerical differential of the data was taken by counting these points into bins of length δG on the G axis and multiplying this number by $-\delta V_g/\delta G$. This gives $\partial V_g/\partial G$ directly. The mean of a number of sweeps was calculated by summation of these histograms.

6.4.5 Temperature dependence

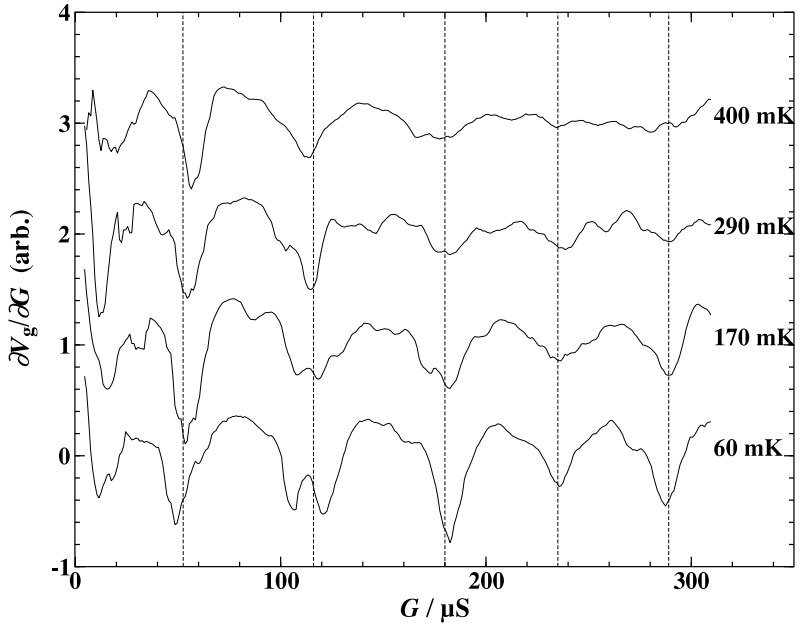

Figure 6.12: $\partial V_g/\partial G$ versus G (uncorrected). Data obtained from device J9, at four different temperatures. Plateaux are indicated by the minima.

Figure 6.12 plots $\partial V_g/\partial G$ versus G measured between temperatures of 60 mK and 400 mK. The minima represent plateaux in the G versus V_g traces. At 60 mK, five plateaux are detected. The increasing temperature smears the plateaux, with those of highest conductance the most strongly affected. At

400 mK, the plateaux at 235 μS and 280 μS have almost disappeared. This indicates that the energy spacing between those subbands is approximately $4 \times 0.3 = 1.2$ K.

6.4.6 Reflection of edge states

The application of a magnetic field perpendicular to the plane of the 2DHS ($B_\perp$) strongly affects the states both in the constriction and in the 2D regions. $B_\perp$ can be shown to cause a transition from electrostatic quantization to magnetic (i.e. quantum Hall effect) quantization [15]. The regimes of behaviour may be classified according to the energy scales of these two effects. The energy associated with the magnetic field may be approximated by $\hbar\omega_C$, whilst the 1D subband spacing due to the electrostatic confinement is described by $\hbar\omega_x$. The latter energy scale originates from the assumption that the lateral-confinement potential at the saddle-point (Fig. 6.1(b)) is parabolic, with curvature ω_x. This assumption is appropriate when screening is ineffective, which occurs when the constriction is occupied by few particles.

At low $B_\perp$, $\omega_c \ll \omega_x$, the electrostatic confinement dominates the constriction: the spacing of the levels is changed only weakly from the $B_\perp = 0$ values. The spacing of the levels starts to increase more quickly when $\omega_c \approx \omega_x$; a transport consequence of this is improved plateau flatness, as tunnelling and back-scattering are inhibited [15]. At high fields, $\omega_c \gg \omega_x$, the electrostatic confinement is irrelevant; the sample is in the quantum Hall regime and transport occurs via the transmission and reflection of edge states (see Section 1.5).

Data from J9 corrected with a *constant* series resistance R_0 are plotted in Fig. 6.13(a). $B_\perp$ has been increased in increments of 0.1 T. As $B_\perp$ increases, the higher conductance plateaux appear to be unaffected until fields of between 0.2 T and 0.3 T. For the plateaux at lower conductance, this occurs at approximately 0.4 T. Furthermore, plateaux emerge at approximately odd integral multiples of e^2/h, due to spin-splitting of the 1D subbands. This evolution of the conductance quantization suggests that the assignment of even indices to the plateaux at zero field is justified; each zero-field plateau is strengthened by $B_\perp$ and new plateaux emerge both above and below it with odd indices. This demonstrates a one-to-one correspondence between even filling factors and the electric quantization at $B = 0$.

Inspection of Fig. 6.13(a) shows that although the plateaux are poorly quantized at $B = 0$, the quantization accuracy improves as $B_\perp$ increases. The question of whether the plateaux really are affected strongly by a variable series resistance, or whether for some fundamental reason they do not take the normal quantization, is very difficult to answer. It is possible that some inter-

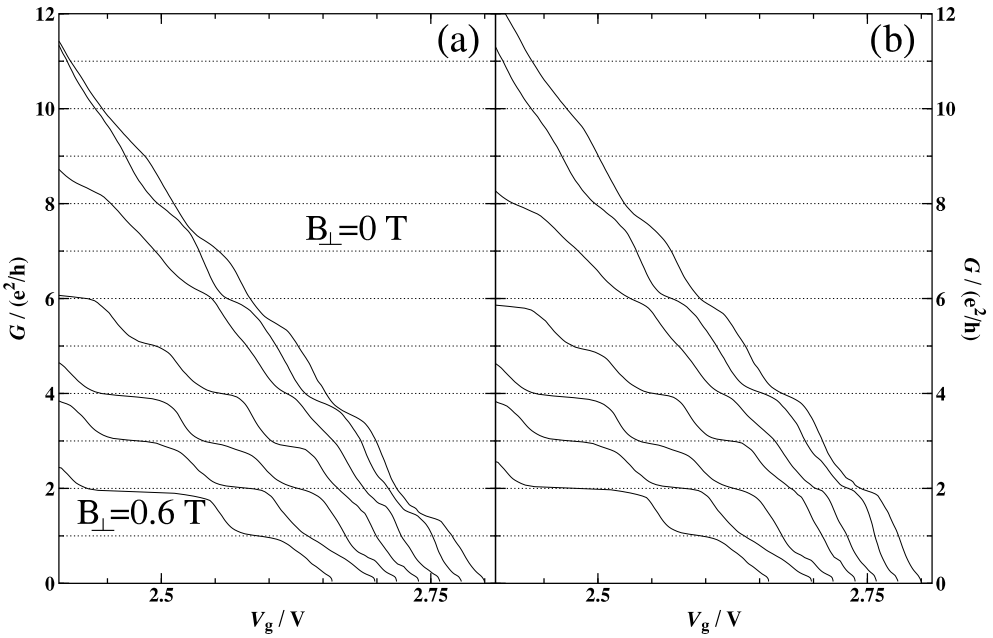

Figure 6.13: G versus $V_{\rm g}$ for $B_\perp$ incremented in 0.1 T steps. Traces have been sequentially offset in $V_{\rm g}$ for clarity. (a) G has been corrected for a constant series resistance. Spin-splitting and the transition to reflected edge-states occurs at about 0.3 T. (b) The same data, using a variable series-resistance correction.

esting 'interactions' process is being inhibited by $B_\perp$, and that the data show a cross-over from renormalized plateaux to properly quantized quantum Hall plateaux. On the other hand, it could be argued that whatever process causes lateral depletion is being inhibited by the magnetic field. For example, the nature of the coupling between 2D and 1D states is certain to be affected by $B_\perp$. Figure 6.13(b) shows data corrected using a $V_{\rm g}$-dependent series resistance.

6.5 DC source-drain bias

The use of a DC source-drain bias to measure the 1D subband energy spacings of split-gate structures is well established [141, 142, 143]. For a detailed description of the theory, see reference [144]. To date, no such measurements on hole systems have been reported in the literature due to the difficulty of fabrication of devices of sufficiently high quality. In this section, such measurements are presented and their consequences are discussed. They provide part of the information necessary for the measurement of the 1D parallel g factors of a 1DHS, which is described in Chapter 7.

6.5.1 Theory

The current-voltage relationship of a split-gate system is highly non-linear because of the quantized nature of the density of states. We consider a current I, which flows through the constriction due to a source-drain voltage V. The latter is composed of a constant 'DC bias' part, $V^{\rm sd}$, and an oscillating component δV. Hence

$$I = I(V) = I(V^{\rm sd} + \delta V) = I(V^{\rm sd}) + \delta V \frac{\partial I}{\partial V} \tag{6.5}$$

to first order. $\delta V = V_0 \cos \omega t$ is the signal detected by the LIA, which effectively multiplies the signal with the reference and computes the time average (see Appendix D). Representing the signal detected by the LIA as $\mathcal{V}$ we find:

$$\mathcal{V} = \langle I(V^{\rm sd}) \cos \omega t \rangle + \langle \delta V \cos \omega t \frac{\partial I}{\partial V} \rangle \tag{6.6}$$

which gives

$$\mathcal{V} = \langle V_0 \frac{\partial I}{\partial V} \cos^2 \omega t \rangle \tag{6.7}$$

thus demonstrating that the detected signal is proportional to the differential conductance G (both at zero and non-zero DC bias).

The flow of current due to $V^{\rm sd}$ is a non-equilibrium process which occurs because of differences in the electrochemical potentials of the source and drain ohmic contacts, which are μ_1 and μ_0 respectively. A suitable model system is depicted in Fig. 6.14. The whole of the applied voltage is assumed to be dropped across the constriction. For convenience the current is assumed to flow from left to right, as depicted in Fig. 1.9.

The Landauer-Buttiker formalism described in Chapter 1 indicates that each occupied transmitted subband contributes a current $e\Delta\mu/h$ to the current flow. In the derivation of conductance quantization, it was implicitly assumed that the same number of modes were available to the two ohmic contacts. However, this assumption is dropped here, and it is therefore necessary to replace the transmission coefficients T_j by $\overrightarrow{T_j}$ and $\overleftarrow{T_j}$. The net current is then found to be

$$I = \frac{2e}{h} \sum_j (\overrightarrow{T_j} \Delta\mu_1 - \overleftarrow{T_j} \Delta\mu_0), \tag{6.8}$$

where the factor of two arises from spin-degeneracy at zero B. For the purposes of this discussion $\overrightarrow{T_j}$ and $\overleftarrow{T_j}$ therefore count occupied spin-degenerate 1D subbands.

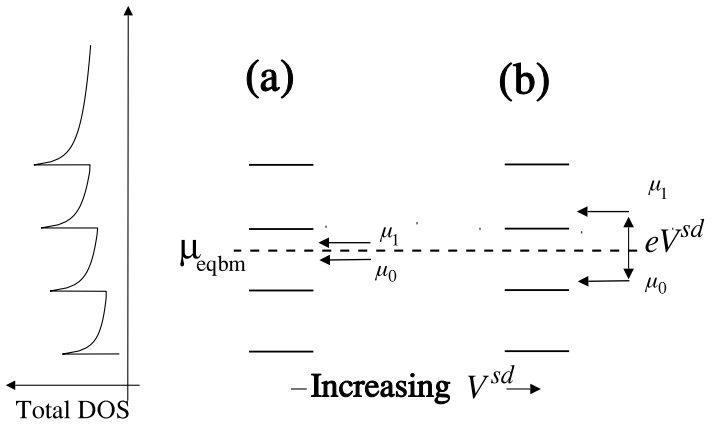

Figure 6.14: A model 1D system in which an applied DC source-drain bias, $eV^{\rm sd}$, separates the left- and right-going chemical potentials. Two regimes [(a) and (b)] are depicted, in which the number of occupied (spin degenerate) subbands for motion in both directions are equal, or differ by one.

The relationship between the electrochemical potentials and the applied voltage is usually described using the parameter β, where $\mu_1 = \mu_{\rm eqbm} + eV\beta$ and $\mu_0 = \mu_{\rm eqbm} - eV(1-\beta)$ [145, 144]. Thus the measured quantity $\partial I/\partial V$ is found to be:

$$\frac{\partial I}{\partial V} = \frac{2e^2}{h}\sum_j (\overrightarrow{T_j}\beta + \overleftarrow{T_j}(1-\beta)). \tag{6.9}$$

It is usually assumed that $V^{\rm sd}$ is dropped symmetrically, in which case $\beta = 1/2$ [142]. In the 'equilibrium' limit, which is depicted in Fig. 6.14(a), $\overrightarrow{T_j} = \overleftarrow{T_j}$ and the familiar ballistic quantization result is recovered. However, for larger values of $eV^{\rm sd}$ (Fig. 6.14(b)), the number of occupied left- and right-going channels differs by one and, according to equation 6.9, the plateaux occur at odd integer multiples of e^2/h. The appearance of odd plateaux in the absence of a magnetic field can be related to the coincidence of $eV^{\rm sd}$ with the subband spacing at the Fermi level. The use of DC-bias experiments to determine directly the energy separations of 1D subband edges was first suggested in reference [146]. It should be noted that the appearance of odd-quantized plateaux was predicted in reference [145]; it turns out that this is a property of adiabatic constrictions only and is not expected in abrupt constrictions [144].

6.5.2 Measurement

The source-drain voltage was applied with the circuit in a constant-voltage configuration. The symmetry of the circuit with respect to DC bias was ensured by referencing V_g to half of the applied V^{sd} [137]. A schematic circuit diagram is presented in Appendix D, which includes a more detailed account of equipment wiring.

The usual quantities plotted for high quality data are the transconductance $\partial G/\partial V_g$ versus V_g for fixed V^{sd}. However, the device instability encountered in this work, and the particularly short plateau length made this approach unfeasible. Instead, data were plotted as a greyscale, with horizontal and vertical axes of V^{sd} and G respectively. The shade of grey was determined by $|\partial V_g/\partial G|$. A loss of information occurs because of the (unavoidable) elimination of the V_g axis.

Typically, data were taken over a 36 hour period incorporating as much averaging as possible, sweeping from large negative DC biases to large positive ones, or vice-versa. The taking of data with both signs of V^{sd} aided analysis by providing the eye with an axis of symmetry, and served as an important test for the reproducibility of faint features. A typical data set is plotted in Fig. 6.15, where plateaux are represented by the colour black and risers appear white. The contrast has been increased to highlight the black features of interest.

At $V^{sd} = 0$, there is a set of plateaux at poorly quantized conductances, because no account has been taken of the V_g-dependent series resistance. As $|V^{sd}|$ is increased, the plateaux disappear abruptly at approximately 50 μV and are replaced by fainter dark features which appear at conductances approximately mid-way between the 'even' quantized plateaux observed at $V^{sd} = 0$. As $|V^{sd}|$ increases further, these dark features drift to higher conductances and then vanish; no new structure is visible. The lack of perfect symmetry in the figure must arise from broken symmetries in the device. The obvious causes include differing source and drain ohmic-contact resistances, and the asymmetry in the lithographic gating pattern. Furthermore, the potential in and around the constriction is also affected by impurity configurations (which suffer no symmetry constraints).

6.5.3 Data analysis

The formalism for the interpretation of the source-drain bias data presented in Fig. 6.15 is now introduced. A typical experiment involves the measurement of G versus V_g for sequentially incremented V^{sd}. It should be noted that the confining potential is different at every different value of V_g. In principle, the

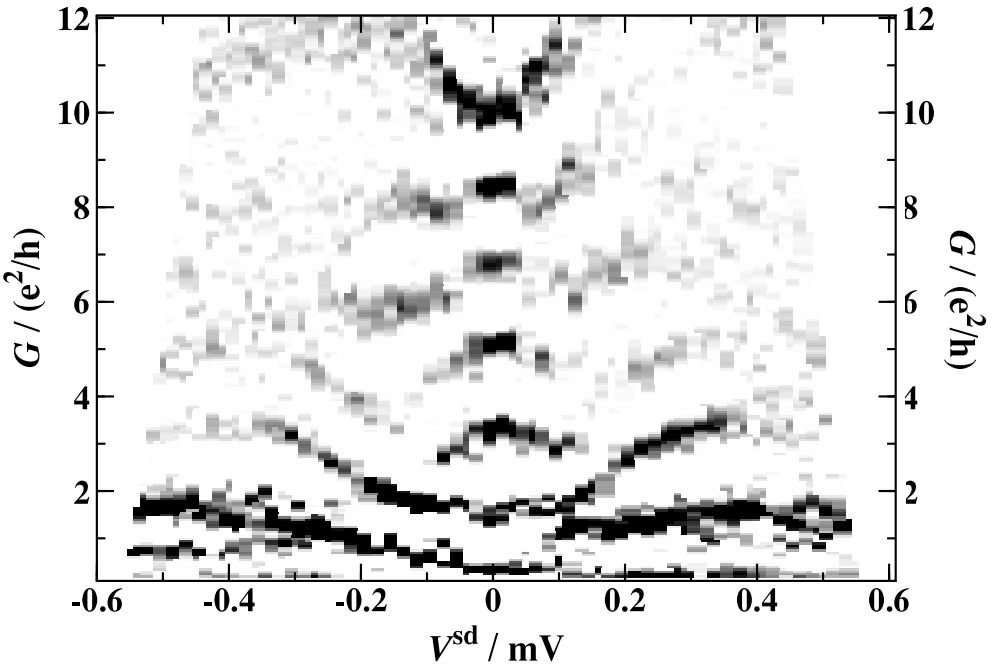

Figure 6.15: Differential conductance G versus total applied source-drain bias $V^{\rm sd}$, for device J9. The applied DC bias has been corrected for the constant contact resistance of the leads and ohmic contacts. Black regions represent 'plateaux'.

same is true of of $V^{\rm sd}$. However, it is assumed that the applied source-drain bias *does not* alter the electrostatics of the system.

At $V^{\rm sd} = 0$, it is assumed that there exists a set of two-fold degenerate 1D subbands occupied up to the chemical potential at each gate voltage. As $V_{\rm g}$ increases, the Fermi energy decreases and the changes in the confinement potential affect the energy separations of the 1D subband edges.

A measurement of energy spacings of the 1D subband edges is obtained by the introduction of the source-drain bias, which separates the two chemical potentials by an energy $eV^{\rm sd}$. These are swept through the range of confining potentials by pinching off the constriction; their simultaneous coincidence with the 1D subband edges at a particular $V_{\rm g}$ can be detected and hence yields their energy separation.

Equation 6.9 relates the differential conductance to the transmission coefficients of left- and right-going 1D subbands. The transmission coefficient of a generic 1D subband is unity if the electrochemical potential lies well above it and is zero if it lies well below. At intermediate chemical potentials, quantum mechanical (tunnelling) effects which depend on the nature of the confinement

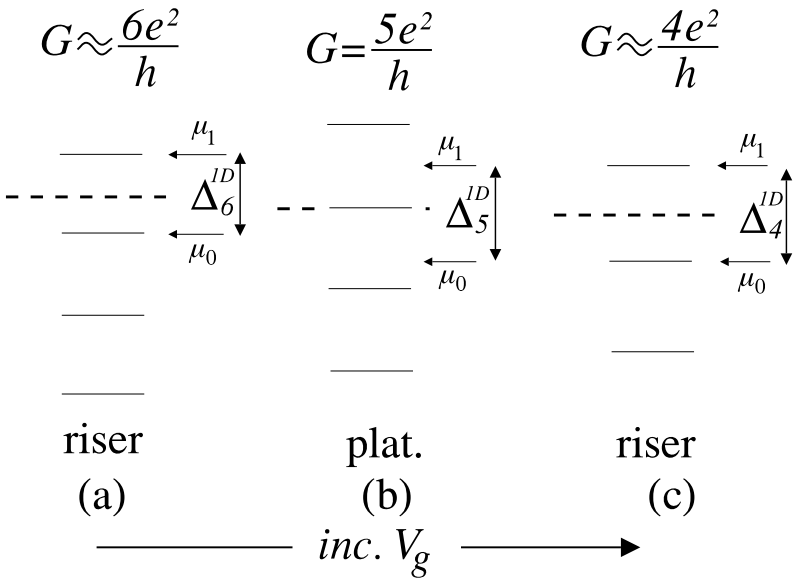

Figure 6.16: As $V_{\rm g}$ increases, μ decreases and the 1D subband spacing goes up. The applied source-drain bias $V^{\rm sd}$ required to obtain the most steep riser [(a),(c)], or the most flat plateau (b) gives the energy spacings between the 1D levels.

become important. The range of $V_{\rm g}$ over which the total transmission coefficient takes these constant values determines the plateaux length and visibility. A 'riser' corresponds to the range in $V_{\rm g}$ over which the transmission coefficient is varying strongly.

In the forthcoming analysis, these special values of the conductance are related to the relative positions of the left- and right-going chemical potentials, as depicted in Fig. 6.16. It has been assumed that the simultaneous coincidence of both μ_1 and μ_0 with the 1D subband edges leads to the most-steep riser (and therefore a light point in the greyscale). Figure 6.16(a) shows that the quantity $\mu_1 - \mu_0 = eV^{\rm sd}$ is equal to the energy spacing between the 1D subbands, denoted $\Delta_i^{\rm 1D}$. The index i, which in this case is even, denotes the (ideal) quantized conductance at $V^{\rm sd} = 0$ in multiples of e^2/h. Similarly, the dark points (plateaux) have been assumed to occur when μ_1 and μ_0 are positioned mid-way between different 1D subband edges (Fig. 6.16(b)). In this case, $\Delta_i^{\rm 1D}$ also represents the energy spacing of the 1D subband edges at this increased value of $V_{\rm g}$, and i is odd.

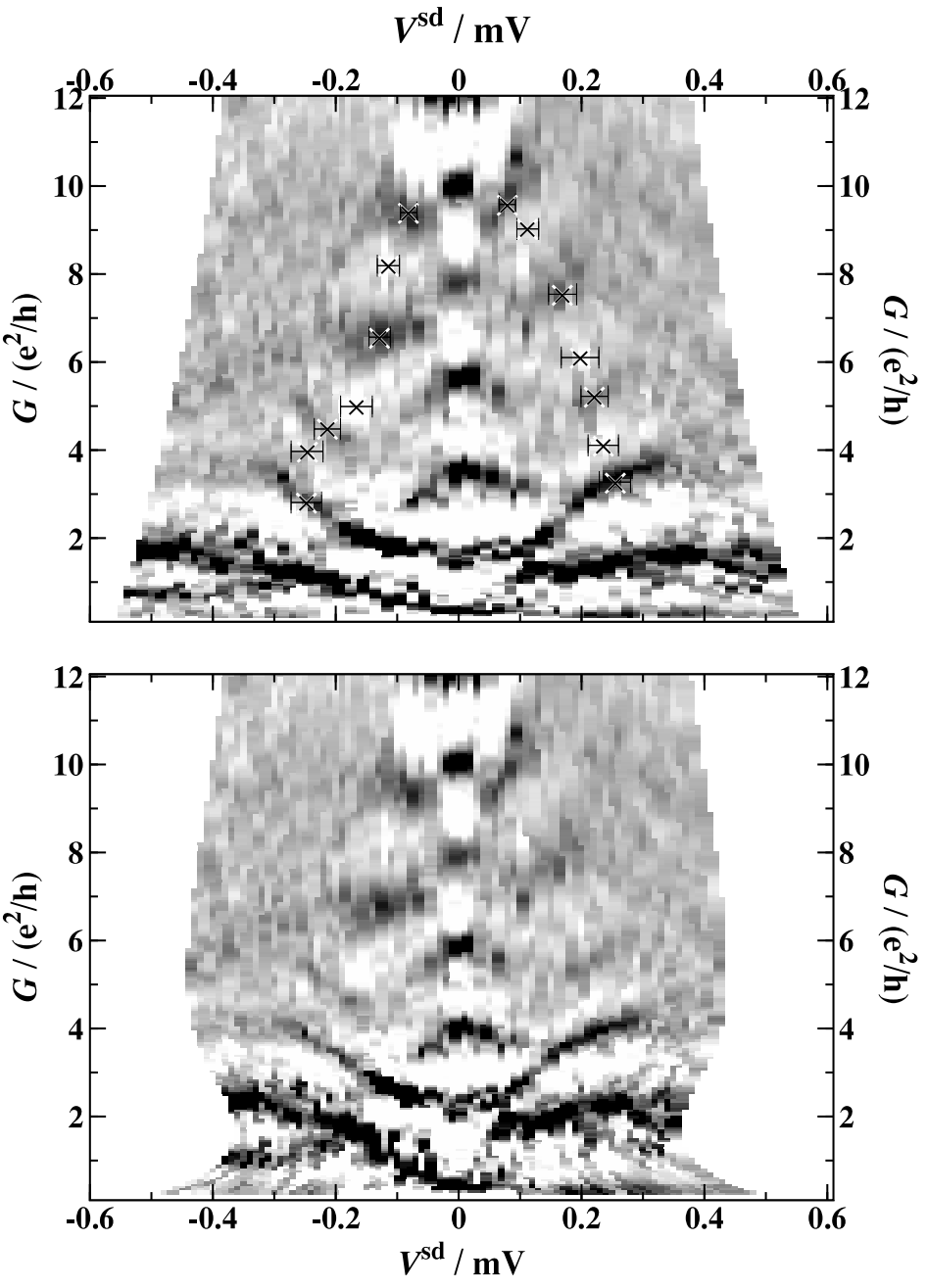

Figure 6.17: (a) Differential conductance G versus DC bias V^{sd}, for a constant series resistance correction of 1030 Ω. (b) Same as (a) but with the variable resistance correction.

6.5.4 1D subband energy spacing

Figure 6.17(a) shows the data from Fig. 6.15, corrected for a constant series resistance $R = R_0 = 1030\ \Omega$, which approximately quantizes all but the lowest-index plateau, whilst Fig. 6.17(b) gives the correction for the case in which R is a function used to fit the plateaux to their correct values. In comparison with Fig. 6.15, a lower contrast has been selected to provide more information. In (a), the most light and most dark points are marked with crosses. The biases $V_i^{\rm sd}$ of these points are plotted as the 1D subband spacings $\Delta_i^{\rm 1D} = eV_i^{\rm sd}$ against plateau index i in Fig. 6.18, using empty triangles. The other points (squares and filled triangles) in the diagram are the 1D subband energy spacings deduced from Figs. 6.15 and 6.17(b); they show the 1D subband energy spacings obtained using the other possible methods for the correction of the series resistance. Different subband energy spacings are measured because different amounts of the applied bias are dropped across the 1DS. The sizes

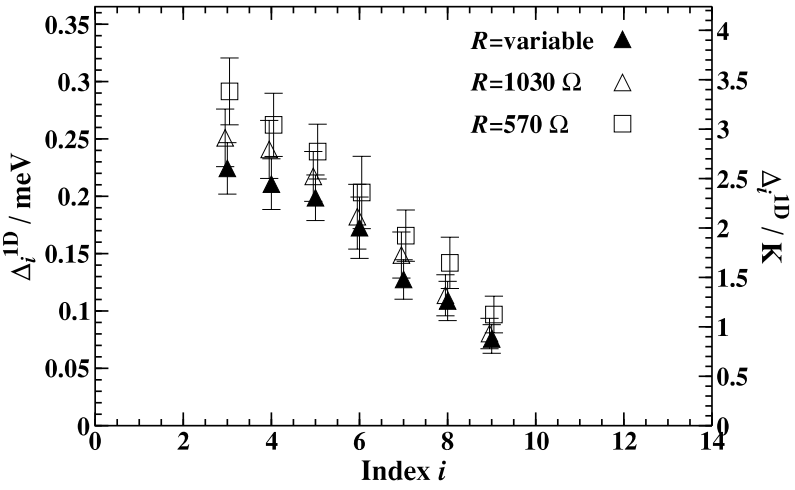

Figure 6.18: Energy separations of the edges of the 1D subbands plotted against index i, which indicates the conductance (in units of e^2/h) at which the measured gap is appropriate.

of the high-index energy gaps are in rough agreement with those estimated from the temperatures at which the plateaux are smeared (see Section 6.4.5). $\Delta_i^{\rm 1D}$ is found to increase strongly as the number of occupied 1D subbands decreases, which agrees with the temperature-dependence data. Furthermore, an increase is observed whatever the nature of the series resistance correction.

For completeness, comparison is made with results obtained from 1DESs fabricated from wafers of similar depth and carrier concentration. In these

very high quality devices, the 1D subband energy spacings near to pinch-off are found to approach 3.5 meV [137], which is an order of magnitude higher than the results obtained here. The reason for this difference is likely to be a combination of the greater effective mass of the particles in the 2DHS, and also the weaker confinement which occurs because of the lateral depletion effect. Between conductances of $10e^2/h$ and $2e^2/h$ the energy spacing is found to increase by a factor as high as two, in approximate agreement with the factor observed in this 1DHS.

Figure 6.18 represents the principal result of this chapter. It will be used in conjunction with magnetic field data obtained on the same cooldown to deduce 1D g factors of each subband. This topic forms the subject of the next chapter.

6.6 Summary and conclusions

This chapter began with a brief survey of the basic properties of 1DSs fabricated using split-gate technology. Then, a detailed account was provided of the problems encountered during the fabrication of the ballistic 1DHSs, and their novel solutions. Data were presented which demonstrated the properties of these constrictions at $B = 0$, including the best conductance quantization observed to date in the 1DHS. The plateaux were found to be only approximately quantized in even multiples of e^2/h. It was argued that this is most likely to have been due to the nature of the coupling between the 2D and 1D regions of the devices, resulting in a V_g-dependent series resistance. The evolution of the plateaux into spin-resolved reflected edge states by the application of a perpendicular magnetic field demonstrated that the plateaux observed at $B = 0$ are due to spin-degenerate ballistic quantization. Some of the greyscale and data-averaging techniques need to overcome sample instabilities were also described.

The most important data presented in this chapter concerned the first study of the effect of a DC source-drain bias on the 1DHS. The plateau quantization of device J9 was observed to change from even to roughly odd multiples of e^2/h, as a function of V^{sd}. This indicates that the entrance and exit of the constriction are close to adiabatic. From these observations, the 1D subband energy spacings were obtained using a method adapted from previous techniques used in higher quality 1DESs. It was found to increase from approximately 0.1 meV to 0.25 meV as the sample was pinched-off, which is in rough agreement with temperature-dependence data presented earlier in the chapter. These results are of crucial importance to Chapter 7.

Chapter 7

Parallel magnetic field studies of one-dimensional hole systems

7.1 Introduction

This chapter presents the results of experiments performed in a low parallel magnetic field on the 1DHSs described in Chapter 6. Following a simple description of the data, which show evidence for the crossing of the 1D subbands, a more careful consideration of the relevant processes is used to deduce the magnitude of the parallel g factors of the 1D subbands of the hole system. These are found to increase as the number of occupied subbands in the channel is reduced. The possible mechanisms, which include both mixing and interactions, are discussed in the last part of the chapter.

7.2 Application of a parallel B field

Three 1DHS devices (J9, J10 and J11) were studied in a magnetic field $B_{||}$ applied in the plane of the 2DHS, with the current flow (through the constriction) aligned perpendicular to the magnetic field (see Fig. 7.1). Data obtained are presented in Figs. 7.2(a) and (b) for devices J9 and J10 respectively. In each case, the magnetic field was oriented closer than 1° to the plane, so that at $B = 4$ T the perpendicular component of the field, $B_{\perp}$, was less than 0.1 T. The greyscales have been constructed as described in Chapter 6; black regions represent plateaux in the G vs $V_{\rm g}$ traces. At $B = 0$, plateaux are observed at even integer multiples of e^2/h. As the magnetic field is increased, the conductance changes from even integer to all integer and then to odd

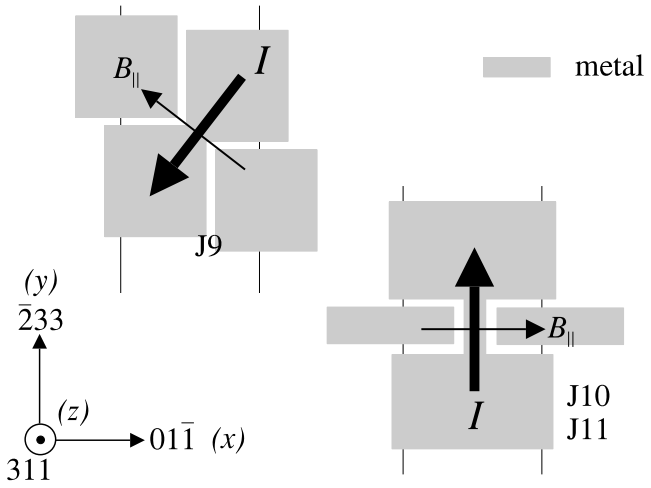

Figure 7.1: Schematic diagrams of the various devices, showing the orientations of the 1D constrictions studied with respect to the applied magnetic fields and the crystal axes.

integer quantization, between magnetic fields of 1 and 2 T. This changeover occurs at slightly lower fields when there are many occupied 1D subbands. At even higher fields, beyond approximately 4 T, the odd quantization becomes weaker. This high field regime is the subject of Chapter 8.

To elucidate the basic physics, it is assumed initially that: (i) the 1D subband edges in the constriction are two-fold degenerate at $B = 0$; (ii) the subbands have well defined spin; (iii) the g factors of all the subbands are the same, and are non-zero; (iv) diamagnetic effects are unimportant. These assumptions are relaxed, or justified, in later sections of this chapter.

The effect of $B_{||}$ is depicted schematically in Fig. 7.3, in which solid and dotted lines represent 1D subband edges of opposite spin. When $g\mu_B B_{||} = \Delta^{1D}$, the subbands cross for the first time.

The data in Fig. 7.2 may be explained using the idea of the crossing 1D subbands depicted in Fig. 7.3. When the chemical potential lies between 1D subband edges, the conductance is quantized at a value $i \times e^2/h$ where i is an integer which counts the number of spin-resolved 1D subband edges below the chemical potential. As V_g is decreased from the pinch-off voltage, the Fermi energy increases as carriers are introduced into the system. At zero magnetic field, the first two (opposite-spin) subbands are populated simultaneously; therefore G increases to $2e^2/h$ and further increases occur in pairs of degenerate subbands so that the conductance is quantized in even integral

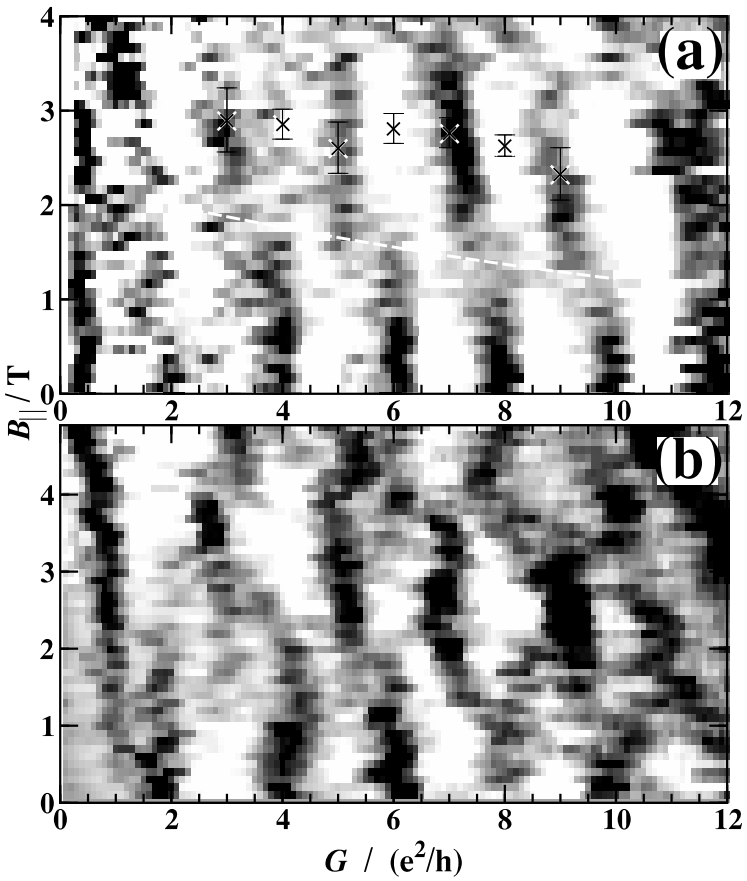

Figure 7.2: (a) Sample J9, showing a change in quantization (black) from even to odd as $B_{||}$ increases. (b) Similar behaviour at low field in sample J10.

multiples of e^2/h. When the spin degeneracy of the subbands is lifted at low $B_{||}$, all of the levels are resolved and the 1D subbands are populated separately; hence G takes all integer multiples of e^2/h. At the magnetic field of the crossings, an increase in the Fermi energy populates just one 1D subband edge, but further subbands are populated in pairs because of the accidental degeneracy introduced by the parallel magnetic field. In this regime, which is shaded in Fig. 7.3, the conductance takes values $1e^2/h, 3e^2/h, 5e^2/h$, giving the odd quantization observed in Fig. 7.2. As the magnetic field increases further the energy gaps at odd filling factor decrease, resulting in the weakening and eventual disappearance of the odd quantization.

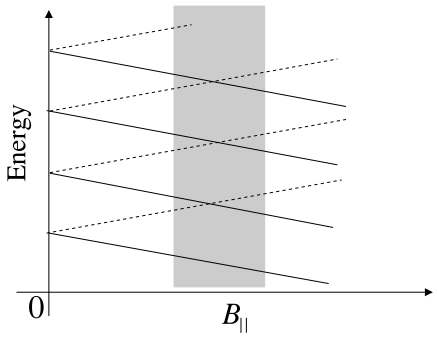

Figure 7.3: The Zeeman effect in 1D, due to a parallel magnetic field. The 1D subband edges of opposite 'spin' are represented using the solid and dashed lines. The regime in which odd quantization is expected is shaded.

7.3 Parallel g factors of the 1DHS

This section presents a deduction of the parallel g factors of the 1DHS from the measured energy spacings of the 1D subband edges and the magnetic fields at which the edges cross. Implicit in the calculations are the assumptions that the 1D subband edges are two-fold degenerate at zero magnetic field, and that the magnetic field affects the energies of the subbands linearly. These assumptions are discussed in detail in Section 7.4.

The parallel g factors of the 1DHS are determined from the data using two related methods. In the first technique (method 1), we utilize the set of parallel magnetic fields $\{B_i^{1D}\}$ at which the plateaux at $i \times e^2/h$ are most clearly resolved (i odd), or at which the risers between odd plateaux are most steep (i even). The subband energy spacings at the chemical potential, Δ_i^{1D}, are then used to calculate the 1D parallel g factors at the chemical potential,

$$g_i^{1D} = \frac{\Delta_i^{1D}}{\mu_B B_i^{1D}}. \tag{7.1}$$

The values of B_i^{1D} for J9 are marked with crosses in Fig. 7.2(a), and are assumed to correspond to the point at which the 1D subbands in the vicinity of the chemical potential cross.

The second technique (method 2) uses a lower magnetic field regime. The quantization of the conductance of the plateaux changes from even to odd between fields of 1 T and 2 T. This transitionary region is marked by the white dashed line in Fig. 7.2(a). This line has been determined by fitting

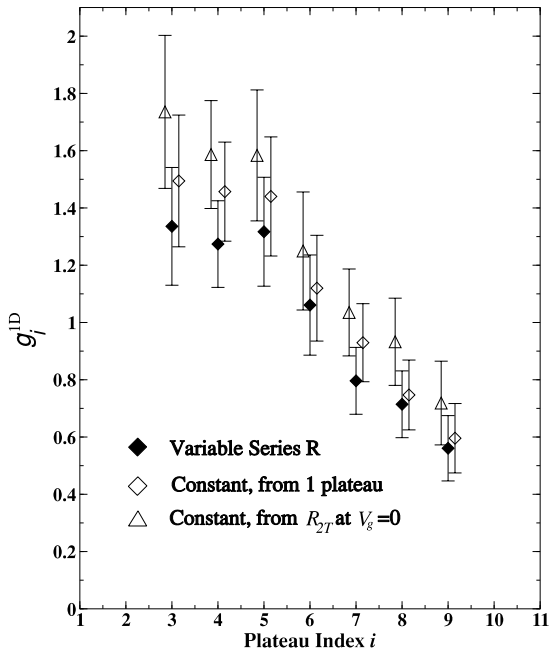

Figure 7.4: Parallel g factors of the 1D subbands of device J9, obtained at 70mK using method 1 for the extraction of $\{B_i^{1D}\}$, with the three different analyses of the 1D subband energy spacing (see Chapter 6).

a polynomial to the fields at which the dark and light features are of equal visibility. These points exist at $i + 1/2$. By interpolating to integer indices, and assuming that the levels are equally spaced at this point, new values of $B_i^{1D}/2$ are obtained. In conjunction with the Δ_i^{1D} extracted from the DC source-drain bias measurements, an alternative set $\{g_i^{1D}\}$ may be calculated.

Figure 7.4 plots g factors for device J9 on one cooldown, determined using method 1 discussed above. The three curves correspond to the three methods of series-resistance correction in the measurement of Δ_i^{1D} (see Section 6.5.4). The error bars plotted in Figs. 7.4 and 7.5 are determined from the errors in the estimation of B_i^{1D} and Δ_i^{1D}. These error bars are about 30%, and are insufficient to change the observed trends. It is more difficult to account for systematic errors. The most obvious one, which occurs in the determination of the actual DC bias across the constriction, has been shown to be of little qualitative importance because the three sets of points in Fig. 7.4 exhibit the same trend. Filled symbols in Fig. 7.5 show g factors obtained using method 1 for devices J9 (from Fig. 7.4) and J11. Empty symbols represent data obtained by method 2, for device J9 on two different cooldowns and for

device J11. The arrows show lower bounds obtained from device J10, which was destroyed before DC-bias measurements had been completed.

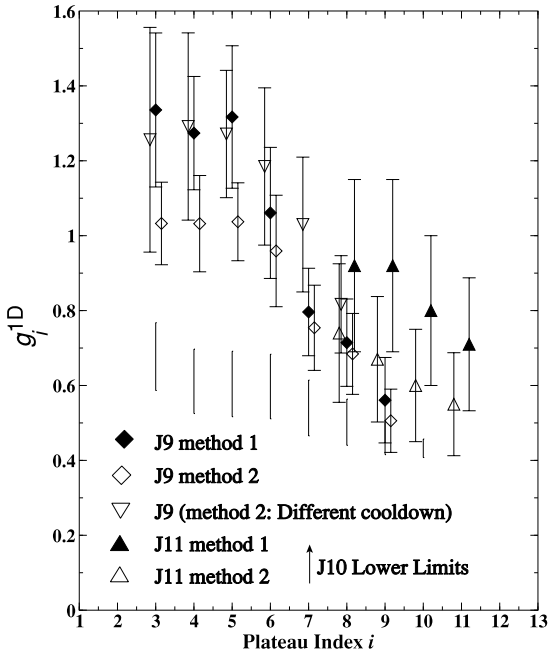

Figure 7.5: Parallel g factors obtained from various devices and cooldowns, using methods 1 and 2. The variable series-resistance correction has been employed.

The two methods of extraction of the B-data, and the three methods for the determination of the DC bias across the constriction, yield roughly consistent results: as the number of occupied 1D subbands is decreased by an increase in the side-gate voltage, the 1D parallel hole g factor increases, by a factor of approximately two over the experimentally accessible range.

7.3.1 Orientation errors

The orientation of the sample, which was varnished to the cold finger of a dilution refrigerator insert, differed from parallel by an angle of 0.7° (in the case of J9, cooldown 1). This was determined from the Hall voltage, which depends only on $B_\perp$ in a 2DS. At the Γ point of the Brillouin zone of a 2DHS, $g_{||}$ is predicted to be zero as discussed in Section 5.2.2. The possibility that the observations are strongly affected by $g_\perp$, which in the strongly anisotropic regime is large, is considered now (see also Section 5.2.5).

The experimental proof that the 1D subband crossings observed are not due to the 'stray' component of the magnetic field, $B_\perp$, lies in a comparison of

the reflected edge-state data (shown in Fig. 6.13) with the parallel-field data of Fig. 7.2. In the former case, $B_\perp$ did not cause spin splitting for fields less than 0.2 T. Furthermore, the quantization of G evolved from even-index plateaux to *all*-index plateaux; purely odd quantization was not observed. In the parallel-field data, $B_\perp$ never exceeds 0.1 T and a transition to odd quantization is observed. It is therefore clear that the observed behaviour is due to $B_{||}$.

7.4 Assumptions of the analysis

In addition to the Zeeman effect, the application of a magnetic field affects the levels diamagnetically, and at high fields there are self-consistent effects which arise from the long-range nature of the 1D density of states. These, and other, assumptions are discussed in this section.

7.4.1 Degeneracy at zero field

An important assumption of the analysis was that, at zero magnetic field, the 1D subbands of the hole system were two-fold degenerate. As described in Chapter 2, the two-fold degeneracy at a particular value of $k_{||}$ (at $B = 0$) arises from the invariance of the Hamiltonian to the space-inversion operation ($\mathbf{r} \rightarrow -\mathbf{r}$) [43]. If the crystal- and lateral-confinement potentials are inversion symmetric, then the 1D subbands must retain this two-fold degeneracy.

The T240 quantum well is close to symmetrically doped, and to a good approximation it may be assumed that the HH1 2D subband is two-fold degenerate at the 2D Fermi wavevector of the system. Furthermore, the 1DHS is created by the application of a voltage V_g to symmetrically patterned split-gate metal. Thus the lateral confinement potential is also inversion symmetric.

However, the large voltage V_g applied to the split gates is certain to break the inversion symmetry of the 2DHS directly beneath them. This is because the component of electric field perpendicular to the plane, E_z, far exceeds the voltages required to produce beating in the Shubnikov-de Haas oscillations (see Section 2.5). Although the 1DHS is defined *between* the split-gates (and not beneath them), it is possible that the stray component of E_z could cause measurable zero-field spin splitting in the split-gate devices.

Surprisingly however, the data presented in Figs. 6.9 and 6.13 indicate clearly that the plateaux *do* correspond to two-fold degenerate 1D subbands, because the number of plateaux is doubled by the application of $B_\perp$.

The observation of plateaux at conductances of $10e^2/h$ and $8e^2/h$, but not at $9e^2/h$ (at $B = 0$), implies that energy gaps of approximately $(\Delta_8^{\mathrm{1D}} + \Delta_{10}^{\mathrm{1D}})/2$ are detectable in this measurement. The measurements of these subband spacings presented in Chapter 6 imply therefore that the resolution of the experi-

ment is better than 50 μeV. This energy could be taken as an upper bound for any lifting of the degeneracy of the 1D subband edges at zero magnetic field. However, as the 1D subband energy spacing increases towards pinch off, the plateau quality does not improve commensurately. This could mean that the 'resolution' of the measurements decreases as V_g increases, possibly because of the drop in device stability.

7.4.2 Self-consistent behaviour

The density of states of a single 1D subband varies as $E^{-1/2}$ from the subband edge. Therefore the occupation of a 1D subband is limitless. Even when the chemical potential is located between 1D subband edges, and G is quantized, a small change in the positions of the subbands relative to μ will alter the number of carriers in the constriction. This should be contrasted with the quantum Hall effect in which, at integer filling factor, a small change in the positions of the Landau levels does not require a significant change in the 2D carrier concentration. This reflects the finite occupancy of each Landau level.

The parallel 1D g factors of the 1DHS were deduced by the application of a magnetic field, which was assumed to have moved the subband edges relative to the chemical potential. As argued above, this would have altered the number of carriers in the constriction, and could therefore have cost a large amount of electrostatic energy.

In fact, Hartree calculations for the 1DES [147] show that the system changes its self-consistent confinement potential by moving the electrostatic potential Φ_0 in Fig. 7.6(a) to keep the carrier concentration roughly constant. The energy difference $\mu - q\Phi_0$ is plotted (using dotted lines) as a function of $B_{||}$ for fixed carriers per unit length in Fig. 7.6(b). It exhibits cusps when subbands depopulate. However, these cusps may be expected to be smoothed by the finite lifetime of the particles. Although the 'oscillations' are most pronounced when there are few 1D subbands occupied, up to magnetic fields of the first crossing points the oscillation is rather small and the Fermi energy may be approximated by a horizontal line. These self-consistent processes are not expected to have affected the g factor measurements significantly.

7.4.3 Diamagnetic Shift

The parallel magnetic field applied also affects the energies of the 1D subbands diamagnetically; however, a theory of the properties of the 1DHS in a parallel magnetic field has not been published yet. Reference [148] presents calculations of the 2D valence band structure of (100)-grown symmetric quantum wells in parallel magnetic fields which show that $B_{||}$ changes the mixing of the

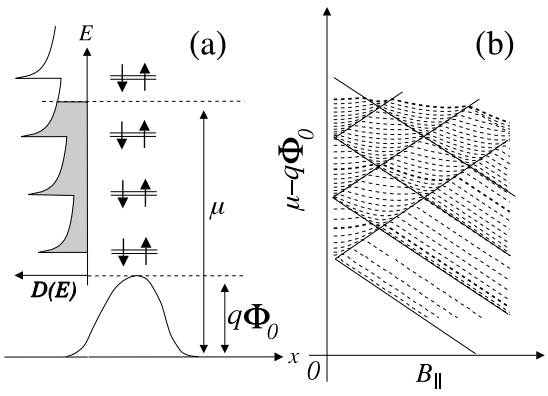

Figure 7.6: (a) A schematic diagram of the (two-fold degenerate) 1D subband edges formed at the saddle-point of the confinement potential. The 1D density of states is plotted on the left. (b) Contours of constant carriers per unit length (dotted lines) in the constriction, as a function of parallel magnetic field.

LH and HH subbands. It suggests that for a 120 Å quantum well subject to $B_{||} = 15$ T, crossings occur between LH and HH subbands for $k_{||} > 0.02$ Å^{-1}. The wider wells studied in this dissertation should be affected more strongly by $B_{||}$ because of the smaller 2D subband spacings, so strong $B_{||}$-induced mixing effects might be expected for parallel fields of less than 15 T.

In electron systems, there are three diamagnetic effects [149], depending on the experimental details: $B_{||}$ perpendicular to the current; $B_{||}$ parallel to the current; B perpendicular to the plane of confinement. The first of these orientations is relevant here (the latter orientation was discussed in Section 6.4.6).

In this case, the magnetic field provides extra confinement in the crystal growth direction but has no effect on the 1D confinement. The energy spacing of the 1D subbands is not changed to first order, but the zero of energy is shifted when the magnetic length associated with the applied field becomes smaller than the characteristic half-width of the z component of the wavefunction of the 2DHS. For T240, this occurs at fields of approximately 6 T. Such diamagnetic shifts have been observed in parallel field experiments in 1DESs [137], and do not become significant until fields of approximately this size. The deductions of the parallel g factors of the 1DHSs were made using parallel magnetic fields smaller than 4 T; this type of diamagnetic effect can be safely neglected.

7.5 Estimates of device parameters

A discussion of the possible mechanisms responsible for the observed enhancement of the 1D g factors requires estimates of the device properties. Although the calculations to be presented are crude, they provide order of magnitude estimates of such quantities as the numbers of particles in the 1DHS. It is assumed here that the effective mass of the 2DHS is approximately $0.25m_0$.

Provided that the number of carriers in the constriction is low, the confinement potential is approximately parabolic. The small number of 1D subbands observed in the J9, J10 and J11 devices indicates that this approximation should be valid. As a device is pinched-off by an increase in $V_{\rm g}$, both the Fermi energy and Φ_0 are expected to vary. Using the measurement $\Delta_9^{\rm 1D} = 0.09$ meV, the Fermi energy of the lowest energy 1D subband (see Fig. 7.6) at this gate voltage can be estimated crudely to be $4 \times 0.09 = 0.36$ meV. Similarly, $\Delta_3^{\rm 1D}$ corresponds to a Fermi energy of $1 \times 0.25 = 0.25$ meV. As expected this is lower than the previous result because of the increase in gate voltage, which depletes carriers from the constriction. The difference in energy, $\mu - q\Phi_0$, can be estimated by adding to the Fermi energies the quantity $\Delta_i^{\rm 1D}/2$, to account for the zero-point energy. The two-dimensional Fermi energy of the T240 2DHS is estimated to be approximately 1.7 meV (see Chapter 2), which indicates that $q\Phi_0$ must be very large. This suggests that 2DHS near to the constriction is rather depleted, and is probably related to the lateral depletion effects discussed in Chapter 6.

Approximate calculations, assuming that the confinement is parabolic, show that the width of the constriction at the chemical potential drops from about 0.4 μm to 0.1 μm as G falls from $9e^2/h$ to $3e^2/h$. Over the same range, the approximate total number of holes in the channel (which is assumed to be around 1 μm long) drops from 200 to about 30.

7.6 Discussion: mixing in 1D

7.6.1 Band structure of the 1DHS

The description and analysis of results presented in Chapter 6 neglected the peculiar properties of the valence band; it was implicitly assumed that the dispersion of holes for motion along the 1D wires was parabolic. This approach is partially justified at zero magnetic field because the theoretical treatments of the conductance quantization and DC source-drain bias are independent of the down-wire dispersions, because they originate from the cancellation of the 1D density of states and the group velocity (see Chapters 1 and 6).

However, in this chapter the 'spin' properties of the 1D subbands are ex-

amined; the spin-orbit coupling in the valence band, and its associated mixing of the angular-momentum characters of the subbands, may not be ignored. The starting point for this brief discussion is the 2D band structure described in detail in Chapter 2. At $k_{||} = 0$, the hole energy is quantized by the crystal confinement potential into decoupled ladders of HH and LH 2D subbands. The effect of a lateral confinement potential is to produce series of 1D subbands associated with each 2D subband. In general, they cannot be labelled $|J, M_J\rangle$ because of the reduction in symmetry of the system, even for down-wire wavevectors of $k_{||}^{1D} = 0$. **k.p** calculations of the valence band in 1D systems [150, 151, 152] show that as $k_{||}^{1D}$ increases from zero, a set of highly non-parabolic 1D subbands are formed, and in principle the mixture of $|J, M_J\rangle$ states in each 1D subband is different.

7.6.2 Variation of mixing with V_g

The g factors plotted in Figs. 7.4 and 7.5 were obtained at different gate voltages, Fermi energies, and magnetic fields. Each g factor therefore originates from a different confinement potential. In principle, the measured enhancement of the 1D in-plane g factor could be explained by increased HH-LH mixing as V_g is increased.

Calculations described in Chapter 2 indicate that appreciable mixing does occur, in this particular system, between the three lowest energy 2D subbands which are HH1, HH2 and LH1, in order of increasing hole energy (see Fig. 2.2(a)). This implies that, at our 2D Fermi wavevector k_F, the 2D parallel hole g factor should be non-zero (in the limit of vanishing magnetic field). It is not apparent from the data whether in the 2D limit, which is approached as the plateau index $i \to \infty$, the g factor will reach zero. It is possible to set an upper bound $g_\infty^{1D} = g_{||} < 0.65 \pm 0.2$. This should be compared with $g_{||} = 0.95 \pm 0.05$ obtained from the 2D tilted-field measurements described in Chapters 4 and 5. The latter result, which was obtained at $\nu = 4$ and agreed with data at $\nu = 5$, was measured in a strong perpendicular magnetic field which causes extra mixing of LH and HH states. It is therefore not surprising that the 2D result yields a larger parallel g factor. However, these comparisons must be viewed with caution as it has not been shown that the signs of the 1D and 2D g factors are the same.

We turn now to the measured increase of g_i^{1D} as i decreases. The **k.p** calculations (mentioned above) of the valence-band 1DS has concentrated on wires in which the characteristic confinement lengths, λ_z and λ_x, are comparable. In this case, the 1D subbands obtained bear little resemblance to the 2D subbands of the host 2DS; the dominant direction in the system is now the wire axis and not the crystal growth direction. However, the simple argu-

ments presented in Section 7.5 indicate that $\lambda_x > 0.1$ μm in this experiment. In contrast, the quantum-well width gives $\lambda_z = 0.02$ μm.

In this 'quasi-2D' limit the non-interacting **k.p** theories predict sets of 1D subbands which reflect the 2D subband from which they are derived [150] (until the 1D subbands from adjacent 2D subbands start to interact). The source-drain bias measurements of Chapter 6 indicate that the 1D subband energy spacings are always less than 0.3 meV, which is an order of magnitude less than the 2D subband spacing. This is equivalent to stating that the well width is much smaller than the 1D constriction width, even near to pinch off. Thus, all of the 1D subbands probed exist very near to the 2D subband from which they derived, and it appears unlikely that they should contain strongly differing mixtures of HH and LH states. Hence it is not thought that the increase in g_i^{1D} is likely to be due to changes in the spin-components of the 1D subbands.

Furthermore, we attach little importance to mixing by the parallel magnetic fields applied in these measurements, because the g factors calculated by the two methods described earlier yield roughly consistent results despite the fact that they utilize information at strongly different magnetic fields. This observation also justifies the neglect of the diamagnetic and self-consistent effects described earlier.

7.7 Discussion: interactions in 1D

7.7.1 Summary of theory

Some of the theory of interactions in 2D has been described in Chapter 3. In this section, arguments are presented which indicate that interactions are very important in the 1DS too.

The large hole effective mass and reduced dimensionality point to an enhanced importance of exchange energies (relative to the kinetic energy). Defining the number of carriers per unit length in the constriction to be n^{1D}, r_S in one dimension can be shown to be $1/(2n^{1D}a_0^*)$. It takes values between two and seven as the device is pinched off, using the estimates of sample parameters described in Section 7.5. It should be borne in mind that, in contrast to the cases of two and three dimensions (equations 3.4 in Chapter 3), exchange energies in 1D are a function of both r_S and also a wire width parameter [70].

The total interaction energy per particle, E^{1D}, is the sum of the Hartree, exchange and correlation energies [69, 153]

$$E^{1D} = E_H^{1D} + E_X^{1D} + E_{cr}^{1D}. \tag{7.2}$$

The effects of exchange in an infinite quasi-one-dimensional wire formed from an ideally thin 2DES by the application of a parabolic potential, have been studied by Wang *et al.* [154] using density-functional theory.

The primary results of the calculation may be summarised as follows: (i) there exists a large energy gap whenever the number of occupied 1D subbands is an odd integer, which arises not from the Zeeman term but the exchange interaction; (ii) these energy gaps increase as the number of occupied subbands decreases; (iii) at the lowest densities, the system is magnetized at $B = 0$.

Thus, the effects of the exchange energy in a 1DS at zero magnetic field bear similarities to the properties of the 2DS in a strong perpendicular magnetic field. In the former case, the quantization is provided by the lateral confinement potential, whereas in the latter case the system is quantized into Landau levels. The excitation gaps and ground state of the system depend strongly on its spin properties, via the exchange interaction.

The instability to spin-polarization at zero magnetic field in the 1DS is analogous to the magnetization instability that occurs in the 2DS (see Chapters 3 and 5). However, the inconvenient nature of the density of states in 1D prevents the description of these exchange effects in terms of simple coefficients such as A_{ij}.

According to Wang *et al.*, the apparent enhancement of the spin-gaps is strongest at odd integers; if this were represented as a g factor, oscillations would be observed. The experimental data for the 1DES, however, do not exhibit oscillations. There is also disagreement in the magnitude of the effects, which are predicted to be much larger than the experimental observations. Wang *et al.* discuss the possibility that correlation effects might explain the discrepancies. However, they argue that correlations ought to be small in the 'device' they considered.

Correlation (and exchange) energies in 1D have been investigated theoretically [69, 153], for an infinite cylindrical 1D wire with up to two occupied 1D subbands. The pertinent results were that, for wide wires, correlation energies are at least an order of magnitude smaller than exchange energies. The calculations were performed assuming that $E_H^{1D} = 0$; this approximation assumes that the interaction of the particles with a dopant background introduces a term of equal magnitude and opposite sign to the direct Coulomb term. This clearly cannot hold generally for devices in which gate voltages are swept. In a subsequent paper [155], the same authors also discuss spin-polarization instability at zero magnetic field and find that theories including correlations do predict their occurrence in one dimension.

7.7.2 Application to data

In this subsection, we discuss the possibility that the measured enhancement of g_i^{1D} as i decreases is due to exchange interactions.

In the activation-energy measurements presented in Chapters 4 and 5, the property of the 2DHS being probed was the single-particle excitation energy Δ_ν. This contained contributions from a non-interacting energy and the exchange interaction. The latter energy depended only on $B_\perp$; hence to describe the g factor as enhanced was mis-informative, because the 'real' g factor $\partial\Delta_\nu/\partial B$ (for constant $B_\perp$) remained at its non-interacting value.

In the 1D experiment described here, there are no energy gaps at the chemical potential because of the long-ranged nature of the 1D density of states. Hence in contrast to the 2D case, in 1D exchange might be expected to affect the 'real' g factors defined in terms of the partial derivative above.

The data presented in Fig. 7.5 have large error bars, and there are relatively few points. No clear oscillation of g_i^{1D} is discernible, which agrees with the data for 1DESs presented in reference [156] (to be discussed below) but contradicts the predictions of Wang *et al.*, discussed in the previous section. However that calculation did not take any account of effects which might have blurred the measurements, such as the limited lifetime of the quasiparticles due to interactions and disorder.

According to reference [153], and assuming that their width parameter (which is the radius of the 1D subband wavefunction) $b = 1/2 \times \sqrt{\lambda_x \lambda_z}$, it is predicted that the exchange energy per particle in the lowest subband of our 1DS is about 1 meV. This is significantly larger than the Fermi energy in the constriction, and shows that the device under consideration cannot be modelled accurately using standard techniques. Nevertheless, it shows also that the single-particle picture is strongly modified. This energy is probably strongly reduced by screening and the effects of disorder in the constriction.

Since exchange interactions increase in importance as a system becomes increasingly one dimensional, it seems likely that the increased coupling between the Coulomb interaction energy and the 'spin' of the hole system towards pinch-off can explain the observed enhancement.

7.7.3 Comparison with 1DESs

The first observations of enhanced g factors in one dimension were described in reference [157], which reported a measurement of $|g^{1D}| \approx 1$ for the two lowest energy subbands of a split-gate device made from a GaAs/AlGaAs 2DES. More recent studies of very high quality 1DESs have been reported by Thomas *et al.* [137, 156]. In these experiments, the g factors were obtained

using a combination of DC source-drain bias and parallel magnetic field measurements. However, the superior stability of 1DESs enabled the use of a more sensitive technique using the gate voltage axis as a reference. The crossing of 1D subbands was not observed for the lowest subbands because of the large 1D subband energy spacing of the 1DES.

The magnitudes of the g factors were found to increase from 0.4 in the 2D limit (which was reached because of very high device quality) to about 1.2 for the lowest subband. It was suggested that electron-electron interactions were responsible for this increase. In the absence of a strong spin-orbit effect in the conduction band of GaAs/AlGaAs two-dimensional systems, and with other data presented suggesting possible spin-polarization in the last subband, this seems a likely explanation.

The similarity of the sizes of the g factors of the electron and hole systems in the 1D limit is probably coincidental. Nevertheless, the increases observed are probably fundamentally related.

7.8 Conclusions

This chapter has described measurements of the effect of a parallel magnetic field on the conductance quantization of 1DHSs. Three split-gate devices exhibited characteristic changes in their conductance which were attributed to the crossing of the 1D subband edges. This occurred at low magnetic fields, because of large g factors and small subband energy spacings of the 1DHS.

A set of parallel 1D g factors $\{g_i^{1D}\}$ were defined in terms of the magnetic fields at which the 1D subbands appeared to cross, using measurements of the 1D subband energy spacings at zero magnetic field. The technique provided the magnitudes but not the sign of the g factors, which were found to increase by a factor of approximately two as the number of occupied 1D subbands in the constriction decreased. The results for high index provided an upper bound on the 2D parallel g factor, $g_{||} < 0.65 \pm 0.2$, which was compared with the tilted-field measurements performed in a strong perpendicular field (see Chapter 5).

The possibility that the enhancement, as the system became more one dimensional, was due to changes in the HH and LH components of the 1D subbands was discussed. However, it was argued that this appeared not to explain the observations because of the 2D nature of the 1D subbands (in terms of mixing).

Finally, the possibility that the observed enhancement of the g factors could be attributed to exchange interactions in one dimension was considered. It turns out that the reduction of dimensionality does increase the importance

of exchange. However, the theory is of limited use in the 1DHS, and also predicts an oscillatory enhancement of g factors which favours odd indices. This has not been observed either in this experiment, or in experiments on similar electron systems.

Chapter 8

1DHSs in strong in-plane magnetic fields

8.1 Introduction

Chapter 7 described the determination of the 1D parallel g factors of 1DHSs, using a combination of measurements of the 1D subband energy spacings (Chapter 6) and the parallel magnetic fields required to cross the subbands. In this brief chapter, the effect of increasing $B_{||}$ even further is presented. It is shown that the pattern of conductance features can generally be explained using the ideas of multiple subband crossing.

8.2 High $B_{||}$ data

8.2.1 Experimental data

Figure 8.1 shows data obtained from sample J9, on a cooldown in which $B_{||}$ was aligned at 45° to the current flowing through the constriction. A constant series-resistance correction has been applied to the data.

As the applied magnetic field increases, the component $B_{\perp}$ which arises from orientation errors increases proportionally. The high magnetic fields to which these measurements extend emphasize any orientation errors of the 2DHS to the magnetic field. For this reason, $B_{\perp}$ has been included in Figs. 8.1 and 8.2 on the right-hand vertical axes. An important consequence of an orientation error $\delta\theta$ is the effect of $B_{\perp}$ on the confinement of the holes, and the subsequent transition to the quantum Hall effect discussed in Section 6.4.6. Examination of Fig. 6.13 shows that for $B_{\perp} < 0.1$ T, there is no apparent effect on the G versus V_{g} traces. Therefore the condition that 'reflected edge-state' effects do not become important, for a typical $\delta\theta = 1°$, is $B < 5.7$ T.

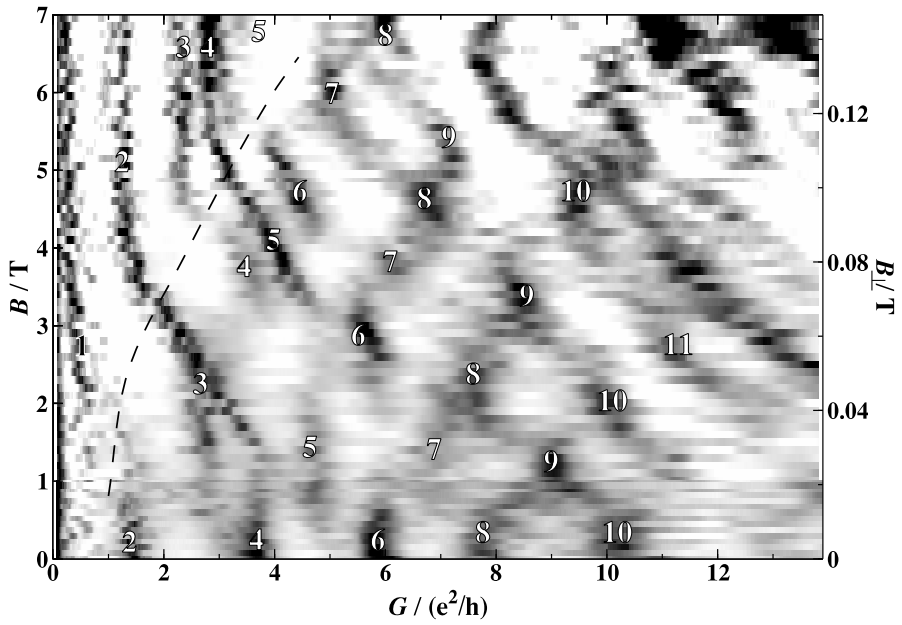

Figure 8.1: Data obtained on a cooldown of device J9, in which $B_{||}$ was oriented approximately 45° to I. Black regions represent plateaux in the G versus $V_{\rm g}$ traces. See the text for details.

As usual, black regions of Fig. 8.1 correspond to plateaux in the G versus $V_{\rm g}$ traces. At $B = 0$, they occur at approximately even integer multiples of e^2/h. As $B_{||}$ is increased, a transition is observed to odd integer quantization; these features are strongest in the range 1.5 T to 2.5 T, and have been marked with integers to denote their supposed ideal conductances in units of e^2/h. Similar behaviour was observed at low $B_{||}$ in the measurements presented in Fig. 7.2, and was explained by the crossing of 1D subbands due to a Zeeman energy.

However, the magnetic fields $B_i^{\rm 1D}$, at which the odd plateaux are most clear, differ between the two experiments and are lower in the case of Fig. 8.1 (for the same sample). It is generally true for small structures that the same device can exhibit slightly different characteristics on different cooldowns, especially if the rate of cooling (between 300 K and less than 4 K) differs significantly. Indeed, these two experiments were performed on different cryostats. Hence it is possible that, for example, the 1D subband energy spacings were smaller in case of Fig. 8.1. Another possible explanation of this discrepancy is the differing orientations of the current flowing through the constriction with respect to the applied magnetic field, which certainly would result in different

diamagnetic effects. A final possibility is that the parallel g factor of the 1DS is strongly anisotropic in the plane of confinement; such 1D anisotropies have been measured optically in arrays of very narrow 1DESs [158].

Figure 8.2 shows more data, obtained from sample J10; in this case $B_{||}$ was aligned at 90° to I. This data set is composed of single sweeps, and has

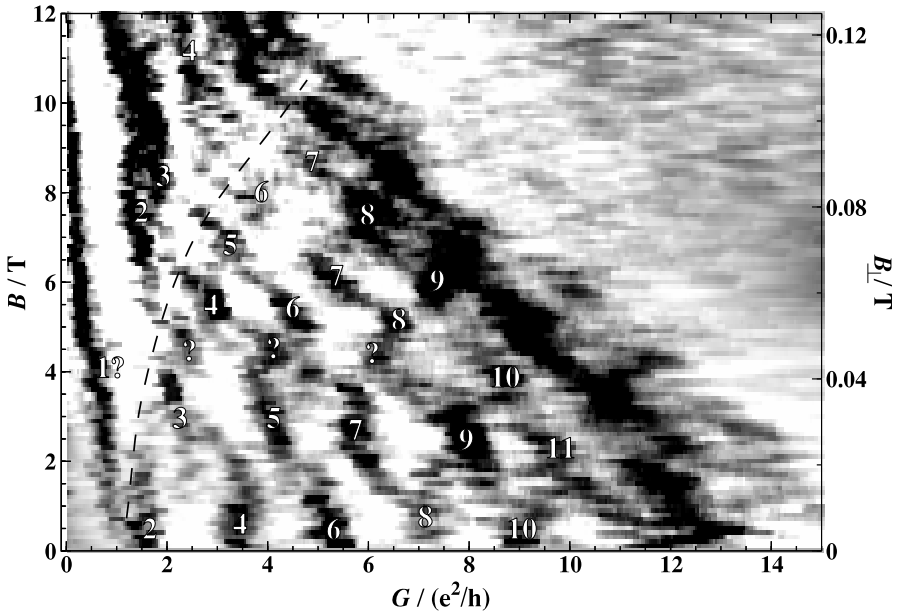

Figure 8.2: Data obtained from device J10, with $B_{||}$ oriented at 90° to I. Black regions represent plateaux in the G versus V_g traces.

therefore not been averaged.

8.2.2 Discussion

The features at higher $B_{||}$ in Figs. 8.1 and 8.2 may be explained qualitatively within a scheme of multiple subband crossings, which are depicted schematically in Figs. 8.3(a) and (b). At the magnetic field of the first crossing, the conductance of the device increases from zero in odd multiples of e^2/h. At the second crossing field, the two lowest energy 1D subbands are of the same spin. As the Fermi energy is increased from pinch-off (by a reduction in V_g), these subbands are occupied first and the conductance takes the values e^2/h and $2 \times e^2/h$. At this point, the system is completely polarized with a large magnetic moment. With further increases in the Fermi energy, the conductance takes *even* integral multiples of e^2/h.

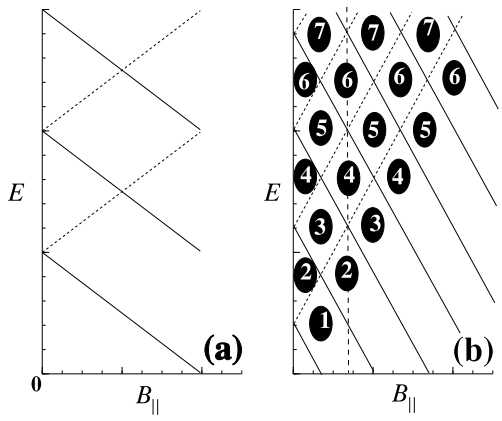

Figure 8.3: (a) Schematic diagram of the 1D subband edges in a parallel magnetic field. Opposite spin subbands are distinguished by the solid and dotted lines. (b) Same as (a), but for a larger $B_{||}$ range. The subband edges cross repeatedly, and the total magnetization of the system (for a fixed number of occupied subbands) increases. The numbers represent the conductance of the device in units of e^2/h.

At each subsequent crossing field, the number of same-spin 1D subbands which are sequentially occupied as V_g is decreased from pinch-off increases by one. Thus, after many crossings, a situation is predicted in which many same-spin 1D subbands can exist below the chemical potential and the system is very strongly magnetized.

White integers superimposed on Figs. 8.1 and 8.2 are positioned using this 'multiple subband-crossing' model of the device. The 'rule' for assignment is that, starting from $B = 0$, it should be possible to move diagonally upwards along lines of sequentially increasing indices and diagonally downwards with decreasing indices. Inspection of the J9 data shows that this rule is quite successful, although at higher magnetic fields the indices do not agree well with the measured conductances of the device. It seems likely that this is because of a changing series resistance, for which we have not corrected. In the case of device J10, the assignment is more problematic because of the extra set of features at approximately 4.5 T (marked by the question marks). If these were counted as ordinary plateaux, extraordinary curvature would be introduced into the labelling scheme. It proved impossible to retake the data more carefully because the device was destroyed by a power cut which occurred during a thunder storm. Nevertheless, both devices show that the 1D subbands crossed as many as four times.

An overall trend clear in Fig. 8.2 is the featureless region at high conductance and high magnetic field. It occurs partly because of an increase in the

contact resistance as $B_{||}$ increases, and partly because of the addition of the Hall resistance (due to $B_{\perp}$) to the two-terminal resistance of the device.

8.2.3 Strong $B_{\perp}$ and $B_{||}$.

On a further cooldown of device J9, in which I was perpendicular to $B_{||}$, the total magnetic field was found to be mis-oriented (with respect to the plane of the 2DHS) by approximately 8°. This offered an opportunity to study the conductance of the device in simultaneously strong parallel and perpendicular magnetic fields. The data are presented in Fig. 8.4, with B and $B_{\perp}$ plotted on the left- and right-hand abscissae. This data set exhibits strong quantum

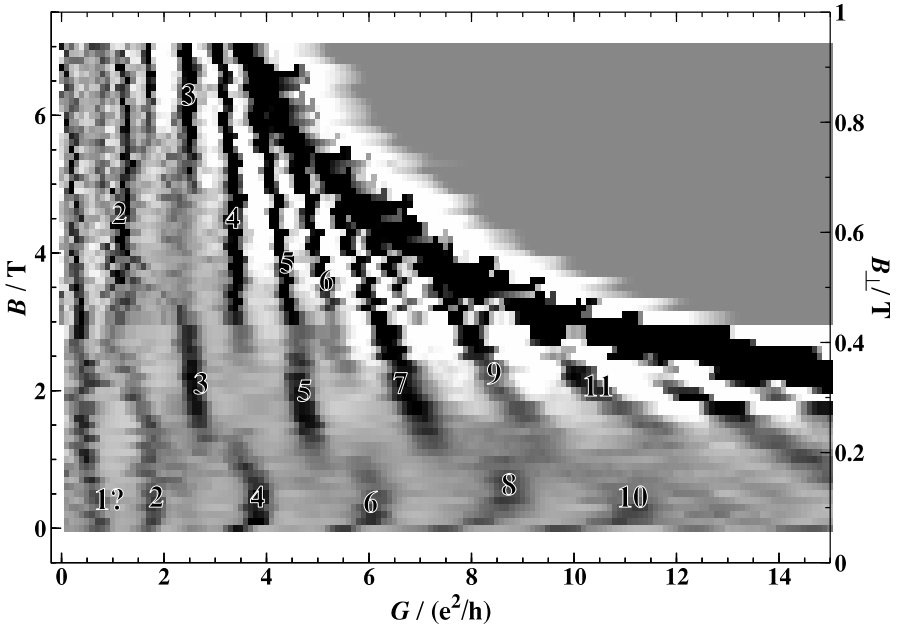

Figure 8.4: Data obtained from sample J9, with $B_{||}$ aligned perpendicular to I. The angle between the plane of the 2DHS and B is approximately 8° from parallel.

Hall effect features. Starting at $B = 0$, there are some roughly quantized plateaux at even multiples of e^2/h. In contrast to previous cooldowns, there is also a feature at approximately $1 \times e^2/h$. There is the temptation to argue that this plateau demonstrates spin-polarization in the lowest 1D subband at $B = 0$. However, its lack of reproducibility on other cooldowns favours its interpretation as an impurity effect.

As B increases, there is an increase in the conductance of the plateaux with indices four, six, eight and ten. This effect was also observed in the

data obtained in a purely perpendicular magnetic field (Fig. 6.13). The data presented in the purely parallel magnetic field are not affected in this way. This supports the theory that the change occurs as $B_\perp$ changes the coupling between 2D and 1D channels.

The conductance then exhibits a transition to odd quantization. The clarity of the plateaux also improves, as the extra confinement due to ω_C becomes important. It is revealing to examine a constant conductance feature. In the data of figures 8.1 and 8.2, a plateau with (for example) index 6 alternately appears and disappears as $B_{||}$ increases. This behaviour reflects the repeated crossing of the 1D subbands, as depicted in Fig. 8.3. Ultimately however, the plateau is expected to be visible independent of B when there are six lowest-energy same-spin 1D subbands. In contrast, in Fig. 8.4, the black regions with index 4 and 6 disappear only one time; once the odd plateaux with indices 5 and 7 appear, they do not disappear again.

These features can be explained in terms of a cross over from 1D electric subbands dominated by the Zeeman effect, to magnetic subbands (i.e. Landau levels) dominated by the cyclotron energy. To show the possible effects, it is convenient to consider a very simple quasi-1D system in which the 1D subbands are formed by harmonic confinement, and the g factor is isotropic and the same for each subband. Then, the energy of a particular subband edge may be written as [15]

$$E = \hbar\sqrt{\omega_x^2 + \omega_c^2} + g\mu_B \mathbf{B}.\hat{\mathbf{s}}. \tag{8.1}$$

The dispersions of ten spin-resolved subbands are plotted in Figs. 8.5(a)-(d) for a range of increasing tilt angles. The two spin species are represented by the solid and dashed lines. Note that in contrast to the tilted field measurements of Chapter 4, θ represents the angle between B and the plane (not the angle between B and the normal to the plane).

It must be borne in mind that the experimental data of Fig. 8.4 were obtained from a whole set of these diagrams (but at one fixed angle), corresponding to different gate voltages.

In Fig. 8.5(a), which corresponds to the perfectly parallel case, the conductance is expected to alternate between even and odd quantization. However, as the tilt-angle increases (b-d), the crossings at higher B cease to occur as $\hbar\omega_C$ (which affects each subband identically) separates the subbands. Hence, depending on the angle, the 1D subbands may never cross (Fig. 6.13), cross just once or twice (Fig. 8.4), or cross many times (Figs. 8.1 and 8.2).

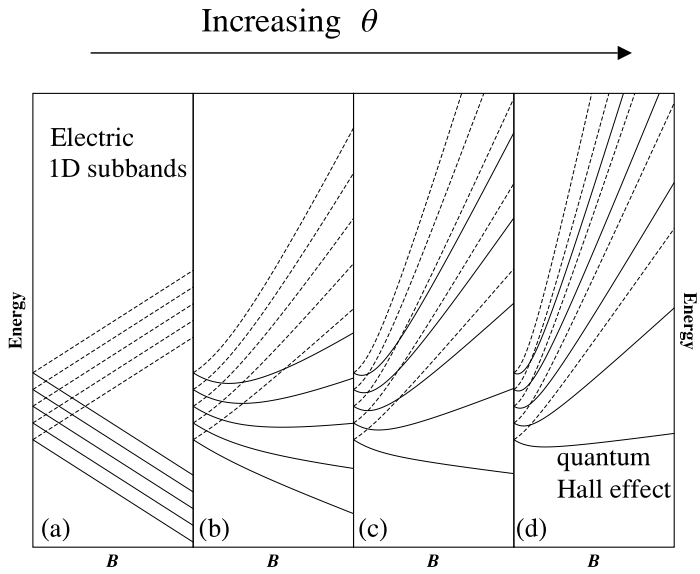

Figure 8.5: (a)-(d) Schematic diagrams of the effect of the magnetic field on a sample for increasing tilt angles. At low fields, the confinement potential is important and the Zeeman effect dominates. At high fields, Landau levels are obtained. The cross-over occurs at lower B as the tilt angle increases. The up and down spin projections are represented by solid and dashed lines.

8.2.4 Exchange effects in 1D

In Chapters 4 and 3 it was argued that when Landau levels approach each other, a first-order phase transition in which particles transferred between the Landau levels can occur. The transition is driven by the fact that an increase in the magnetization of the system lowers its interaction energy through the exchange mechanism. In 1D, the application of $B_{||}$ brings together opposite-spin 1D subbands so an analogous phase transition might be expected to occur.

If a process analogous to the 2D phase transition were to take place, the 1D subband edges would fail to cross. This would result in certain index plateaux weakening but not disappearing totally, and then strengthening, as a function of $B_{||}$. Of course, such an observation could also be explained in an anticrossing picture; as for the 2D case described in Chapter 5, it would be problematic to distinguish between the two mechanisms. Figures 8.1 and 8.2 are surprisingly well described by the simple non-interacting electron-like theory outlined previously; there is no clear evidence of anticrossing.

However, as discussed in Section 7.7, there are important differences between the densities of states of the 2D and 1D systems. It is therefore not clear

whether, as a function of $B_{||}$, a re-ordering of the occupied 1D subbands would occur discontinuously. An exchange-driven phase-transition may occur in 1D, but it need not be first order. In this case, there would be no anticrossing; but the magnetic fields at which the subbands crossed might not be explained by the simple non-interacting theory employed previously. Without devices of higher stability, which would allow the use of gate-voltage information, it is not possible to suggest that features of Figs. 8.1 and 8.2 can be attributed to these speculative phase transitions.

Finally, it is remarked that the exchange interaction may be expected to have a strong effect on the single-particle excitations of the system when it is strongly magnetized. This occurs after many crossings of the 1D subbands (see Section 8.2.2). The boundaries between the totally and partially magnetized regions of the data are marked using the thick dotted lines in Fig. 8.1 and 8.2.

8.3 Summary

This chapter has described the multiple crossing of the 1D subbands of constrictions subjected to strong parallel magnetic fields. The measured pattern of the conductance quantization was observed to change from even to odd, or vice-versa, each time the subbands crossed. Furthermore, a sample tilted away from parallel exhibited a cross-over from a region at low B dominated by the Zeeman effect to a region at higher B in which Landau level effects became important. This chapter also included some speculation about the exchange interaction. However, it did not appear to be manifested clearly in the data because of the poor device quality and the very small energy gaps under investigation.

Chapter 9

Conclusions and suggestions for further work

9.1 Introduction

In this chapter the main conclusions of this thesis are described and suggestions are made for further work. Before the specific conclusions of this research are detailed, attention is drawn to the physical themes common to most of this work.

In both the two and one dimensional devices studied, the motion of the holes in the [311] crystallographic direction of the GaAs/AlGaAs heterostructures was limited to a region of size 200 Å in width. In both types of device extra quantization was introduced by the application either of a magnetic field in the [311] direction ($B_\perp$), or an electrostatic confinement potential in the plane perpendicular to [311]. In the latter case, the confinement potential was rather weak, and a series of closely spaced 1D subbands was formed which are thought to have had many of the 'spin' properties of the parent 2D HH1 subband. In contrast, the confinement by the magnetic field created Landau levels with energy spacings less than an order of magnitude smaller than the 2D subband spacing; the result was extra mixing of the 'spin' components of the Landau levels.

Both types of experiments then investigated the response of the Landau or one-dimensional quantization to the application of a magnetic field applied parallel to the plane of the 2DS; in both cases levels of opposite spin were brought into proximity.

Besides demonstrating that the basic 2DHS studied had strong mixing of LH and HH states at the Fermi wavevector, the parallel field measurements in both cases provided evidence for the importance of the exchange interaction. It

should be borne in mind that the 'raw' Coulomb energy of interaction between a pair of holes in a typical 2DHS is over 50 K, which exceeds the Fermi energy by almost a factor of three.

9.2 The two-dimensional hole system

9.2.1 Confinement symmetry

Towards the end of Chapter 2, new (but preliminary) results were presented which demonstrated the relationship between the reflection-symmetry of the quantum-well confinement potential and the low-field Shubnikov-de Haas oscillations. This was achieved by changing the electric field perpendicular to the 2DHS, whilst keeping its carrier concentration constant, using a sample with both a front gate and a back gate. In the past, there have been studies of this effect in different samples; this measurement enabled the in-situ variation of the potential in one sample. It proved to be possible to interpret the results in terms of a model at zero magnetic field, in which the electric field lifted the two-fold degeneracy of the 2D subbands.

9.2.2 Tilted-field measurements

Chapter 4 presented detailed measurements of the integer quantum Hall effect states of the 2DHS in tilted magnetic fields. It was found that the hole Landau levels at $\nu = 4$ were well described by an approximately isotropic g factor with a magnitude close to one.

Careful activation-energy measurements at constant filling factors were used to determine the energy gaps, Δ_ν, as a function of total magnetic field. It was found that at even filling factors the energy gaps decreased approximately linearly to a turning point at non-zero gap, and then increased. In contrast, at odd filling factors, the Δ_ν versus B dependence appeared to exhibit curvature over a range of magnetic fields.

Owing to the current absence of a simple, intuitive, theory to describe the tilted-field measurements of the 2DHS, a qualitative model was introduced which incorporated some features of the complex dispersion of hole Landau levels as a function of $B_\perp$. This model explained the apparent curvature observed at odd filling factors in terms of the crossing of the Landau levels above and below the chemical potential at different total magnetic fields. The failure of the hole Landau levels to cross at even filling factors was discussed in the context of an anticrossing due to the low symmetry of the system. However, it was argued that this picture failed to account for the apparent lack of curvature in the Δ_4 versus B data.

Exchange effects in hole systems have received very little attention to date. It was demonstrated here that the data at even filling factor could be explained very simply in terms of a first-order phase transition driven by the exchange interaction, and some estimates and limits for the exchange contributions to the single-particle excitation gaps were presented.

9.2.3 Suggestions for further work

Many more experiments will have to be performed to distinguish unambiguously between the anticrossing and phase-transition theories. To prove that there is a truly discontinuous change in the magnetization of the system is a formidable task.

Experiments which could be performed include repetitions of the activation-energy measurements in a dilution refrigerator, which would enable a more reliable measurement of small energy gaps. Higher filling factors could also be investigated in a cryostat with a lower base temperature. A useful experimental facility would be the ability to vary $B_{||}$ and $B_{\perp}$ independently. This would enable a very high resolution study of the turning point of the Δ_4 data. However, this combination of magnetic fields is rather difficult to achieve in practice because it requires the presence of a pair of orthogonal superconducting magnets.

An essential component of future work will be accurate **k**.**p** calculations of the Landau levels in a tilted magnetic field; it will probably be necessary to go beyond the axial approximation. These will provide predictions of the magnetic fields of the turning points, and their energy gaps. If the first-order phase transition does occur, then the measured energy gaps will be larger than those predicted and the turning points will occur at lower magnetic fields. It is pointed out that, according to reference [91], 4×4 Luttinger Hamiltonian calculations fail to account fully for the ρ_{xx} oscillations observed in their experiments.

However, the crucial test is the detection of a discontinuity in the magnetization. Unfortunately, transport measurements offer a rather indirect probe of such thermodynamic quantities; and direct measurements of magnetization are notoriously difficult [159]. It could be that an optical probe such as magneto-absorption would be more suitable, as the polarization-dependence may be related rather simply to the spin composition of the optically active levels [160]. However, the requirements of temperatures far below 1 K and in-situ rotation of the sample will limit the ease of such experiments.

Finally, it is mentioned that the InGaAs/InP material system has a large *electron g* factor, which allows Landau level coincidence experiments at low filling factors to be performed at accessible magnetic fields; indeed, this is

the basis for the experiment reported in reference [123]. Measurements of Δ_ν versus B would be simpler to interpret because of the parabolic conduction band.

9.3 The one-dimensional hole system

9.3.1 The 1DHS at zero magnetic field

Chapter 6 presented a method for the fabrication of 1DHSs, using a 'mid-line' technique to limit some of the instabilities that have plagued previous small structures fabricated in hole systems.

Three devices of differing geometries were fabricated which clearly exhibited 'plateaux' in their pinch-off curves. However, the plateaux were not very flat and their conductances were found to deviate from integer multiples of e^2/h. The latter result was explained in terms of non-ideal coupling between the 2D and 1D regions of the devices. The quality of the devices was significantly higher than those studied previously, and enabled the first detailed measurements of the properties of holes in 1D.

It was shown, by the application of a perpendicular magnetic field, that at $B = 0$ each plateau was two-fold degenerate within the resolution of the experiment. DC source-drain bias measurements were used to estimate the spacings between the 1D subband edges of the constrictions, which were found to be an order of magnitude smaller than those of typical 1DESs.

9.3.2 Small parallel magnetic fields

Chapter 7 described how the conductance was affected by a magnetic field oriented perpendicular to the current flow through the 1DHS but parallel to the crystal growth plane. A change in the conductance quantization was observed from even to odd integer multiples of e^2/h. This was interpreted in terms of the crossing of 1D subband edges; from the magnetic fields at which the odd quantization was most clear, and using DC-bias measurements obtained on the same cooldown, the parallel 1D g factors of the system were deduced. These were found to increase as fewer 1D subbands were occupied in the constriction.

The increase in the 1D g factors of the 1DHS was discussed in the context of mixing effects and exchange interactions. The mixing effect was argued to be unlikely to explain the observed increase, because the 1DHS remained rather wide in comparison with the width of the quantum well. However, this argument will require verification by modelling.

In general, exchange interactions increase in importance as a system becomes increasingly one dimensional. It was argued that the increased coupling between the Coulomb interaction energy and the 'spin' of the hole system towards pinch-off could explain some features of the observed enhancement.

9.3.3 Large parallel magnetic fields

Chapter 8 presented measurements of the 1DHSs at even higher parallel magnetic fields. The quantization of the conductance exhibited changes between even and odd multiples of e^2/h consistent with the crossing of the 1D subband edges as many as four times. Measurements were also presented of a 1DHS in a tilted magnetic field, which showed a cross-over between the Zeeman effect and the quantum Hall effect in the one-dimensional system. Speculation on the ways in which exchange interactions might affect the system was also provided.

9.3.4 Suggestions for further work

Device stability for all gate voltages is the fundamental requirement for detailed studies of the 1DHS. Although the devices measured as a part of this work were significantly more stable than the only previous working 1DHSs, they proved to be far from ideal.

It was speculated that the instabilities observed in these devices arose from charge mobility in the doped regions of the heterostructure. An elegant method for the fabrication of an ultra-clean 2DS uses a front gate to induce carriers into an undoped heterostructure [161]. This technique has recently been extended by the authors of reference [161], and independently by this research group [162], to enable the fabrication of long clean 1DESs. When applied to the hole system, the technique should provide stable 1DHSs because of the lack of dopants.

With an ideal 1DHS, there are a number of experiments that should be performed. Firstly, the multiple crossing of the 1D subbands as a function of parallel magnetic field needs to be investigated for $B_{||}$ oriented both perpendicular and parallel to the current direction. The use of the gate voltage axis as a reference is likely to reveal a plethora of anticrossing and exchange effects. The parallel 1D g factors could then be determined; it is certain that the absolute values will depend on the characteristics of both the 2D and 1D confinement and carrier concentrations. The interesting result would be the observation of an oscillatory enhancement independent of the absolute values of the g factors. It could also prove to be fruitful to investigate the importance of the orientations of the parallel magnetic field with respect to the lateral con-

finement potential, and of the crystallographic direction with respect to the constriction potential.

The fabrication of long 1DHSs will also facilitate the study Luttinger liquid [163, 138, 137] effects in this strongly interacting system.

Appendix A

Physical constants

SI units have been used in most of this thesis. Exceptions include quantities involving energy, which is often usually expressed in electron volts (eV) or Kelvin (K), and distance which is sometimes measured in Angstroms (Å). The physical constants relevant to this thesis are tabulated below.

Symbol	Constant	Value	Unit
e	Electronic charge	1.602×10^{-19}	C
$\hbar$	Planck's constant	1.055×10^{-34}	Js
m_0	Electron mass in free space	9.110×10^{-31}	kg
k_B	Boltzmann constant	1.381×10^{-23}	JK^{-1}
ϵ_0	Permittivity of free space	8.854×10^{-12}	Fm^{-1}
μ_B	Bohr magneton	9.274×10^{-24}	JT^{-1}

Appendix B

Wafer structures

This appendix contains the structures of the wafers studied in this thesis. All of the wafers were grown by Dr M. Y. Simmons using MBE on the (311)A surface of GaAs substrates, using Si as the p-dopant (see Chapter 1). The aluminium fraction x of the Al_xGa_xAs regions was 0.33.

Material	Doping / 10^{18} cm^{-3}	Thickness / Å	Comment
GaAs	-	170	Cap
AlGaAs	0.12	2000	Doped
AlGaAs	-	600	Spacer
GaAs	-	200	Quantum Well
AlGaAs	-	800	Spacer
AlGaAs	0.12	2000	Doped
AlGaAs	-	2500	Cooled
AlGaAs*	-	1000	
GaAs	-	20000	
GaAs	-	-	substrate

Table B.1: Structure of the symmetrically-doped quantum well T240. The asterisk indicates that the Al concentration was ramped from 0 to 0.33 in that particular growth phase.

Material	Doping / 10^{18} cm^{-3}	Thickness / Å	Comment
GaAs	-	170	Cap
AlGaAs	0.1	2000	Doped
AlGaAs	-	1150	Spacer
GaAs	-	200	Quantum Well
AlGaAs	-	950	Spacer
AlGaAs	0.1	2000	Doped
AlGaAs	-	2500	Cooled
AlGaAs*	-	1000	
GaAs	-	20000	
GaAs	HIGH	-	n+ substrate

Table B.2: Structure of the T335n+ quantum well, which is approximately symmetrically doped. It was grown on an n+ substrate.

Material	Doping / 10^{18} cm^{-3}	Thickness / Å	Comment
GaAs	-	170	Cap
AlGaAs	1.2	400	Doped
AlGaAs	-	270	Spacer
GaAs	-	1000	
GaAs	-	10000	
GaAs	-	-	substrate

Table B.3: Structure of the single-interface heterostructure T136

Appendix C

Processing techniques

C.1 Preliminaries

Following the growth of the wafer by MBE, a number of processing steps must be carried out to produce a sample suitable for measurement.

The wafers studied in this work were grown by Dr M. Y. Simmons using a Varian Gen-II MBE machine, in which the wafers are secured to the substrate holder using an Indium/Gallium amalgam. The first step of the processing procedure is therefore to strip these metals from the underside of the wafer, by immersing it in a concentrated solution of HCl. It should be noted that considerable diffusion of indium occurs into the underside of the substrate, because of the elevated growth temperatures. The diffused indium is not removed by the stripping procedure.

The wafer is then scribed, using a diamond-tipped stylus, and cleaved into conveniently-sized chips which typically measure 5×5 mm. The preferential

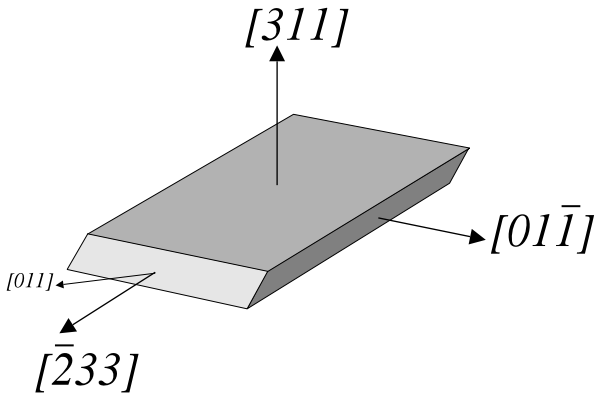

Figure C.1: The cleavage planes of a (311)-grown wafer.

cleavage planes of GaAs are generally those with low Miller indices, {100} and {011}. An orthogonal combination of these planes with the (311) plane cannot be found, which means that in contrast to (100)-grown wafers, the faces of a cleaved chip will not all be orthogonal. In fact, the $[01\overline{1}]$ direction is orthogonal to [311] but the [011] is not. Therefore the $[\overline{2}33]$ direction can be identified by the fact that it runs parallel to those sides of the chip which are orthogonal to its upper surface. Figure C.1 shows that the other pair of faces, with indices (011), are bevelled.

C.2 Mesa etch

The next stage in the processing is the etching of selected areas of the chip to produce a *mesa*, to restrict the 2DHS to a well-defined strip of typical dimensions 80×800 μm. This region of 2DHS is known as a Hall bar, and is 'contacted' by a set of narrower mesas which will eventually connect to ohmic contacts (see Section C.6).

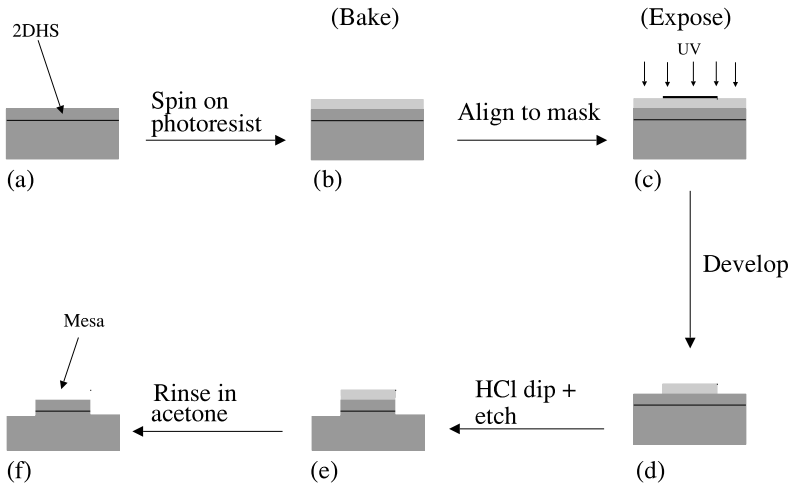

Figure C.2: Schematic diagram of processing steps required to create a mesa.

The area to be etched is defined by optical lithography, as follows. A layer of Microposit 1813-S positive photoresist is spun onto the top surface of the chip, and is then baked for ten minutes at 70°C. The chip is aligned to a mask, which is brought into contact with the surface, and the uncovered regions of photoresist are exposed to ultraviolet (UV) light. The photoresist is then developed in Microposit MF319 developer; this solution dissolves only those regions of the resist which were exposed to the UV radiation. These processing steps are depicted in Figs. C.2(a) to (d).

The chip is then 'cleaned' in a 10% aqueous solution of HCl; this process dissolves the thin layer of oxide on the surface of the chip, and dislodges dirt and traces of developed photoresist which may have adhered to the oxide. Such 'HCl dips' follow all development stages, and precede all evaporation stages.

The exposed regions of the chip are then etched using a 100:8:1 mixture of H_2O:H_2O_2:H_2SO_4; the etch-rate is typically 50 Ås^{-1} at 22°C. The depth of the etch is periodically checked using a DekTak surface profiler; a total etch-depth greater than the distance between the surface of the chip and the 2DHS is chosen. The resist is then stripped from the chip using acetone, to leave the Hall bar, and rinsed in propanol to prevent the formation of a residue. See Figs. C.2(d) to (f).

C.3 Ohmic contacts

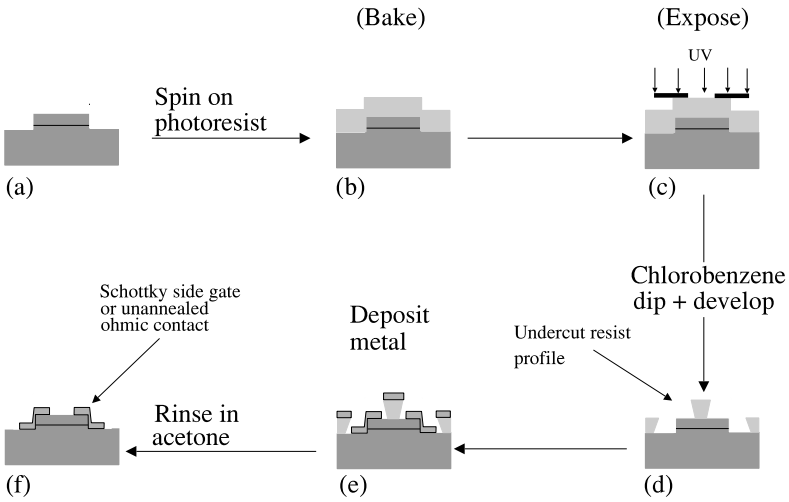

Figure C.3: Schematic diagram of processing steps required to pattern metal onto the surface. In the case for ohmic contacts, an anneal is required after step (f). No anneal is used for Schottky gates.

The next stage of the processing is to fabricate ohmic contacts to the 2DHS, and is depicted in Fig. C.3.

The chip is re-coated with photoresist and baked, and then exposed using a mask for ohmic contacts. Before development, the exposed chip is immersed in chlorobenzene for seven minutes. Figure C.3(d) shows that the profile of the developed resist is undercut, because its surface is hardened by the chloroben-

zene.

Following an HCl dip, the chip is placed into an evaporator and approximately 200 nm of Au/Be alloy (10% Be by mass) is deposited onto the surface, at a rate of approximately 0.4 nm per second. Immersion of the chip in acetone removes the remaining resist and 'lifts off' metal deposited onto it, to leave only the metal adhered directly to the mesa. Lift-off is facilitated by the under-cut profile of the resist. Ohmic contact is made to the 2DHS by a carefully controlled anneal using a Leisk annealer, in a reducing atmosphere of hydrogen and nitrogen. The optimal anneal time was determined by experiment to be approximately 480°C for three minutes, giving resistances of between 250 Ω and 700 Ω per ohmic contact at temperatures below 4 K.

C.4 Schottky gates

The final stage of optical lithography is the deposition of Schottky gates onto the Hall bar. The processes described above for ohmic contacts are repeated, except that the metallization is usually 10 nm of NiCr alloy followed by 70 nm of Au. There is no anneal. The NiCr is deposited first because it adheres more strongly to the GaAs surface than does Au; if it is omitted then problems are encountered during bonding.

The optically-defined Schottky gates used in the course of this work fall into two categories. For two-dimensional measurements in which it is necessary to be able to vary the carrier concentration, large gates are deposited which cover many squares of the 2DHS. These are known as 'front gates'. For chips intended for electron-beam lithography (subsection C.5), 'side-gates' are patterned onto the chip. They climb onto the mesa but do not cross it, and provide electrical contact to the smaller features to be defined by electron-beam lithography.

C.5 Electron-beam lithography

Diffraction limits the minimum size of features which can be defined to length scales larger than the wavelength of the radiation used; a typical lower limit for optical lithography is approximately 1 μm. For this reason, the split gates used to make 1DHSs (which contain feature sizes of around 0.1 μm) are patterned using electron-beam lithography.

In this research group, electron-beam lithography is performed using a 25 keV Hitachi scanning electron microscope (SEM) modified by the addition of a pattern generator. The spot-size of the electron beam is around 20 Å; the proximity effect, which arises from scattering of the electron-beam by the

substrate and resist, reduces the resolution so that the minimum feature size possible is approximately 0.05 μm.

The resist used for this work was the polymer: isofine P5 polymethylmethacrylate (PMMA). It is spun onto the chips to produce a layer of resist of thickness 180 nm. The chip is then baked for at least thirty minutes at 150°C. Devices are 'drawn' using patterns carefully designed to minimize the inherent instabilities of the SEM and proximity effects, and are then developed in 3:1 solution of propanol:MIBK (methylisobutylketone) which dissolves regions of the resist exposed to the electron beam. A standard HCl dip, and then the deposition of 10 nm of NiCr and 30 nm of Au, follow. Lift-off of the unwanted metal is achieved in acetone, and can take a number of hours.

C.6 Bonding

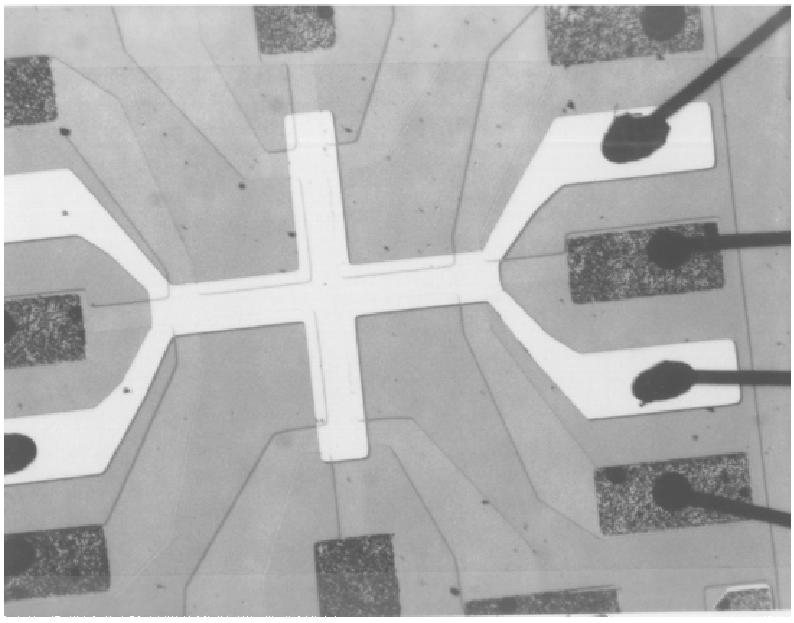

Figure C.4: Photograph of a completed chip. The light region is a NiCr/Au Schottky front gate, on top of a pair of orthogonal Hall-bar mesas. The dark, mottled, areas are annealed AuBe ohmic contacts. Strips of mesa connect ohmic contacts to voltage probes on the Hall bars. Bond wires are visible on the right-hand side of the photograph.

Completed chips are glued by their under-surface to a twenty-pin package using GE varnish or silver-epoxy resin, and the ohmic- and Schottky-contact

bond-pads are electrically connected to the pins of the package by fine gold wire, using a Kulick and Soffa ultrasonic ball-bonder. A photograph of a completed chip is presented in Fig. C.4. Particular care must be taken when bonding to samples containing small gate features, because the ball on the end of the gold wire is created by a spark which can destroy fine features.

Appendix D

Measurement techniques

D.1 Introduction

The measurements presented in this thesis were performed at very low temperatures. This appendix presents some of the important concepts pertaining to electrical measurement at low temperatures, and diagrams of typical circuits used.

Typically, ohmic-contact and gate-leakage characterization are performed in ^{4}He dewars, which provide sample temperatures of approximately 4 K by immersion in liquid helium, or in pumped-^{4}He cryostats with base temperatures of 1.5 K. Experiments are performed in pumped-^{3}He cryostats, with base temperatures of around 0.28 K, or in dilution refrigerators which attain temperatures as low as 30 mK. In practice, the temperature which characterizes the hole system is slightly higher than that of the crystal lattice because of the lack of phonons, which provide the thermal coupling at higher temperatures. A detailed description of the cryogenic techniques employed in the field of low-temperature solid state physics may be found in reference [164]

D.2 Lock-in amplifiers

The measurement of resistance, or conductance, at temperatures below 1 K is problematic because the passage of a current through a sample dissipates heat, and may increase its temperature. This effect can only be avoided by the use of very small excitations, which then introduce the problem of separating the signal from electrical noise. These difficulties may be alleviated through the use of a lock-in amplifier (LIA), which may be considered to act as a very sensitive voltmeter.

To illustrate the properties of a LIA, it is convenient to consider the mea-

surement of the resistance of a resistor, as depicted in Fig. D.1(a). The measurement is performed by using an AC constant-current source to provide a known current I_{ex} through the resistor, at some frequency ω. The voltage dropped across the resistor, V_{R} is measured using the LIA. In general, V_{R} is the sum of the desired signal, at frequency ω, and a noise voltage which is also a function of frequency.

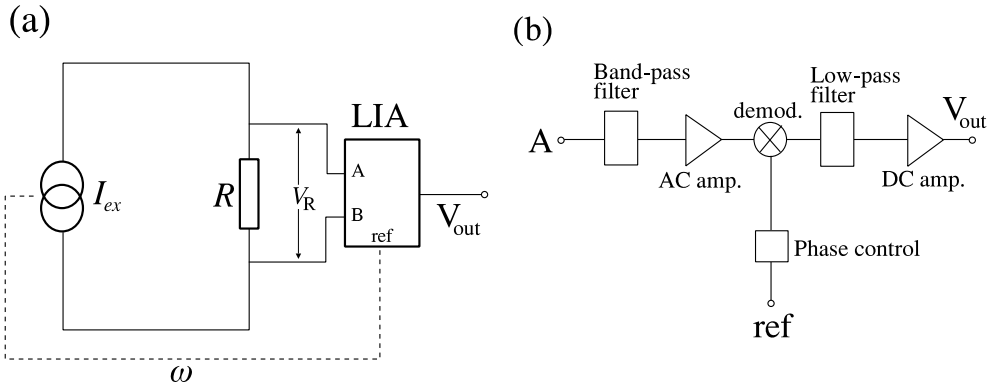

Figure D.1: (a) Schematic diagram of a measurement of a voltage across a resistor, using a LIA. (b) Block diagram of a LIA, showing the AC and DC amplification stages.

The ideal LIA may be considered to amplify the portion of the input signal over some very narrow frequency range $\omega - \delta\omega < \omega < \omega + \delta\omega$. In the simplest of analogue cases this is achieved by multiplying the signal by the reference, which yields a DC ($\omega = 0$) component proportional to the voltage required and AC components at all other frequencies. This signal is passed through a low-pass filter and is then amplified by a high quality DC amplifier to produce an output voltage proportional to I_{ex}/R. The reference frequency is typically chosen to be less than 100 Hz; in this frequency range, the dominant source of electrical noise is mains pick-up. Although pick-up was always minimized in experimental circuits, by the use of twisted pairs and the elimination of earth loops, it was found to be difficult to reduce it to less than 0.2 μV peak to peak; therefore reference frequencies near to 50 Hz are always avoided.

Modern LIAs achieve better noise rejection and stability through a multi-stage amplification process, and may be classified as either analogue or digital according to the nature of their circuitry. The only analogue LIAs used extensively in this work were from the Brookdeal 9500 series. The amplification process in such a LIA is depicted in Fig. D.1(b). The input to the LIA is filtered using a fairly broad band-pass filter; it is then subjected to an AC

amplification stage followed by demodulation (i.e. selection of the required frequency component) and a DC amplification stage.

For a given total gain, the experimental physicist has some control of the way the amplification is shared between the AC and DC amplifiers. The AC amplifier usually has higher linearity and greater stability than the DC amplifier; switching the dynamic reserve of the LIA to 'low' transfers as much of the amplification to the AC stage as possible. However, the LIA can fail to lock-in if the noise on the input signal increases. In these circumstances, the noise-rejection is improved by limiting the AC amplification; however, the DC amplification stage introduces offsets onto the output of LIA, thereby distorting the recorded measurement.

Purely digital LIAs such as the Standford SR830 offer very high performance, because the signal processing is achieved purely computationally. The problems of noise-induced offsets are eliminated entirely. However, for measurements at millikelvin temperatures, analogue LIAs are preferred because they do not contain high-frequency circuits that can introduce noise into the measurement circuit and actually heat the sample. Measurements were generally performed using analogue LIAs, or hybrid LIAs such as the EG&G 5209 or 5210 models.

D.3 Two- and four-terminal measurements

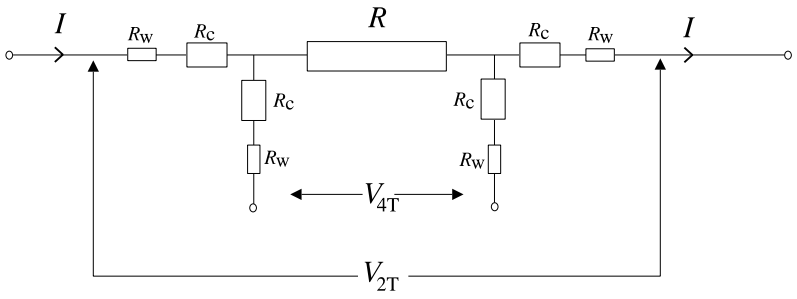

Figure D.2: Schematic diagram showing two and four terminal resistance measurements.

The simplest of resistance measurements is two terminal, in the sense that the voltage is measured using the same contacts that are used to pass the current through the sample. Referring to Fig. D.2, the voltage dropped due to the current I is $V_{2T} = I \times (2R_w + 2R_c + R)$, where R_w, R_c and R represent the resistances of the wires, contacts and sample respectively. Therefore the measured resistance, R_{2T}, is affected by the wires and contacts used. Four-terminal

measurements use different ohmic contacts for the measurement of the voltage and the conduction of the current. Provided that the input impedance of the voltmeter is much greater than the resistance of the sample, the current drawn by the voltmeter is negligible. The voltage measured is then $V_{4T} = I \times R$, and is therefore unaffected by the resistances of the contacts and wires.

D.3.1 Typical experimental configurations

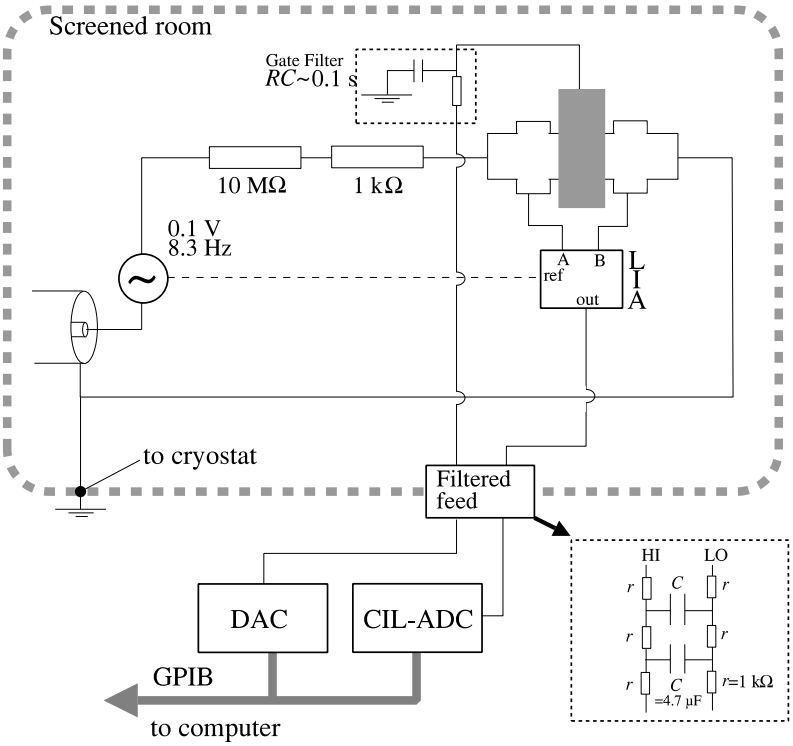

Figure D.3: Schematic diagram of a constant-current measurement.

Figure D.3 shows a generic four-terminal measurement of ρ_{xx}, using a circuit in the constant-current configuration. All of the sensitive measurements presented in this thesis were performed in screened rooms, which offer better electrical-noise characteristics than can be found elsewhere in the laboratory. The data are acquired by feeding the analogue output of the LIAs out of the screened room via low-pass filters incorporating resistors on both high and low connections to break earth loops. This voltage is digitized by a CIL microsystems analogue to Digital Converter (ADC), which communicates using IEEE connections with the computer used to control equipment and record data.

The software used for this purpose is the *CryoMeas* program written by Dr C. J. B. Ford. DC voltages used for biasing Schottky gates, and for applying a DC source-drain bias to the samples, are obtained from IQ-Tech DAC 488/4 'quad sources'. They provide a 0.25 mV resolution floating voltage with 0.5 Ω output impedance. This source is also kept out of the screened room.

The excitation is provided by placing a 10 MΩ resistor in series with a Brookdeal 9473 signal source, which has an output impedance of 50 Ω. Obviously, a constant current is only provided if the impedance of the device remains much less than that of the series resistor. A 1 kΩ resistor is also included to facilitate measurement of the current. The voltage dropped across the ohmic contacts is measured differentially, with a LIA referenced to the signal source. Typical frequencies for quantum Hall effect measurements lay in the range two to eight Hertz.

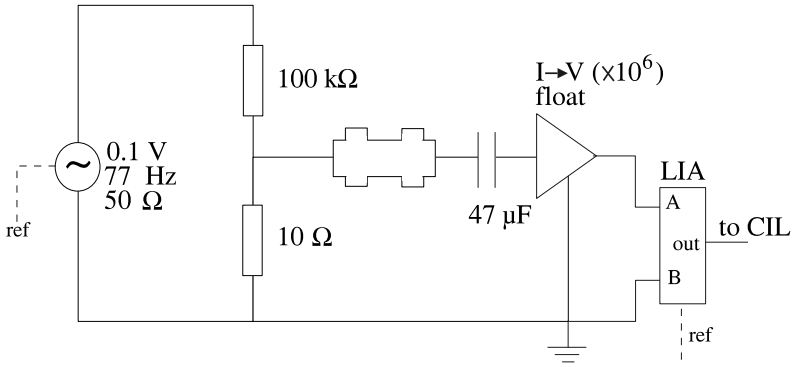

Figure D.4: Schematic diagram of a constant-voltage measurement.

Measurements of 1DHSs were always performed using constant-voltage circuits; a typical circuit is presented in Fig. D.4. Provided that the total resistance of the sample is much greater than 10 Ω, the voltage divider provides an approximately constant 10 μV AC excitation across the source and the drain. The constant-voltage circuits were calibrated by replacing the sample with a calibrated 10 kΩ resistor.

The current flowing through the 1DHS is measured using a floating current pre-amplifier (with negligible input impedance) which produces an output voltage with a gain 10^6 V/A that is measured using a LIA. It is common practice to place a large capacitor between the drain and the current amplifier to 'block' any DC offset voltage between its high and low inputs.

The DC-bias measurements presented in Chapter 6 were performed using the circuit depicted in Fig. D.5, which was designed to allow the gate voltages to be referenced to half of the DC source-drain voltage across the device.

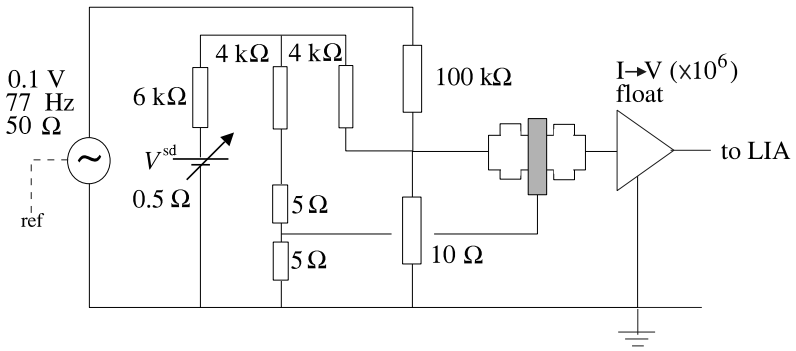

Figure D.5: Schematic diagram of circuit which allows for symmetric DC biasing.

This symmetric biasing arrangement requires the use of a floating DC voltage source; the biases across the device were measured independently using a DC voltage pre-amplifier.

As the device is pinched off, the AC and DC voltages dropped across it change. Because the circuits were calibrated near to pinch off, errors may be expected to occur when the device has high conductance. However, because the series resistance of the devices always exceeds 600 Ω, the change in the voltage amounts to 1.6% at most. Furthermore, conductances of interest always occurred for total device resistances in excess of 3 kΩ, which are subject to errors of only 0.3%.

Appendix E

Some notes on the Luttinger Hamiltonian

This brief appendix contains some notes relevant to Section 2.2.2 of Chapter 2. The Luttinger Hamiltonian (equation 2.1) may be written as a single 4×4 matrix. In one representation of the **J** matrices, we obtain [56]:

$$H_{\mathbf{k}} = \begin{pmatrix} P+Q & S & R & 0 \\ S^{\dagger} & P-Q & 0 & R \\ R^{\dagger} & 0 & P-Q & -S \\ 0 & R^{\dagger} & -S^{\dagger} & P+Q \end{pmatrix} \tag{E.1}$$

with

$$\begin{aligned} P &= \tfrac{\hbar^2}{2m}\gamma_1 k^2, \\ Q &= \tfrac{\hbar^2}{2m}\gamma_2 (k_x^2 + k_y^2 - 2k_z^2), \\ S &= -\tfrac{\hbar^2}{2m}\gamma_3 (2\sqrt{3}) k_- k_z, \\ R &= -\tfrac{\hbar^2}{2m}\sqrt{3}/2[(\gamma_2+\gamma_3)k_-^2 + (\gamma_2-\gamma_3)k_+^2], \end{aligned} \tag{E.2}$$

where $\gamma_1 = 6.85 \pm 0.15, \gamma_2 = 2.1 \pm 0.15$ and $\gamma_3 = 2.9 \pm 0.15$ are the $\mathbf{k} \cdot \mathbf{p}$ parameters [4], and $k_{\pm} = k_x \pm i k_y$. The z direction has been taken to point in the [100] crystallographic direction. For systems grown on alternative planes, it is necessary to rotate the coordinate system to align the z axis to the required crystallographic direction.

To find the 2D subband dispersions, a confinement potential $V(z)$ may be added along the diagonal of the matrix, and k_z is replaced by the operator $-id/dz$. The matrix operates on the envelope function $\mathbf{F} = (F_1, F_2, F_3, F_4)$,

which is related to the wavefunction by $\Psi = F_1|3/2, 3/2\rangle + F_2|3/2, 1/2\rangle + F_3|3/2, -1/2\rangle + F_4|3/2, -3/2\rangle$. The simplest case of an infinite symmetric quantum well in the flat-band limit has an analytic solution [165]; an exact solution may also be found for a well of finite depth [166].

The general problem requires the numerical solution of the system of four coupled second-order differential equations subject to suitable boundary conditions. If the well is infinite, it is sufficient to assume that $\mathbf{F} = 0$ at its boundaries.

Bibliography

[1] M. A. Herman and H. Sitter, *Molecular beam expitaxy*, Springer series in Materials Science 7, Springer, Berlin, 2nd ed., 1996.

[2] W. I. Wang, E. E. Mendez, T. S. Kuan, and L. Esaki, *Crystal orientation dependence of silicon doping in molecular beam epitaxial AlGaAs/GaAs heterostructures*, Appl. Phys. Lett., **47**, 826 (1985).

[3] R. Notzel, N. N. Ledentsov, L. Daweritz, K. Ploog, and M. Hohenstein, *Semiconductor quantum-wire structures directly grown on high-index surfaces*, Phys. Rev. B, **45**, 3507 (1992).

[4] O. Madelung, *Physics of group IV elements and III-V compounds*, Springer, Berlin, 1982.

[5] K. H. Hellwege, *Semiconductors. Intrinsic Properties of Group IV Elements and III-V, II-VI and I-VII Compounds*, Springer, Berlin, 1987.

[6] M. J. Kelly, *Low-dimensional semiconductors*, Oxford University Press, 1995.

[7] O. Madelung, *Numerical data and functional relationships in science and technology; New Series, Group III: Crystal and Solid State Physics*, vol. 17 of Landolt-Bornstein, Springer, Berlin, 1982.

[8] M. Y. Simmons, D. A. Ritchie, I. Zailer, A. C. Churchill, and G. A. C. Jones, *Optimization of high mobility two-dimensional hole gases*, J. Vac. Sci. Technol. B, **12**, 1296 (1993).

[9] A. G. Davies, *The fractional quantum Hall effect in high mobility two-dimensional hole gases*, PhD thesis, University of Cambridge, 1991.

[10] A. G. Davies, J. E. F. Frost, D. A. Ritchie, D. C. Peacock, R. Newbury, E. H. Linfield, M. Pepper, and G. A. C. Jones, *The growth and physics of high mobility two dimensional hole gases*, J. Crys. Growth, **111**, 318 (1991).

[11] J. Heremans, M. B. Santos, K. Hirakawa, and M. Shayegan, *Mobility anisotropy of two dimensional holes systems in* (311)*A GaAs/AlGaAs heterojuctions*, J. Appl. Phys., **76**, 1980 (1994).

[12] M. Y. Simmons, A. R. Hamilton, S. J. Stevens, D. A. Ritchie, M. Pepper, and A. Kurobe, *Fabrication of high mobility* in situ *back-gated* (311)*A hole gas heterojuctions*, Appl. Phys. Lett., **70**, 2750 (1997).

[13] H. Fukuyama and E. Abrahams, *Inelastic scattering time in two-dimensional metals*, Phys. Rev. B, **27**, 5976 (1983).

[14] I. Zailer, J. E. F. Frost, C. J. B. Ford, M. Pepper, M. Y. Simmons, D. A. Ritchie, J. T. Nicholls, and G. A. C. Jones, *Phase coherence, interference, and conductance quantization in a confined two-dimensional hole gas*, Phys. Rev. B, **49**, 5101 (1994).

[15] C. W. J. Beenakker and H. van Houten, *Quantum transport in semiconductor nanostructures*, vol. 44 of Solid state physics, Academic Press, New York, 1991.

[16] J. M. Ziman, *Principles of the theory of solids*, Cambridge University Press, 1972.

[17] R. Landauer, *Electrical resistance of disordered one-dimensional lattices*, Phil. Mag., **21**, 863 (1970).

[18] M. Buttiker, *Four-terminal phase-coherent conductance*, Phys. Rev. Lett., **57**, 1761 (1986).

[19] H. U. Baranger and A. D. Stone, *Electrical linear-response theory in an arbitrary magnetic field: A new Fermi-surface formation*, Phys. Rev. B, **40**, 8169 (1989).

[20] L. I. Schiff, *Quantum mechanics*, McGraw-Hill Book Co., Singapore, 1968.

[21] T. Ando, A. B. Fowler, and F. Stern, *Electronic properties of two-dimensional systems*, Rev. Mod. Phys., **54**, 437 (1982).

[22] K. von Klitzing, G. Dorda, and M. Pepper, *New method for the high-accuracy determination of the fine-structure constant based on quantized Hall resistance*, Phys. Rev. Lett., **45**, 494 (1980).

[23] H. L. Stormer, Z. Schlesinger, A. Chang, D. C. Tsui, A. C. Gossard, and W. Wiegmann, *Energy structure and quantized Hall effect of two-dimensional holes*, Phys. Rev. Lett., **51**, 126 (1983).

[24] H. P. Wei, D. C. Tsui, M. A. Paalanen, and A. M. M. Pruisken, *Experiments on delocalization and universality in the integral quantum Hall effect*, Phys. Rev. Lett., **61**, 1294 (1988).

[25] R. E. Prange and S. M. Girvin, *The quantum Hall effect*, Springer Verlag, New York, 2nd ed. ed., 1990.

[26] D. B. Chklovskii, B. I. Shklovskii, and L. I. Glazman, *Electrostatics of edge channels*, Phys. Rev. B, **46**, 4026 (1992).

[27] R. J. F. van Haren, F. A. P. Blom, and J. H. Wolter, *Direct observation of edge channels in the integer quantum Hall regime*, Phys. Rev. Lett., **74**, 1198 (1995).

[28] D. C. Tsui, H. L. Stormer, and A. C. Gossard, *Two-dimensional magnetotransport in the extreme quantum limit*, Phys. Rev. Lett., **48**, 1559 (1982).

[29] H. L. Stormer, A. Chang, D. C. Tsui, J. C. M. Hwang, A. C. Gossard, and W. Wiegmann, *Fractional quantization of the Hall effect*, Phys. Rev. Lett., **50**, 1953 (1983).

[30] A. G. Davies, R. Newbury, M. Pepper, J. E. F. Frost, D. A. Ritchie, and G. A. C. Jones, *Fractional quantum Hall effect in high-mobility two dimensional hole gases in tilted magnetic fields*, Phys. Rev. B, **44**, 13128 (1991).

[31] S. Kivelson, D.-H. Lee, and S.-C. Zhang, *Global phase diagram of the quantum Hall effect*, Phys. Rev. B, **46**, 2223 (1992).

[32] J. K. Jain, *Strongly correlated fractional quantum Hall states - description in terms of weakly interacting composite fermions*, Surf. Sci., **263**, 65 (1992).

[33] T. J. Thornton, *Transport properties of a gated GaAs/AlGaAs heterojunction*, PhD thesis, University of Cambridge, 1987.

[34] T. J. Thornton, M. Pepper, H. Ahmed, D. Andrews, and G. J. Davies, *One-dimensional conduction in the 2D electron gas of a GaAs/AlGaAs heterojuction*, Phys. Rev. Lett., **56**, 1198 (1986).

[35] A. Yacoby, H. L. Stormer, K. W. Baldwin, L. N. Pfeiffer, and K. W. West, *Magnetotransport spectroscopy on a quantum wire*, Sol. St. Commun., **101**, 77 (1997).

[36] B. J. van Wees, H. van Houten, C. W. J. Beenakker, J. G. Williamson, L. P. Kouwenhoven, D. van der Marel, and C. T. Foxon, *Quantized conductance of point contacts in a two dimensional electron gas*, Phys. Rev. Lett., **60**, 848 (1988).

[37] D. A. Wharam, T. J. Thornton, R. Newbury, M. Pepper, H. Ahmed, J. E. F. Frost, D. G. Hasko, D. C. Peacock, D. A. Ritchie, and G. A. C. Jones, *One-dimensional transport and the quantization of the ballistic resistance*, J. Phys.: Cond. Matt., **21**, 209 (1988).

[38] J. J. Heremans, M. B. Santos, and M. Shayegan, *Observation of magnetic focusing in two dimensional hole systems*, Appl. Phys. Lett., **61**, 1652 (1992).

[39] J. Heremans, M. B. Santos, and M. Shayegan, *Transverse magnetic focusing and the dispersion of GaAs 2D holes at* (311)*A heterojunctions*, Surf. Sci., **305**, 348 (1994).

[40] G. Dresselhaus, *Spin-orbit coupling effects in zinc blende structures*, Physical Review, **100**, 580 (1955).

[41] G. Davidson, *Group theory for chemists*, Macmillan, London, 1991.

[42] G. Burns, *Solid state physics*, Academic Press inc., 1990.

[43] C. Kittel, *Quantum theory of solids*, John Wiley and Sons inc., 1987.

[44] J. R. Chelikowsky and M. L. Cohen, *Non-local pseudopotential calculations for the electronic structure of eleven diamond and zinc-blende semiconductors*, Phys. Rev. B, **14**, 556 (1976).

[45] T. C. Chiang, J. A. Knapp, M. Aono, and D. E. Eastman, *Angle-resolved photoemission, valence-band dispersions $E(k)$, and electron and hole lifetimes for GaAs*, Phys. Rev. B, **21**, 3513 (1980).

[46] J. M. Luttinger, *Quantum theory of cyclotron resonance in semiconductors: General theory*, Physical Review, **102**, 1030 (1956).

[47] D. A. Broido and L. J. Sham, *Effective masses of holes at GaAs/AlGaAs heterojunctions*, Phys. Rev. B, **31**, 888 (1985).

[48] W. Hackenberg and H. P. Hughes, *Directional resolution of the GaAs heavy-hole band dispersion and photoelectron-momentum orientation from hot-electron luminescence*, Phys. Rev. B, **49**, 7990 (1994).

[49] N. O. Lipari and A. Baldereschi, *Angular momentum theory and localized states in solids. Investigation of shallow acceptor states in semiconductors*, Phys. Rev. Lett., **25**, 1660 (1970).

[50] A. Baldereschi and N. O. Lipari, *Spherical model of shallow acceptor states in semiconductors*, Phys. Rev. B, **8**, 2697 (1973).

[51] U. Ekenberg and M. Altarelli, *Subbands and Landau levels in the two-dimensional hole gas at the GaAs/AlGaAs interface*, Phys. Rev. B, **32**, 3712 (1985).

[52] U. Ekenberg and M. Altarelli, *Calculation of hole subbands at the GaAs/AlGaAs interface*, Phys. Rev. B, **30**, 3569 (1984).

[53] E. C. Valadares, *Strong anisotropy of hole subbands in* (311) *GaAs/AlGaAs quantum wells*, Phys. Rev. B, **46**, 3935 (1992).

[54] R. Winkler and U. Rossler, *General approach to the envelope-function approximation based on a quadrature method*, Phys. Rev. B, **48**, 8918 (1993).

[55] R. Winkler and A. I. Nesvizhskii, *Anisotropic hole subband states and interband optical absorption in [mmn] oriented quantum wells*, Phys. Rev. B, **53**, 9984 (1996). and private communication.

[56] R. Winkler, M. Merkler, T. Darnhofer, and U. Rossler, *Theory for the cyclotron resonance of holes in strained asymmetric Ge-SiGe quantum wells*, Phys. Rev. B, **53**, 10858 (1996).

[57] G. Bastard, *Wave mechanics applied to semiconductor heterostructures*, John Wiley and Sons inc., 1988.

[58] J. A. Kash, M. Zachau, M. A. Tischler, and U. Ekenberg, *Anisotropic valence bands in quantum wells: quantitative comparison of theory and experiment*, Phys. Rev. Lett., **69**, 2260 (1992).

[59] R. K. Hayden, D. K. Maude, L. Eaves, E. C. Valadares, M. Henini, F. W. Sheard, O. H. Hughes, J. C. Portal, and L. Cury, *Probing hole dispersion curves of a quantum well using resonant magnetotunnelling spectroscopy*, Phys. Rev. Lett., **66**, 1749 (1991).

[60] R. K. Hayden, L. Eaves, M. Henini, E. C. Valadares, O. Kuhn, D. K. Maude, J. C. Portal, T. Takamasu, N. Miura, and U. Ekenberg, *Probing hole dispersion curves of a quantum well using resonant magnetotunnelling spectroscopy*, Semiconduc. Sci. Technol., **9**, 298 (1994).

[61] H. W. van Kesteren, E. C. Cosman, W. A. J. A. van der Poel, and C. T. B. Foxon, *Fine structure in excitons in type-II GaAs/AlAs quantum wells*, Phys. Rev. B, **41**, 5283 (1990).

[62] B. E. Cole, J. M. Chamberlain, M. Hennini, T. Cheng, W. Batty, A. Wittlin, J. A. A. J. Perenboom, A. Ardavan, A. Polisski, and J. Singleton, *Cyclotron resonance in ultra-low-density narrow p-type GaAs/AlGaAs quantum wells*, Phys. Rev. B, **55**, 2503 (1997).

[63] E. Bangert and G. Landwehr, *Landau levels of the 2 dimensional hole gas in GaAs with inclusion of the anisotropy of the band structure*, Surf. Sci., **170**, 593 (1986).

[64] J. P. Eisenstein, H. L. Stormer, V. Narayanamurti, A. C. Gossard, and W. Wiegmann, *Effect of inversion symmetry on the band structure of semiconductor heterostructures*, Phys. Rev. Lett., **53**, 2579 (1984).

[65] M. Y. Simmons, A. R. Hamilton, A. Kurobe, S. J. Stevens, D. A. Ritchie, and M. Pepper, *The physics and fabrication of in situ back-gated* (311)*A hole gas heterojuctions*, Microelectronics J., **28**, 795 (1997).

[66] A. R. Hamilton, *Private communication*, 1998.

[67] K. Muraki and Y. Hirayama, *Effect of valence band structure on the fractional quantum Hall effect of two-dimensional hole systems.* To appear in Physica B, 1998. Proceedings of EP2DS-XII, Tokyo, 1997.

[68] N. W. Ashcroft and N. D. Mermin, *Solid state physics*, W.B. Saunders Co., 1976.

[69] L. Calmels and A. Gold, *Exchange and correlation in the quasi-one-dimensional electron gas: The local field correction*, Phys. Rev. B, **52**, 10841 (1995).

[70] A. Gold and A. Ghazali, *Exchange effects in a quasi-one-dimensional electron gas*, Phys. Rev. B, **41**, 8318 (1990).

[71] I. Zailer, *The physics and fabrication of low-dimensional hole systems*, PhD thesis, University of Cambridge, 1994.

[72] T. Ando and Y. Uemura, *Theory of oscillatory g factor in an MOS inversion layer under strong magnetic fields*, J. Phys. Soc. Jpn., **37**, 1044 (1974).

[73] I. S. Gradshteyn and I. M. Ryzhik, *Table of Integrals, Series and Products*, Academic Press, 1980.

[74] C. Kallin and B. I. Halperin, *Excitations from a filled Landau level in the two-dimensional electron gas*, Phys. Rev. B, **30**, 5655 (1984).

[75] J. F. Janak, *g-factor of the two-dimensional interacting electron gas*, Physical Review, **178**, 1416 (1969).

[76] I. L. Aleiner and L. I. Glazman, *Two dimensional electron liquid in a weak magnetic field*, Phys. Rev. B, **52**, 11296 (1995).

[77] G. F. Giuliani and J. J. Quinn, *Spin-polarization instability in a tilted magnetic field in a two-dimensional electron gas with filled Landau levels*, Phys. Rev. B, **31**, 6228 (1985).

[78] G. F. Giuliani and J. J. Quinn, *Triplet exciton and ferromagnetic instability of a two-dimensional electron gas in a large magnetic field with filling factor 2*, Sol. St. Commun., **54**, 1013 (1985).

[79] G. F. Giuliani and J. J. Quinn, *Magnetic instabilities of a two-dimensional electron gas in a large magnetic field*, Surf. Sci., **170**, 316 (1986).

[80] S. Yarlagadda, *Magnetization instabilities at tilted magnetic fields in the quantum Hall regime*, Phys. Rev. B, **44**, 13101 (1991).

[81] M. Combescot and P. Nozieres, *Condensation of excitons in germanium and silicon*, J. Phys. C, **5**, 2369 (1972).

[82] P. A. Bobbert, H. Wieldraaijer, R. van der Weide, M. Kemerink, P. M. Koenraad, and J. H. Wolter, *Exchange-correlation energy of a hole gas including valence band coupling*, Phys. Rev. B, **56**, 3664 (1997).

[83] R. A. Abram, G. N. Childs, and P. A. Saunderson, *Band gap narrowing due to many-body effects in silicon and gallium arsenide*, J. Phys. C, **17**, 6105 (1984).

[84] G. E. W. Bauer and T. Ando, *Theory of band gap renormalization in modulation-doped quantum wells*, J. Phys. C, **19**, 1537 (1986).

[85] W. O. G. Schmitt, *Density-functional calculation for quasi-two-dimensional hole gases*, Phys. Rev. B, **55**, 15221 (1994).

[86] W. O. G. Schmitt, *Density-functional calculation of Landau levels for a quasi-two-dimensional hole gas*, Phys. Rev. B, **55**, 15239 (1994).

[87] A. Pinczuk, J. Shah, R. C. Miller, A. C. Gossard, and W. Wiegmann, *Optical processes of 2D electron plasmae in GaAs/AlGaAs heterostructures*, Sol. St. Commun., **50**, 735 (1984).

[88] E. Blackwood, M. J. Snelling, R. T. Harley, S. R. Andrews, and C. T. Foxon, *Exchange interaction of excitons in GaAs heterostructures*, Phys. Rev. B, **50**, 14246 (1994).

[89] N. J. Traynor, R. J. Warburton, M. J. Snelling, and R. T. Harley, *Highly nonlinear Zeeman splitting of excitons in semiconductor quantum wells*, Phys. Rev. B, **55**, 15701 (1997).

[90] P. T. Coleridge, A. S. Sachrajda, P. Zawadzki, R. L. Williams, and H. Lafontaine, *The Hall insulator in 2-dimensional SiGe hole gases*, Sol. St. Commun., **102**, 755 (1997).

[91] M. Kemerink, P. M. Koenraad, and J. H. Wolter, *Exchange interaction in p-type GaAs/AlGaAs heterostructures studied by magnetotransport*, Phys. Rev. B, **57**, 6629 (1998).

[92] I. S. Millard, N. K. Patel, M. Y. Simmons, E. H. Linfield, D. A. Ritchie, G. A. C. Jones, and M. Pepper, *Compressibility studies of double electron and double hole gas systems*, Appl. Phys. Lett., **68**, 3323 (1996).

[93] B. E. Cole, F. M. Peeters, A. Ardavan, S. O. Hill, J. Singleton, W. Batty, J. M. Chamberlain, A. Polisskii, M. Henini, and T. Cheng, *Collective cyclotron modes in high-mobility two-dimensional hole systems in GaAs/AlGaAs heterojuctions .1. Experiments at low magnetic fields and theory*, J. Phys.: Cond. Matt., **9**, 3163 (1997).

[94] N. R. Cooper and J. T. Chalker, *Theory of spin-split cyclotron resonance in the extreme quantum limit*, Phys. Rev. Lett., **72**, 2057 (1994).

[95] H. C. Manoharan and M. Shayegan, *Wigner crystal versus Hall insulator*, Phys. Rev. B, **50**, 17662 (1994).

[96] A. G. Davies, E. E. Mitchell, R. G. Clark, P. E. Simmonds, D. A. Ritchie, M. Y. Simmons, M. Pepper, and G. A. C. Jones,

Magneto-optical probe of the two-dimensional hole-system low temperature ground states, Phys. Rev. B, **51**, 7357 (1995).

[97] R. B. Dunford, E. E. Mitchell, R. G. Clark, V. A. Stadnik, F. F. Fang, R. Newbury, R. H. McKenzie, R. P. Starrett, P. J. Wang, and B. S. Meyerson, *A low-temperature insulating phase at $\nu = 1.5$ for 2D holes in high mobility Si/SiGe heterostructures with Landau level degeneracy*, J. Phys.: Cond. Matt., **9**, 1565 (1997).

[98] M. Y. Simmons, A. R. Hamilton, M. Pepper, E. H. Linfield, P. D. Rose, D. A. Ritchie, A. K. Savchenko, and T. G. Griffiths, *Metal-insulator transition at $B = 0$ in a dilute two dimensional GaAs/AlGaAs hole gas*, Phys. Rev. Lett., **80**, 1292 (1998).

[99] R. J. Nicholas, R. J. Haug, K. v. Klitzing, and G. Weimann, *Exchange enhancement of the spin splitting in a GaAs/AlGaAs heterojunction*, Phys. Rev. B, **37**, 1294 (1988).

[100] A. Usher, R. J. Nicholas, J. J. Harris, and C. T. Foxon, *Observation of magnetic excitons and spin waves in activation studies of a two-dimensional electron gas*, Phys. Rev. B, **41**, 1129 (1990).

[101] A. Schmeller, J. P. Eisenstein, L. N. Pfeiffer, and K. W. West, *Evidence for skyrmions and single spin flips in the integer quantized Hall effect*, Phys. Rev. Lett., **75**, 4290 (1995).

[102] S. Pollitt, M. Pepper, and C. J. Adkins, *The Anderson transition in silicon inversion layers*, Surf. Sci., **58**, 79 (1976).

[103] S. Kawaji and J. Wakabayashi, *Temperature dependence of the magnetoconductivity in the ground Landau level in silicon inversion layers*, Sol. St. Commun., **22**, 87 (1977).

[104] F. F. Fang and P. J. Stiles, *Effects of a tilted magnetic field on a two-dimensional electron gas*, Physical Review, **174**, 823 (1968).

[105] Y. Iye, E. E. Mendez, W. I. Wang, and L. Esaki, *Magnetotransport properties and subband structure of the two-dimensional hole gas in GaAs/AlGaAs heterostructures*, Phys. Rev. B, **33**, 5854 (1986).

[106] R. W. Martin, R. J. Nicholas, G. J. Rees, S. K. Haywood, N. J. Mason, and P. J. Walker, *Two-dimensional spin confinement in strained-layer quantum wells*, Phys. Rev. B, **42**, 9237 (1990).

[107] A. G. Davies, D. A. Ritchie, J. E. F. Frost, and M. Pepper, *Universal dissipative resistivity in the fractional quantum Hall effect in 2-dimensional hole systems*, Phys. Rev. B, **52**, 5507 (1995).

[108] S. I. Dorozhkin, C. J. Emeleus, T. E. Whall, and G. Landwehr, *Tuning of the quantum Hall effect state - insulator transition by tilting of the magnetic field*, Phys. Rev. B, **52**, 11638 (1995).

[109] W. Heuring, E. Bangert, K. Grotsch, G. Landwehr, G. Weimann, W. Schlapp, J.-H. Reemtsma, and K. Heim, *Influence of warping on quantum oscillations in p-type GaAs/AlGaAs heterostructures*, Surf. Sci., **229**, 76 (1990).

[110] H. H. Sample, L. J. Neuringer, and L. G. Rubin, *Low temperature thermometry in high magnetic fields. iii. carbon resistors (0.5-4.2 k); thermocouples*, Rev. Sci. Instr., **45**, 64 (1974).

[111] D. Shoenberg, *Magnetic oscillations in metals*, Cambridge University Press, 1984.

[112] Y. Ono, *Localization of electrons under strong magnetic fields in a two-dimensional system*, J. Phys. Soc. Jpn., **51**, 237 (1982).

[113] G. Ebert, K. von Klitzing, C. Probst, E. Schuberth, K. Ploog, and G. Weimann, *Hopping conduction in the Landau level tails in GaAs/AlGaAs heterostructures at low temperatures*, Sol. St. Commun., **45**, 625 (1983).

[114] R. G. Clark, J. R. Mallett, S. R. Haynes, J. J. Harris, and C. T. Foxon, *Experimental determination of fractional charge e/q in the fractional quantum Hall effect*, Phys. Rev. Lett., **60**, 1747 (1988).

[115] M. J. Snelling, E. Blackwood, C. J. McDonagh, R. T. Harley, and C. T. B. Foxon, *Exciton, heavy-hole, and electron g factors in type I GaAs/AlGaAs quantum wells*, Phys. Rev. B, **45**, 3922 (1992).

[116] P. T. Coleridge, A. S. Sachrajda, H. Lafontaine, and Y. Feng, *Magnetotransport coefficients in a two-dimensional SiGe hole gas*, Phys. Rev. B, **54**, 14518 (1996).

[117] W. Heuring, E. Bangert, G. Landwehr, G. Weimann, and W. Schlapp, *p-Type GaAs/AlGaAs heterostructures in tilted magnetic fields: theory and experiments*, Springer series in Solid-State Sciences Vol. 87, Springer-Verlag, 1989.

[118] S. I. Dorozhkin, *Shubnikov-de Haas oscillation beats and anisotropy of the g factor in two dimensional hole systems*, Sol. St. Commun., **72**, 211 (1989).

[119] F. F. Fang, P. J. Wang, B. S. Meyerson, J. J. Nocera, and K. E. Ismail, *Two-dimensional hole gas in Si/SiGe heterostructures*, Surf. Sci., **263**, 175 (1992).

[120] K. Hirakawa, Y. Zhao, M. B. Santos, M. Shayegan, and D. C. Tsui, *Anomalous cyclotron-resonance line splitting of two dimensional holes in* (311)*A AlGaAs/GaAs heterojuctions*, Phys. Rev. B, **47**, 4076 (1993).

[121] Z. Schlesinger and W. I. Wang, *Two dimensional hole-gas cyclotron line splitting in the extreme quantum regime*, Phys. Rev. B, **33**, 8867 (1986).

[122] S. J. Hawksworth, S. Hill, T. J. B. M. Janssen, J. M. Chamberlain, J. Singleton, U. Ekenberg, G. M. Summers, G. A. Davies, R. J. Nicholas, E. C. Valadares, M. Henini, and J. A. A. J. Perenboom, *Cyclotron resonance of high-mobility GaAs/AlGaAs* (311) *2DHGs*, Semiconduc. Sci. Technol., **8**, 1465 (1993).

[123] S. Koch, R. J. Haug, K. v. Klitzing, and M. Razeghi, *Suppression of the Landau level co-incidence: A phase transition in tilted magnetic fields*, Phys. Rev. B, **47**, 4048 (1993).

[124] J. P. Eisenstein, H. L. Stormer, L. Pfeiffer, and K. W. West, *Evidence for a phase transition in the fractional quantum Hall effect*, Phys. Rev. Lett., **62**, 1540 (1989).

[125] R. R. Du, A. S. Yeh, H. L. Stormer, D. C. Tsui, L. N. Pfeiffer, and K. W. West, *Fractional quantum Hall effect around ν=3/2: Composite fermions with spin*, Phys. Rev. Lett., **75**, 3926 (1995).

[126] P. J. Rodgers, B. L. Gallagher, M. Henini, and G. Hill, *Observation of a spin polarization phase transition of the 4/3 fractional quantum Hall state in a high-mobility 2D hole system*, J. Phys.: Cond. Matt., **5**, 565 (1993).

[127] V. I. Falko, *The fine structure of cyclotron and spin resonances at their crossing: interplay of spin-orbit and Coulomb interactions*, J. Phys.: Cond. Matt., **5**, 8725 (1993).

[128] D. J. Paul, J. R. A. Cleaver, and H. Ahmed, *Cotunnelling of holes in silicon-based structures*, Phys. Rev. B, **49**, 16514 (1994).

[129] A. Yakimov, V. Markov, A. Dvurechenskii, and O. Pchelyakov, *Longitudinal conductivity of Ge/Si heterostructures with quantum dots*, Sov. Phys. JETP, **63**, 444 (1996).

[130] E. Leobandung, L. Guo, and S. Y. Chou, *Single hole quantum dot transistors in silicon*, Appl. Phys. Lett., **67**, 2338 (1995).

[131] T. Sogawa, H. Ando, S. Ando, and H. Kanbe, *Interband optical transition in GaAs quantum wires with rectangular cross sections*, Phys. Rev. B, **56**, 1958 (1997).

[132] P. C. Sercel and K. J. Vahala, *Analytical technique for determining the polarization dependence of optical matrix elements in quantum wires with band-coupling effects*, Appl. Phys. Lett., **57**, 545 (1990).

[133] G. Goldoni, F. Rossi, E. Molinari, A. Fasolino, R. Rinaldi, and R. Cingolani, *Valence-band spectroscopy in V-grooved quantum wires*, Appl. Phys. Lett., **69**, 2965 (1996).

[134] G. Goldoni, F. Rossi, E. Molinari, and A. Fasolino, *Band-structure and optical anisotropy in V-shaped and T-shaped semiconductor quantum wells*, Phys. Rev. B, **55**, 7110 (1997).

[135] C. W. J. Beenakker and H. van Houten, *Quantum point contacts*, Semiconductors and Semimetals, Academic Press, New York, 1990.

[136] J. E. F. Frost, M. Y. Simmons, M. Pepper, A. C. Churchill, D. A. Ritchie, and G. A. C. Jones, *Temperature limits for ballistic quantization in a GaAs/AlGaAs one-dimensional constriction*, J. Phys.: Cond. Matt., **5**, 559 (1993).

[137] K. J. Thomas, *Transport properties of high mobility one-dimensional electron gases*, PhD thesis, University of Cambridge, 1997.

[138] C. L. Kane and M. P. A. Fisher, *Transmission through barriers and resonant tunnelling in an interacting one-dimensional electron gas*, Phys. Rev. B, **46**, 15223 (1992).

[139] V. V. Ponomarenko, *Renormalization of the one-dimensional conductance in the Luttinger liquid model*, Phys. Rev. B, **52**, 8666 (1995).

[140] D. L. Maslov and M. Stone, *Landauer conductance of Luttinger liquids with leads*, Phys. Rev. B, **52**, 5539 (1995).

[141] N. K. Patel, L. Martin-Moreno, M. Pepper, R. Newbury, J. E. F. Frost, D. A. Ritchie, G. A. C. Jones, J. T. M. B. Janssen, J. Singleton, and J. A. A. J. Perenboom, *Ballistic transport in one dimension: additional quantization produced by an electric field*, J. Phys.: Cond. Matt., **2**, 7247 (1990).

[142] N. K. Patel, J. T. Nicholls, L. Martin-Moreno, M. Pepper, J. E. F. Frost, D. A. Ritchie, and G. A. C. Jones, *Evolution of half plateaus as a function of electric field in a ballistic quasi-one-dimensional constriction*, Phys. Rev. B, **44**, 13549 (1991).

[143] K. J. Thomas, J. T. Nicholls, M. Y. Simmons, M. Pepper, D. R. Mace, and D. A. Ritchie, *Ballistic transport in one-dimensional constrictions formed in deep 2-dimensional electron gases*, Appl. Phys. Lett., **67**, 109 (1995).

[144] L. Martin-Moreno, J. T. Nicholls, N. K. Patel, and M. Pepper, *Non-linear conductance of a saddle-point constriction*, J. Phys.: Cond. Matt., **4**, 1323 (1992).

[145] L. I. Glazman and A. V. Khaetskii, *Nonlinear quantum conductance of a lateral microconstraint in a heterostructure*, Europhys. Lett., **9**, 263 (1989).

[146] A. M. Zagoskin, *Nonlinear electrical conductivity of ballistic quantum contacts*, Sov. Phys. JETP Lett., **52**, 435 (1990).

[147] C. H. W. Barnes, *Private communication*, 1996.

[148] G. Goldoni and A. Fasolino, *Hole states in quantum wells in high in-plane magnetic fields: Implications for resonant magnetotunnelling spectroscopy*, Phys. Rev. B, **48**, 4948 (1993).

[149] T. P. Smith-III, J. A. Brum, J. M. Hong, C. M. Knoedler, H. Arnot, and L. Esaki, *Magnetic anisotropy of a one-dimensional electron system*, Phys. Rev. Lett., **61**, 585 (1988).

[150] U. Bockelmann and G. Bastard, *Interband absorption in quantum wires. i. zero-magnetic-field case*, Phys. Rev. B, **45**, 1688 (1992).

[151] U. Bockelmann and G. Bastard, *Interband absorption in quantum wires. ii. nonzero-magnetic-field case*, Phys. Rev. B, **45**, 1700 (1992).

[152] G. Goldoni and A. Fasolino, *Valence band structure, edge states, and interband absorption in quantum-well wires in high magnetic fields*, Phys. Rev. B, **52**, 14118 (1995).

[153] L. Calmels and A. Gold, *Many-body effects in the interacting quasi-one-dimensional electron gas: Oscillator confinement*, Phys. Rev. B, **56**, 1762 (1997).

[154] C. K. Wang and K.-F. Berggren, *Spin splitting of subbands in quasi-one-dimensional electron quantum channels*, Phys. Rev. B, **54**, 14257 (1997).

[155] L. Calmels and A. Gold, *Spin-susceptibility of the quasi-one-dimensional electron gas with long-range Coulomb interaction*, Europhys. Lett., **39**, 539 (1997).

[156] K. J. Thomas, J. T. Nicholls, M. Y. Simmons, M. Pepper, D. R. Mace, and D. A. Ritchie, *Possible spin polarization in a one-dimensional electron gas*, Phys. Rev. Lett., **77**, 135 (1996).

[157] N. K. Patel, J. T. Nicholls, L. Martin-Moreno, M. Pepper, J. E. F. Frost, D. A. Ritchie, and G. A. C. Jones, *Properties of a ballistic quasi-one-dimensional constriction in a parallel high magnetic field*, Phys. Rev. B, **44**, 10973 (1991).

[158] M. Oestreich, A. P. Heberle, W. W. Ruhle, R. Notzel, and K. Ploog, *Extreme anisotropy of the g factor in quantum wires*, Europhys. Lett., **31**, 399 (1995).

[159] S. A. J. Wiegers, M. Specht, M. Y. Simmons, D. A. Ritchie, A. Cavanna, B. Etienne, G. Martinez, and P. Wyder, *Magnetization and energy gaps of a high-mobility 2D electron gas in the quantum limit*, Phys. Rev. Lett., **79**, 3238 (1997).

[160] M. J. Manfra, E. H. Goldberg, B. B. Goldberg, D. A. Broido, L. Pfeiffer, and K. West, *Temperature dependence of the spin polarization of a quantum Hall ferromagnet*, Phys. Rev. B, **54**, 17327 (1996).

[161] B. E. Kane, L. N. Pfeiffer, and K. West, *High-mobility GaAs heterostructure field-effect transistor for nanofabrication in which dopant-induced disorder is eliminated*, Appl. Phys. Lett., **67**, 1262 (1995).

[162] R. H. Harrel and K. S. Pyshkin, *Private communication*, 1998.

[163] F. D. M. Haldane, *Luttinger liquid theory of one-dimensional quantum fluids. 1. Properties of the Luttinger model and their extension to the general 1D interacting spinless Fermi gas*, J. Phys. C, **14**, 2585 (1981).

[164] A. Kent, *Experimental low-temperature physics*, Macmillan, London, 1993.

[165] S. S. Nedorezov, *Space quantization in semiconductor films*, Sov. Phys.-Solid State, **12**, 1814 (1971).

[166] L. Andreani, A. Pasquarello, and F. Bassani, *Hole subbands in strained GaAs/AlGaAs quantum wells: Exact solution of the effective mass equation*, Phys. Rev. B, **36**, 5887 (1987).